Hybrid rare-earth ion superconductor systems for quantum information processing

Ilana Wisby

Department of Physics

Royal Holloway, University of London

This dissertation is submitted for the degree of

Doctor of Philosophy

April 2017

In memory of Russell Gwilliam,

without whom this work would not have been possible.

Declaration

I, Ilana Wisby, hereby declare that this thesis and the work presented in it is entirely my own. Where I have consulted the work of others, this is always clearly stated.

Ilana Wisby

April 2017

Acknowledgements

First and foremost I would like to thank both my supervisors: Phil Meeson and Tobias Lindström, for both providing me with the opportunity to undertake this PhD and your continued support throughout the process. Thank you, both for all your guidance, enthusiasm and patience. Without your help, this would not have been possible.

Special thanks to Tobias for providing me with the guidance, trust and independence within the lab, and for keeping me sane in the screened room with all your funny and slightly long anecdotes (I'm not sure how people think you are still known as the quiet Swedish one). Special thanks to Phil for catching my spelling mistakes and reading this thesis back to front, as well as all the enlightening discussions over the years.

Many thanks to Sebastian de Graaf, who has made fabrication fun, and been a wealth of support, discussion and knowledge in so many ways. I would not have been able to do this without you and for that, I will be forever thankful.

I would also like to thank my collaborators at Chalmers, Royal Holloway, and the Ion Beam Centre, Surrey. Sergey, Asterigk, Oleg and Russ respectively. It has been an absolute pleasure and this thesis would not have been possible without these opportunities.

A big thank you to the rest of the quantum detection group for all your efforts, both great and small, in particular to Sasha, Jon and Steve for being there at crap-hitting-the-fan-and-supervisor-being-away moments! I am also grateful for the support of all the other fellow students and friends. In particular to Viktoria and John who have been a source of much-needed laughter, sarcasm and gin. Thanks also to Katie, Pardis, Nathan,

Stephen, Shaun, Ana, Ruth, Vishal for letting me pick your brains, borrow your kit, and generally for being great friends.

Finally, I would like to thank my coworkers, friends and family, with special kudos to my parents and sisters for their love and support over the last few years - where relating to my problems has probably been a little harder to endure!

Abstract

Interfacing rare-earth doped crystals with superconducting circuit architectures provides an attractive platform for quantum memory and transducer devices. This work demonstrates the development and implementation of an alternative approach for creating a scalable quantum memory system. The process utilises a local ion implantation technique to control both the location and density of spins, without introducing additional dielectric interfaces which are thought to introduce noise. The hybrid device is fabricated by a controlled ion implantation of rare-earth ions in well-defined micron-sized areas of a substrate, which are aligned to lithographically defined microresonators: a highly scalable technique.

This work first demonstrates that within the limit of our experimental sensitivity, the fabrication procedure does not degrade the internal quality factors of the resonators, which remain above 10^5. We next investigate the properties of the implanted spin system through angular dependent microresonator electron spin resonance (micro-ESR) spectroscopy. We extract corresponding coupling rates of the order of 1 MHz and spin linewidths of $50 - 150$ MHz. We find, that despite the high energy near-surface implantation, the resulting micro-ESR spectra are in excellent agreement with the modelled Hamiltonian, supporting the notion that the dopant ions are well integrated into their relevant lattice sites whilst maintaining crystalline symmetries. Furthermore, we observe clear undesirable contributions from different microwave field components of our microresonator, emphasising the need for controllable local implantation.

Table of Contents

List of Figures

List of Tables

Chapter 1

Introduction

This thesis focuses on the development and implementation of a hybrid quantum memory device, interfacing a locally implanted rare-earth doped crystal with a superconducting microresonator. This approach aims to exploit the sensitive detection and scalability provided by circuit quantum electrodynamics (cQED) along with the coherence of natural rare-earth ions. The thesis presents the development of the fabrication process of the device, before presenting experimental data. We find that the fabrication technique does not degrade the internal quality factor of the resonators, and are able to investigate the properties of the implanted spin system through angular dependent microresonator electron spin resonance (micro-ESR) spectroscopy. The work demonstrates the promising potential of locally implanted rare-earth doped crystals for application in hybrid quantum technologies.

1.1 The bigger picture

It has long been recognised that to realise quantum communication requires a quantum network [1]. This network enables the distribution of quantum states over large distances [2], in a similar manner to that of classical fibre optic communications. There are advantages to using existing fibre-optic cables to facilitate the transmission of quantum

information: a quantum network would also benefit from the low-loss attenuation associated with optical fibres (at a rate of ≈ 17 dB/km at a 1550 μm wavelength), and it is also beneficial to consider the integration of new quantum communication technology within existing communication architectures.

There are, however, some key differences between the operation of a quantum and classical network. In a classical network, information is sent via optical photons from the sender to the recipient via a number of amplifiers which compensate for any photon losses. At either end of the network, a transducer node converts the information from electronic to optical information, or vice-versa. In the operation of a quantum network, quantum information is entangled within photons and is distributed from a sender, through some form of amplifier and network system, to the recipient. Unlike the amplification process of a classical network, it is not possible to directly amplify the quantum state without destroying the information. Therefore the amplifiers must be replaced with some other device, which takes the form of a quantum repeater. The principle operation of such a repeater requires the photons to be converted into stationary qubits to be processed again, employing additional photons to distribute the entanglement between senders, repeater stations and the recipient [3]. As such, whilst the entangled information may travel from A to B, the photon does not.

To realise a quantum repeater, we must have the ability to coherently store and retrieve the quantum information on demand, thus defining the need for a quantum memory [4]. Such a quantum memory must be able to provide long storage times, coherent information transfer, enable fast processing speeds and, crucially, be scalable. When considering any potential quantum memory device, we must reflect on these generally accepted prerequisites.

One approach in realising such a quantum memory lies in the field of solid-state quantum information processing, where rapid progress has been made in recent years. This progress

has come from the field of circuit quantum electrodynamics (cQED) where macroscopic Josephson qubits - anharmonic quantum electromagnetic oscillators - are coupled to a resonator [5]. Quantum states are then stored and manipulated in the qubit device. Typically, these devices operate in the microwave regime (1 - 10 GHz) at cryogenic temperatures and have demonstrated great success and future potential, for example, with the creation of quantum states and the demonstration of elementary quantum processes [6, 7].

In conforming with the prerequisites for an effective quantum memory device, we find that cQED devices hold the potential for coherent information transfer, enable relatively fast processing speeds, and are highly scalable. The device potential, however, in terms of memory storage has been found to be fundamentally limited by the coherence times of the qubit [8].

Despite this flaw, the benefits of utilising cQED have been recognised, prompting interest in a hybrid approach, combining such superconducting circuitry with other two-level systems (TLS). In this way, the unique strengths of individual systems in conjunction [9] may be exploited. Device scalability, low loss rates, and fast processing speeds may be provided by superconducting circuitry [10] whilst the long storage times are facilitated by other 'natural' TLS as a memory element.

The 'natural' TLS (as opposed to man-made qubits) generally hold the advantage of being less well coupled to the environment, and as such are less susceptible to decoherence and relaxation. There are a number of natural quantum systems available, each with their own advantages and disadvantages. Since superconducting circuits have previously shown success in terms of performance, early hybrid devices (from 2006 - 2009) were developed around this concept. This research involved the coupling of spin degrees of freedom to coplanar waveguide (CPW) resonators, where the spin system took the form of molecules [11, 12], trapped cold atoms and ions [13–15], two-level defects [16] and

spins in solids [17, 18]. From these experiments, the most practical and promising device was demonstrated to be electronic spins in solids. It was found that coherent information transfer mediated by the strong coupling regime is difficult to achieve with a single spin. This regime may, however, be reached using an ensemble of spins in the form of a spin doped crystal - providing an enhancement of collective coupling proportional to $\sqrt{N}$.

In more recent years (within the time-scale of this project), there has been a plethora of activity around this area, focusing on circuit and cavity QED experiments coupled to a number of types of different spin ensembles. These include spin centres in the form of NV-centres in diamond [19–22], where strong coherent coupling has been demonstrated [23, 24], iron impurities [25], and phosphorus [26] and bismuth donors [27] in silicon.

Rare-earth (R.E) ion doped crystals are of particular interest for transducer applications necessary for long-range quantum communications, due to both the microwave and optical accessibility mediated by the inner $4f$ shell transition [28, 29]. Rare-earth ion doped crystals coupled to superconducting circuitry was identified as a system of interest within this group and is the basis of this work. Within the community, there is particular interest in neodymium and erbium ions, which possess optical transitions in standard telecommunications bands. Strong coupling of an erbium spin ensemble to superconducting and non-superconducting resonators has been demonstrated [30–32]. There has been promising progress made in optical quantum memories based on rare-earth elements, with the demonstration of multi-mode storage [33]. Additionally, work on ferromagnetic spin ensembles has been recently reported [34–36]. Coherent coupling to iron groups has been demonstrated in a whispering gallery mode 3D resonator [37], and molecular spin ensembles have also demonstrated strong coupling at room temperature in standard ESR cavity experiments [38, 39].

1.2 Identifying our niche and project aims

At the time of commencing this project, spin doped crystals had previously demonstrated operation in the strong coupling regime through 'flip-chip' style experiments [23, 31]. In a flip-chip experiment, a doped crystal sample is mechanically pressed, or glued to the top of a superconducting cavity. Whilst this method demonstrated the underlying physics necessary for such a hybrid device, with many of the prerequisites for a quantum memory being met, such a device is not fundamentally scalable. Additional drawbacks included a lack of control of the configuration of coupled spins and an introduction of additional two-level-systems from the additional interfaces. These interfaces increase the dielectric losses [40] and as such result in an increased level of decoherence.

We identified this as a niche to work within, seeking to implement an alternative approach utilising an ion implantation technique to allow for control of both the location and density of spins without introducing additional dielectric interfaces. It was theorised that by fabricating the device using a controlled ion implantation of rare-earth ions within well-defined micron-sized areas of a substrate, and by aligning these spin doped regions to microresonators created directly on top of the substrate, we may eliminate the additional dielectric interface and create a highly scalable hybrid device. The concept of the device is outlined as follows:

The device is comprised of a superconducting microresonator which is fabricated on a substrate. Beneath the microresonator and within the substrate lies an ensemble of spins which have been locally implanted prior to the device fabrication. The spin system takes the form of an ensemble of rare-earth ions, which have a partially filled inner 4f shell providing a magnetic moment which may be utilised for quantum storage. As such, subjecting the device to an externally applied magnetic field gives rise to a Zeeman field splitting within the spin ensemble. This energy splitting may be matched at certain

magnetic fields to the centre frequency of the microresonator, such that when the device is probed with on-resonance photons, the photons may couple to the spin ensemble. The coupling rate is proportional to the number of spins, such that a higher number of spins increases the coupling rate, and provides stronger coupling. Manipulations of the spin state may then be applied via pulsed micro-electron-spin-resonance experiments, thus demonstrating experimentally the potential of a locally implanted rare earth approach for application as a coherent quantum memory.

The initial challenge lies in the integration of ion implantation with superconducting microresonators. It was largely believed that the substrate crystalline surface would be damaged to a level that would impact upon the superconducting device quality. This was a key initial question to answer.

Before we could answer this, however, we were required to develop the fabrication process. Provided we were successful, we could then seek to explore further experiments where we may manipulate the spin ensemble system. We, therefore, set out the initial project aims:

1. To develop the integration of a local implantation technique alongside standard e-beam lithography procedures to produce a locally implanted spin ensemble available for coupling to a superconducting microresonator device.

2. To examine the effect of this fabrication technique on the intrinsic quality factors and crystalline environment of the microresonator devices.

3. Provided previous success of points 1 and 2, to demonstrate the proof of principle of such a hybrid device by achieving coupling between the two systems. Ideally, we seek to achieve coherent coupling in the strong coupling regime.

4. To perform pulsed micro-electron-spin-resonance measurements on the device, as such proving the potential of the device for quantum memory applications.

1.3 The initial starting point

The group has previous experience in performing low-noise measurements of microresonator devices. The devices were designed, fabricated and measured within the group with the assistance of collaborative facilities. The microresonators we choose to focus on within this project are lumped-element (LE) resonator devices. These LE devices provide the benefit of frequency multiplexing and have also been found to demonstrate magnetic field resilience. Previous work within the group focused on Nb microresonators fabricated on r-cut sapphire Al_2O_3 substrates. It was decided to use this previous experience as a starting point for this work, where we have a well-developed fabrication procedure and extensive knowledge of the noise properties of the system.

This initial decision, however, greatly restricted the choice of spin species which would be available to use within early, exploratory experiments. This restriction was due to the lack of literature available detailing the implantation of rare-earth ions within sapphire substrates. The literature, therefore, guided the decision to focus on a Gd^{3+} in Al_2O_3 system, which is the focus of this study.

1.4 An outline of the thesis

This thesis commences with an introduction to the overall concept behind the implementation of the hybrid device. The theoretical concepts behind each individual element are then explored. We first focus on the superconducting resonator, followed by the spin system and the substrate independently before considering the doped Al_2O_3 system. The coupling mechanism between the resonator and spin ensemble system is then presented. Next, with a more thorough understanding of the theory, we study the viability of the hybrid device through a number of simulations. These simulations seek to demonstrate that the chosen system is capable of the desired operation, and aims to provide some

guidance to the design process and choice of experimental parameters.

We detail the development of the fabrication process used to created the hybrid sample, meeting of the project's first aim. This section covers the initial sample designs, fabrication techniques and processes. Some time is spent describing the motivation behind certain techniques used and steps within this process.

The experimental section of this thesis first presents an overview of a number of cryogenic systems utilised within this work before describing the initial sample characterisation. We then seek to meet the second aim by exploring the effect of the fabrication technique on the intrinsic quality factor of the microresonator devices. This is explored using a standard S_{21} microwave measurement technique. We find the fabrication process does not degrade the internal quality factor of the resonators, which remains above 10^5.

Based on this success, we next consider proof of principle investigations using a superconducting micro-electron-spin-resonance (micro-ESR) technique. Here, resonator responses are investigated with respect to a variable magnetic field. When the spin ensemble Zeeman splitting is degenerate with the microresonator centre frequency, ESR's may be observed by a change in the resonator quality factor. This, in turn, provides an absorption spectroscopy trace. Information regarding the spin ensemble's coupling rates, line-widths and quality factor can then be extracted from this data. We observe electron spin resonances in good agreement with numerical modelling and extract corresponding coupling rates, of the order of 1 MHz and spin linewidths of 50-65 MHz.

Whilst the third aim of pulsed-ESR measurements have been explored within this project, further information regarding this is presented in Appendix. D, where such experiments did not yield successful results.

As such, we present further measurements which seek to examine the locally doped crystals and their structure in detail. This exploration is performed using angular dependent micro-ESR spectroscopy and temperature dependent ESR measurements.

We find the measured angular micro-ESR spectra to be in excellent agreement with the modelled Hamiltonian. This supports the conclusion that the dopant ions are well integrated into their relevant lattice sites and that crystalline symmetries are maintained. Furthermore, from these measurements, we observe individual contributions from the spatial components of the microwave field of the microresonator device. This emphasises the need for better controlled local implantation. After some additional discussions, we conclude this thesis with a summary of our key findings, reflections and future outlooks. In parallel to this project, photoluminescence measurements, magnetic property measurements, THz spectroscopy and standard ESR measurements were explored with the assistance of collaborators. These and other areas of work performed during the course of the project are summarised in Appendix D, but are not directly connected to the project aims.

Chapter 2

Fundamentals of superconducting resonators

As discussed in Chapter 1, a hybrid device provides the ability to exploit the desirable properties provided by a number of different systems in conjunction. In this project, we seek to couple a locally implanted spin ensemble system to a superconducting resonance cavity mode.

The cavity system of choice is a superconducting microresonator device. These devices are particularly advantageous in terms of scalability, where we may create many resonators spanning a wide frequency range upon a single device. In this chapter, we begin by exploring the theory behind the lumped element superconducting microresonator devices utilised in this work - specifically operating within the low power, low-temperature regime. Since this measurement technique used in this project utilises the measurement of losses within the resonator, the microwave transmission measurement response is described, before the loss mechanisms are next explored. There is particular focus on the device operation and losses when subjected to external magnetic field.

2.1 Superconductivity

The property of superconductivity was first discovered in 1911 by H. Kammerlingh Onnes [41]. Onnes noticed that for specific metals below a material dependent temperature, the electrical resistance vanished. Perfect diamagnetism was then discovered by Meissner and Oschsendfeld in 1933. This was explained more with the development of BCS theory [42], which demonstrated superconductivity as a unique thermodynamic state with the formation of Cooper-pairs below a given critical temperature. The theory explained both the electron pairing mechanism and the temperature dependence of the effect. Furthermore, it provided a framework to describe the vanishing DC resistance, expulsion of magnetic fields, exponentially decreasing heat capacity and infra-red properties of superconductivity.

Many microwave components benefit from the decreased losses provided by the superconducting state. Within the context of this project, the property of low loss is exploited in the utilisation of the superconducting microresonator device and can be satisfactorily described by the two-fluid model. This phenomenological model was developed in the 1930's and preceded that of BCS theory, however, the main elements were later supported by BCS theory.

2.1.1 Mattis-Bardeen theory and the two fluid model

When a superconductor is cooled through the superconducting transition temperature, T_c, the charge carriers divide into two populations; normal electrons (quasiparticles), and Cooper-pairs. The total carrier density is $n_t = n_n + n_s$, where n_n, n_s are the quasiparticle and Cooper-pair densities respectively. The ratio of the path densities as a function of temperature may be described by the theory of Mattis and Bardeen [43]. As the temperature decreases below T_c, the density of Cooper-pairs increases, until the total

electron density comprises Cooper-pairs at $T = 0$,

$$\sigma_s = \sigma_t(1 - (T/T_c)^4). \tag{2.1}$$

This phenomenon may be detected by amplifying a current of frequency ω. Assuming that the frequency, ω is smaller than the electron inverse scattering time, τ_n^{-1} ($\omega << \tau_n^{-1}$), the complex conductivity, σ may be considered as a summation of the quasiparticle and superconductor conductivity, σ_n and σ_s respectively. This is derived as,

$$\sigma = \sigma_n + i\sigma_s = \frac{n_n e^2 \tau_n}{m_e} - i\frac{n_s e^2}{m_e \omega}, \tag{2.2}$$

where m_e is the mass of an electron. Typical quasiparticle scattering times are of order $\approx 10^{-12}$ s. This restricts ω to be < 100 GHz. Operating outside this regime ($\omega > \tau_n^{-1}$) results in a complex surface impedance, Z_s,

$$Z_s = \sqrt{\frac{i\mu\omega_0}{\sigma_n i\sigma_s}} = R_s + i\omega L_s \tag{2.3}$$

where R_s and L_s are the cooper-pair resistance and inductance respectively.

An additional consequence of the population splitting is an increased superconductor kinetic inductance. As a Cooper-pair absorbs energy from a high-frequency field, it does not then partake in scattering events. Instead, excess kinetic energy is stored within the condensate. This enables superconducting circuits to exhibit larger inductances than the geometry alone typically allows. The kinetic inductance per unit length L_k may be calculated from the excess kinetic energy of the Cooper-pairs, n_s contributing to the current density, J_s. This is,

$$\mathrm{KE} = \frac{1}{2} n_s m v_s^2 \tag{2.4}$$

where m is mass and the v_s is the superconducting electron velocity in terms of the current density, $I_s = n_s e v_s$. Substituting this through Eq. 2.4, leads to,

$$\text{KE} = \frac{1}{2}\frac{m}{n_s e^2} I_s^2 \tag{2.5}$$

$$= \frac{1}{2}\mu_0 \lambda^2 I_s^2, \tag{2.6}$$

where λ is the superconductor penetration depth. The general formula for L_k is,

$$U_k = \frac{1}{2} L_k I^2 = \frac{1}{2}\mu_0 \lambda^2 \int_s I_s^2 \delta s \tag{2.7}$$

where U_k is the total kinetic energy per unit length and μ_0 is the vacuum permeability. The surface integral taken over a cross-section of the superconducting strip accounts for the non-uniform current distribution [44].

Within a superconductor, the current is confined within the penetration depth from the surface. In a thin film, we may assume that the film thickness $d << \lambda$. The current density in the film is, therefore, uniform and given by $I_s = I/Wd$ where W is the film width and is assumed to be greater than λ. The result for L_k then becomes:

$$\frac{1}{2} L_k I^2 = \frac{\mu_0 I^2 \lambda^2}{2W^2 d^2} Wt \tag{2.8}$$

$$\rightarrow L_k = \frac{\mu_0 \lambda^2}{Wd}. \tag{2.9}$$

In addition to the kinetic inductance, the total inductance L of a wire also includes a geometric term L_g such that:

$$L = L_g + L_k \tag{2.10}$$

.

The geometric inductance may be obtained through conformal mapping,

$$L_g = \frac{\mu_0}{4} K(k')K(k) \tag{2.11}$$

where K is the complete elliptic integral, $k = G/a$ where G is conductance per unit length, $a = 2G + W$ and $k' = \sqrt{1 - k^2}$. Detailed derivations of this may be found in Ref. [42, 45].

Resonators subjected to a magnetic field observe a quadratic shift in centre frequency. This originates from the quadratic dependence of the kinetic inductance on the magnetic field. Materials where the kinetic inductance dominates of geometric inductance, such as NbN, we may expect to see large frequency shifts with respect to an applied magnetic field. Despite this, the best materials in terms of magnetic field induced losses tend to come with large kinetic inductances.

We next explore the micro-resonator device used within this work.

2.2 Resonators

We begin with a coplanar waveguide (CPW) structure, which is used to guide microwave signals on superconducting chips in the same way a coaxial cable is used in microwave communications. The CPW is comprised of a central conductor strip of width W. The central conductor is separated from the (semi-infinite) electrical ground planes by gaps of width s, as shown in Fig. 2.1. The design is patterned into a superconducting thin film, of thickness t. The thin film is deposited on top of a dielectric substrate of dielectric constant $\epsilon_r = \epsilon' + i\epsilon''$.

The CPW may be formed into a transmission line resonator by the introduction of two additional gaps along the central conductor. As such, only discrete energy modes are allowed within transmission line structure - forming standing waves of a characteristic

Fig. 2.1 a) A CPW transmission line, consisting of a central conductor of width W, separated by gaps of distance s from the ground planes, such that $a = W + 2s$. The purple represents the superconducting thin film of thickness t, which sits on top of a dielectric substrate of height h. The CPW may be modelled as a series of lumped element circuits. b) The CPW may be formed into a transmission line resonator by the introduction of two additional gaps along the central conductor, shown with an equivalent circuit diagram. c) A series lumped element resonator design is depicted with an equivalent circuit diagram. The resonator is inductively coupled to a standard CPW transmission line.

resonance frequency, ω_0. When this resonance is excited, energy is stored oscillating between a capacitive and inductive form.

2.3 The series lumped element resonator

There are a number of types of resonator structures. Here, we focus on a series lumped element (LE) resonator device, which is primarily used within this work. The LE resonator device is desirable to use as a hybrid system, since each individual resonator is compact in geometry, and may be coupled to a single transmission line - enabling the frequency multiplexing of many resonator devices on a single chip. This provides the scalability desirable for a potential quantum communication architecture. Additionally, the LE resonator design is more robust when subject to external magnetic fields due to the device design. This is further explored in Section 2.5.4.

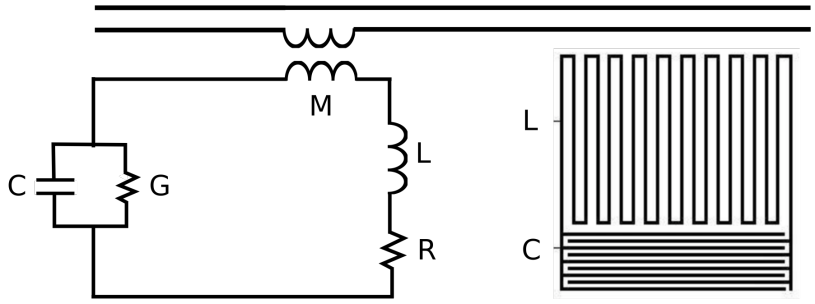

Fig. 2.2 An example of a series lumped element resonator coupled to a transmission line as a circuit (left) and as a schematic layout (right).

A series LE resonator device is comprised of an inductance L in the form of an inductive meander, capacitance C in the form of an inter-digitated capacitor, and resistance R in series and is depicted in Fig. 2.2. To excite the LE resonator, it must be placed in close proximity to a standard transmission line structure such that energy may be transferred via either an inductive or capacitive coupling element (depending on the device design).

This coupling allows the resonator to be excited by on resonance microwaves of frequency ω_0.

The total energy stored is given by $E_t = \frac{1}{2}LI^2$, where I is current. The energy is equally (on average) stored between the resonator inductor E_m and the capacitor E_e,

$$\langle E_m \rangle = \frac{1}{4}L|I|^2 \tag{2.12}$$

$$\langle E_e \rangle = \frac{1}{4}C|V|^2 \tag{2.13}$$

$$\langle E_m \rangle = \langle E_e \rangle. \tag{2.14}$$

where V is voltage. Therefore,

$$\frac{1}{4}L|I|^2 = \frac{1}{4}C|V|^2. \tag{2.15}$$

Since,

$$V = ZI \tag{2.16}$$

$$V = i\omega LI \tag{2.17}$$

$$|V|^2 = \omega^2 L^2 |I|^2. \tag{2.18}$$

Such that we can substitute this for $|I|^2$, and therefore $\langle E_m \rangle = \frac{1}{4}\frac{|V|^2}{\omega^2 L}$. As such,

$$\frac{1}{4}\frac{|V|^2}{\omega^2 L} = \frac{1}{4}|V|^2 C, \tag{2.19}$$

$$\therefore \omega_0 = \frac{1}{\sqrt{LC}}. \tag{2.20}$$

A schematic of an inductively coupled lumped element (LE) microresonator device is shown in Fig. 2.2 with an equivalent circuit model.

In this work, the microresonators are inductively coupled to the transmission line via a mutual inductance M. The coupling is present as a result of the magnetic field of the transmission line threading the fingers of the inductive meander. Each meander produces an effective loop area and the rate of change of flux threading each loop induces an emf. There is then a net effect of the emf in all but one of the loops cancelling. The magnetic flux threading is dependent on the meander geometry and the flux density across the loop area. As such, the distance between the inductive meander and the transmission line allows the coupling M to be highly tunable as the total flux threading decreases with distance.

2.4 The scattering matrix

Having considered the microresonator device as a superconducting structure, it is next necessary to consider the measurement response of the microresonator device. The microresonator may be considered as a microwave network, which is typically described in terms of a scattering matrix S, representing the ratio of voltages between the ports of a n-port system. Assuming a two-port system $(1, 2)$ yields four scattering parameters, where $V_i^{\pm}$ represents the voltage amplitude and i denotes the port $(1, 2)$, where $\pm$ denotes the incident and reflected wave at that port. The complete system may be described as [46]:

$$\begin{pmatrix} V_1^- \\ V_2^- \end{pmatrix} = \begin{pmatrix} S_{11} & S_{12} \\ S_{21} & S_{22} \end{pmatrix} \begin{pmatrix} V_1^+ \\ V_2^+ \end{pmatrix}, \tag{2.21}$$

such that the four scattering parameters are,

$$S_{11} = \frac{V_1^-}{V_1^+}, \qquad S_{12} = \frac{V_1^-}{V_2^+}, \tag{2.22}$$

$$S_{21} = \frac{V_2^-}{V_1^+}, \qquad S_{21} = \frac{V_2^-}{V_2^+}. \tag{2.23}$$

Typically in the present work, transmission of S_{21} signal measurements are performed on the microresonator devices.

For a series lumped element device the S_{21} response may be derived as a parallel shunt impedance in the transmission line, such that,

$$S_{21} = \frac{2}{2 + Z_0/Z_{in}} \tag{2.24}$$

$$= \frac{(1 + 2iQ_i\frac{\delta\omega}{\omega_0})}{(1 + 2iQ_i\frac{\delta\omega}{\omega_0}) + \frac{Q_i}{Q_l}} \tag{2.25}$$

$$= \frac{S_{21,\min} + 2iQ\frac{\delta\omega}{\omega_0}}{1 + 2iQ\frac{\delta\omega}{\omega_0)}} \tag{2.26}$$

with,

$$S_{21,\min} = \frac{Q_l}{Q_i + Q_l} \qquad Q = \frac{Q_i Q_l}{Q_i + Q_l}. \tag{2.27}$$

where Q, Q_i and Q_l are the total, intrinsic and coupled resonator quality factors respectively (these are discussed in more detail later in this section), Z_0, Z_{in} are the characteristic and input impedance respectively.

The measured S_{21} response may, therefore, be measured and fit to a function of the expression in Eq. 2.24. However, this represents only an ideal case. Often in measurements, we encounter an asymmetric resonance lineshape. This asymmetry may physical be present due to a mismatch in impedance, interactions with other resonant modes (ie.

from resonators too nearby, or unwanted resonant modes from ground planes).

This asymmetry manifests itself as a rotation of the resonance circle (the real and imaginary S_{21} parts plotted in the complex plane). This can be accounted for with the introduction of a complex factor ϕ to Eq. 2.24,

$$S_{21} = \frac{S_{21,\min} e^{i\phi} + 2iQ\frac{\delta\omega}{\omega_0}}{1 + 2iQ\frac{\delta\omega}{\omega_0}}. \tag{2.28}$$

Derivations of this can be found in Ref's. [44, 47]. Sound experimental fitting should include ϕ as an additional fitting parameter, and Eq. 2.28 is used for S_{21} fitting within this work.

From this resonator response, the characteristic Q_i values may be extracted. The extracted Q is highly sensitive to losses. This parameter may, therefore, be used to probe the spin ensemble as it is tuned in and out of resonance with the resonator device, where the spin ensemble presents itself as an additional loss mechanism. This experimental method is discussed further in Section 7.4.

2.4.1 Quality factors

These resonator devices may be characterised by a quality factor, Q, which provides a measure of resonator losses. Generally,

$$Q = \frac{\text{energy stored}}{\text{energy dissipated per cycle}}. \tag{2.29}$$

As the electromagnetic energy in a LE series resonator device is stored within the electric E_e and magnetic field E_m components, we may express Q as,

$$Q = \omega_0 \frac{E_e + E_m}{P_{lost}}, \tag{2.30}$$

where P_{lost} is the average power dissipated and is $|I|^2 R$. Assuming the average energy

stored is split equally between these modes, we may define the total average energy stored as $\langle E_m \rangle + \langle E_e \rangle = E_t$, where $\langle E_m \rangle = \langle E_e \rangle = E_t/2$.

Using these definitions, we may express Q in these electrical terms as,

$$Q = \frac{E_t}{|I|^2 R} = \omega_0 \frac{1}{2} \frac{L|I|^2}{|I|^2 R}, \tag{2.31}$$

such that we may redefine Q as,

$$Q = \omega_0 \frac{L}{R} = \frac{1}{\omega_0 RC}. \tag{2.32}$$

As a measure of the total losses, we may break the quality factor Q down into a number of loss components,

$$\frac{1}{Q_{\text{tot}}} = \frac{1}{Q_i} + \frac{1}{Q_l} + \text{other}, \tag{2.33}$$

where Q_i is the internal quality factor of the resonator in isolation and Q_l is the loaded quality factor.

The loaded quality factor Q_l accounts for the introduction of an additional coupling mechanism, which allows energy to be both added and removed to/from the resonator. For a lumped element resonator, this can be derived as in Ref. [48] as,

$$Q_l = \frac{1}{4} \frac{\pi}{(\omega C Z_0)^2}. \tag{2.34}$$

The internal losses Q_i are attributed to a number of loss mechanisms which sum reciprocally. These are next described.

2.5 Loss mechanisms

Q is highly sensitive to intrinsic losses. This sensitivity is exploited in this work, allowing the detection of the spin ensemble by monitoring Q as a function of magnetic field. The losses due to the spin ensemble are observed in addition to a number of other loss mechanisms. It is, therefore, important that we are aware of these intrinsic losses and their dependencies. These intrinsic losses include: radiation losses, $1/Q_{\mathrm{rad}}$, dielectric losses, $1/Q_{\sigma}$, surface resistivity and kinetic losses, $1/Q_{\epsilon}$ and magnetic field induced losses $1/Q_{B}$. These losses sum reciprocally such that,

$$\frac{1}{Q_i} = \frac{1}{Q_{\mathrm{rad}}} + \frac{1}{Q_{\sigma}} + \frac{1}{Q_{\epsilon}} + \frac{1}{Q_B} + \text{etc.} \tag{2.35}$$

We now discuss these individual mechanisms in further detail, with particular focus paid to magnetic field losses due to the context of this work.

2.5.1 Radiation losses

Radiation losses account for any energy which is not confined within the resonator structure and instead is lost into free space. For a typical CPW resonator, these radiation losses Q_{rad} are approximate of order $10^6 - 10^7$ [48] and are usually considered to be negligibly small [48]. The low loss rates may be explained by the low dipole moment of a typical CPW resonator structure, where currents with opposite polarities flow in close proximity such that radiation produced is screened [49].

2.5.2 Dielectric losses

The dielectric substrate upon which the resonators are fabricated has an associated dielectric constant, ϵ. In the low temperature and low power regime, the primary source

of this dissipation is attributed to two-level-fluctuators (TLF's) - the study of which has been a previous area of speciality within the group [40, 50, 51]. In previous work, it has been demonstrated that at low temperatures, inter-TLF interactions increase and thus the loss rate increases, whereas, at slightly elevated temperatures, there may be less dissipation due to thermal saturation of these TLF's. The exact origin of these TLF's is still an area of active research, however, they are generally agreed to be attributed to the metal-dielectric interface [52, 53]. The losses associated with $1/Q_\epsilon$ are $\tan\delta = -\epsilon'/\epsilon''$. The contribution should not interfere with measurements in this work. However, we should be aware that the TLF's may have magnetic dependencies themselves which may translate to a measurable ESR signal. To avoid this, it is necessary to understand the expected spectra due to the implanted spin ensemble alone, as well as to be aware of the natural substrate impurities and their magnetic dependencies.

2.5.3 Surface resistivity and kinetic losses

The two-fluid model was previously summarised in Section 2.1.1, where it was found that in the regime where $\omega >> \tau_s$, the complex surface impedance is,

$$Z_s = \sqrt{\frac{i\mu_0\omega}{\sigma_n + i\sigma_s}} = R_s + i\omega Ls. \tag{2.36}$$

From this complex impedance, the losses at finite temperatures may be derived as [42, 54],

$$Q_\sigma = \frac{\omega L_s}{R_s} = \frac{n_s}{n_n}\frac{Z_0}{\mu_0\lambda_{\text{eff}}^2\tau_n\sqrt{\epsilon_r}\omega_0 cg}, \tag{2.37}$$

where Z_0 is the characteristic impedance (typically 50 Ω), μ_0 is vacuum permeability, λ_{eff}^2 is the thin film penetration depth, c is the speed of light and g is a geometric factor [55]. The thin film penetration depth, λ_{eff} is defined as $\lambda\coth\left(\frac{d}{\lambda}\right)$, where d is the thin film thickness and λ is the penetration depth of the bulk superconductor. In a

microresonator device, the currents are confined to the edges of the superconductor due to the superconductor penetration depth. This results in an increase in resistive losses associated with $1/Q_\sigma$. We may need to be aware of this, in particular when current paths are further restricted due to applied magnetic fields, as next discussed.

2.5.4 Magnetic field induced losses and effects

Applying static magnetic fields to a superconducting resonator gives rise to numerous additional loss mechanisms. The applied field also changes the basic characteristics of a superconducting resonator. Such effects are particularly prevalent within the scope of this work, where devices will be subject to a slowly changing magnetic field and therefore require particular attention.

In general, the applied magnetic field suppresses the conductivity of the superconductor at a length scale of $\lambda_L(B)$, where λ_L is the London penetration depth. This results in an increased dissipation of currents flowing at the superconductor edge. This is particularly an issue in superconducting microresonator devices, where the current is localised and results in additional dissipation.

Some techniques have been previously developed to improve the Q factors of microresonators in magnetic fields. We may define the losses associated with an applied magnetic field, Q_B as,

$$\frac{1}{Q_B} = \frac{1}{Q_i(B)} - \frac{1}{Q_i(B=0)}. \tag{2.38}$$

We now aim to derive an expression for Q_B. The theoretical work is generally described by the NBI model [56]. The work considers a single superconducting strip of infinite length and of a width W and thickness d. Within the superconductor flows a DC current I_0. The system is subjected to a static magnetic field B perpendicular to the DC current. Despite the discrepancies of this model with our system, we may still use the model with

an additional consideration of the current density distribution of a microwave current within the coplanar strip geometry.

The problem lies in the generation of Abrikosov vortices [57] in a superconducting thin film. Each individual vortex is subject to a different Lorentz force caused by the current flowing nearby and results in a restoring force due to the pinning potential of each vortex and results in additional power dissipation. The energy dissipated is proportional to the current density squared, which can be associated with a change in the Q factor of the resonator. In microwave-carrying superconducting strips, the current density is greatest at the edges. In the same region that the vortex density is also highest. These mechanisms, therefore, result in a considerable amount of dissipation.

Magnetic flux focusing

Flux focusing is a result of the Meissner effect, where for a superconducting strip subject to a magnetic field the magnetic field strength at the superconductor edges is increased, as discussed previously in Chapter. 2.5.4.

In a CPW structure, the ground planes are large compared to the current carrying central conductor. This results in the expelled field being localised within the CPW gaps. As such, the effective magnetic field that the resonator experiences may be orders of magnitude higher than the actually applied field. This is a particularly large problem since it dramatically increases the level of dissipation [58].

Utilising other resonator and ground plane geometries, such as lumped element or fractal resonator designs and dotted ground planes helps to reduce the effects of flux focusing by ensuring there is always a path present which is not enclosed by superconductor to allow for the flux to escape.

Vortex pinning

Magnetic flux may also 'jump' around as it pins and unpins from localised sites. Additional pinning centres may be artificially formed by the addition of holes on the length scale of the penetration depth within the ground plane. These holes provide a strong pinning potential which allows the vortex to stabilise [59] since they are no longer perturbed by the microwave currents. Whilst this technique reduces dissipation, it does not reduce the effect of the flux focusing itself.

Other magnetic field effects

An additional effect when superconducting resonators are subject to a magnetic field includes a shift in the resonator centre frequency. This frequency shift is due to the change of the kinetic inductance within a magnetic field and is approximated from Ginzburg-Landau theory [42], such that the frequency shift may be described as,

$$\frac{\omega(B) - \omega(0)}{\omega(0)} \approx -\alpha \frac{B^2}{B_{c||}^2} \frac{L_k(0)}{L_g + L_k(0)}, \tag{2.39}$$

where α is a proportionality constant, $B_{c||}$ is the parallel critical field, L_g is the geometric inductance (which can be obtained through conformal mapping), and L_k is the kinetic inductance. Typically, superconducting materials with lesser losses in magnetic fields possess a large kinetic inductance, such as NbN. This property is utilised within this work, where superconducting microresonators are subject to external magnetic fields up to 200 mT. Magnetic fields applied parallel to the superconducting plane are also found to be less detrimental to the superconductor, and are therefore used within this work.

Chapter 3

The spin doped crystal system

Having reviewed the superconducting micro-resonator element of the proposed hybrid system, we next explore the memory storage system. As touched upon in Chapter 1, spin-doped crystals are particularly suitable for quantum memory applications, having demonstrated exceptionally long coherence times [60] in the order of seconds.

The crystalline substrate of choice within this project is sapphire (Al_2O_3). This material is chosen due to the low intrinsic concentration of natural impurities, reducing the decoherence in circuit-quantum-electrodynamic (cQED) circuits. This has previously been demonstrated within the group through exceptionally low dielectric loss tangent measurements [50]. This decision greatly influenced the choice of the rare-earth ion to be doped within the crystal.

At the time of commencing this research, very little literature was available on the topic of Al_2O_3 implanted with rare-earth ions. Since this work sought to implement a first-of-a-kind locally implanted hybrid device for proof-of-principle experiments, we wished to work with an experimentally known spin system and Hamiltonian, such that predictions of the system and expected responses could be made. The literature that was available in this area focused on the doping of Gadolinium (Gd^{3+}) [61, 62] in sapphire. As such, the local implantation of Gd^{3+} in an Al_2O_3 substrate became the spin system

of focus within this project.

In this chapter, we begin by exploring the theory behind the Gadolinium spin system. We begin with the rare-earth ion series and focus on the properties of the Gd^{3+} atom. Next, the atomic structure of the sapphire substrate is described, with particular focus paid to the site distributions in preparation for the substitution of the Gd^{3+} ion within the Al_2O_3 substrate. Focus next turns to the locally doped Gd^{3+}:Al_2O_3 system, considering crystal field interactions, and finally presenting the relevant effective spin Hamiltonian utilised throughout the remainder of this thesis.

3.1 Rare-earth ions

Gadolinium lies within the rare-earth series (also known as the Lanthanides) and is located in the 6th period of the periodic table. The series comprises 15 metallic elements with atomic numbers from 57 to 71, specified in Table 3.1. The rare-earths are characterised by a partially filled inner 4f subshell. This partial filling is caused by the strong spin-orbit coupling of the 4f electrons, which makes it energetically favourable to delay the filling of this subshell until the shells of lower spin-orbit energies (6s, 5s and 5p) are filled. Therefore, as the atomic number of the series increases, the 4f shell progressively fills. The outer shells remain constant in a $5s^2 5p^6$ configuration, like a neutral Xenon atom. This partial inner occupation results in an additional magnetic moment which may be utilised for quantum memory applications.

Every second ion within the rare-earth group (namely, Ce^{3+}, Nd^{3+}, Sm^{3+}, Gd^{3+}, Dy^{3+}, Er^{3+} and Yb^{3+}) are Kramers ions. These Kramers ions possess only a twofold degenerate spin ground-state. These degeneracies may be lifted by the application of a DC magnetic field, which may then be accessed through microwave or optical spectroscopy. These Kramers ions are therefore particularly attractive for the application of coupling to superconducting circuits which operate in the microwave regime. Of these ions, Nd^{3+}

Atomic number	57	58	59	60	61	62	63	64	65	66	67	68	69	70	71
Ion	La	Ce	Pr	Nd	Pm	Sm	Eu	Gd	Tb	Dy	Ho	Er	Tm	Yb	Lu
Electron configuration	$5d^16s^2$	$4f^15d^16s^2$	$4f^36s^2$	$4f^46s^2$	$4f^56s^2$	$4f^66s^2$	$4f^76s2$	$4f^75d16s^2$	$4f^96s^2$	$4f^{10}6s^2$	$4f^{11}6s^2$	$4f^{12}6s^2$	$4f^{13}6s^2$	$4f^{14}6s^2$	$4f^{14}5d^16s^2$
Radius (pm)	162	181.8	182.4	181.4	183.4	180.4	208.4	180.4	177.3	178.1	176.2	176.1	175.9	193.3	173.8

Table 3.1 The Lanthanide element series, with inner 4f electron configuration and ionic radius detailed. It is interesting to note the decrease in ionic radius with respect to the increase in atomic number.

and Er^{3+} ions are of particular interest to the field, since their optical transitions are operational in typical fibre-optic telecommunication bands [28]. These properties make rare-earth doped crystals a particularly promising candidate for transducer applications necessary in long-range quantum communications.

3.2 The Gd^{3+} ion

Gd^{3+}, the rare-earth ion of focus in this work, lies in the middle of the rare-earth series with a half filled inner 4f shell: $4f^7$. The associated spin quantum numbers for Gd^{3+} are summarised in Table 3.2. The ground state energy level diagram for Gd^{3+} is shown in Fig. 3.1, where the electron configuration is determined by Hund's rules [63].

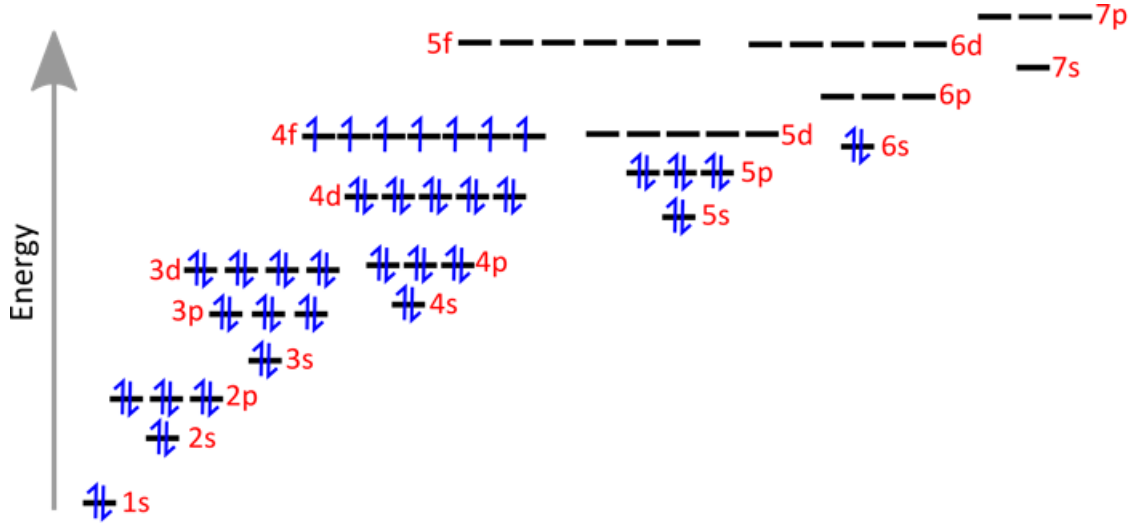

Fig. 3.1 The electronic configuration of the Gd^{3+} atom. As determined by Hund's rules, it is energetically favourable to delay the $4f$ subshell until the 6s, 5s and 5p subshells are filled. In Gd^{3+} the $4f$ level is occupied exactly by half, with a resulting spin 7/2.

n	$l_z =$	3	2	1	0	−1	−2	−3	S	$L = \lvert\sum l_z\rvert$	J	Symbol
7		↓	↓	↓	↓	↓	↓	↓	7/2	0	7/2	$^8S_{7/2}$

Table 3.2 The ground state properties and quantum numbers of the Gd ion.

3.3 The crystallography of sapphire

Sapphire (Al_2O_3) belongs to the ditrigonal-scalenohedral class of the trigonal symmetry (D^6_{3d}). Within this class, Al_2O_3 is hexagonal in form, corresponding to the 3m symmetry point group. This can be seen in Fig. 3.2 (a), which depicts the crystal lattice structure formed of aluminium cations (Al^{3+}) and oxygen anions (O^{2-}). The O^{2-} (represented by blue balls) defines a hexagonal-close-packed (hcp) crystal lattice structure whilst the Al^{3+} cations occupy 2/3 of the octahedral sites in the hcp O^{2-} lattice, see Fig. 3.2 (b). The arrangement of the Al^{3+} and O^{2-} layers in the crystallographic C_3 direction is shown in Fig. 3.3. The parallel planes of O^{2-} ions lie at a distance of 0.2164 nm. Considering each octahedron, the upper three O^{2-} ions are rotated by 64.3° with respect to the three lower O^{2-} ions.

Each grouping of 3 $O^{2-}-O^{2-}$ spacings ranges from $0.252 - 0.287$ nm. The Al^{3+} cations occupy 2/3 of the available octahedral sites to maintain electrical neutrality, whilst the $Al^{3+}-Al^{3+}$ spacing is maximised at a distance of 0.265 nm due to the individual Al^{3+} high charge. The $Al^{3+}-O^{2-}$ distances are 0.197 nm in the c-axis and 0.187 nm in the other 3 directions. The positions of the Al^{3+} ions within the structure are replicated every three layers, and the inter-atomic Al^{3+}-O^{2-}, Al^{3+}-Al^{3+} and O^{2-}-O^{2-} spacings are specified within the magnified selection of Fig. 3.3. The Al^3+ sites between adjacent planes are magnetically inequivalent, ie. b) and c) with a) and f). d) and e) are interstitial sites.

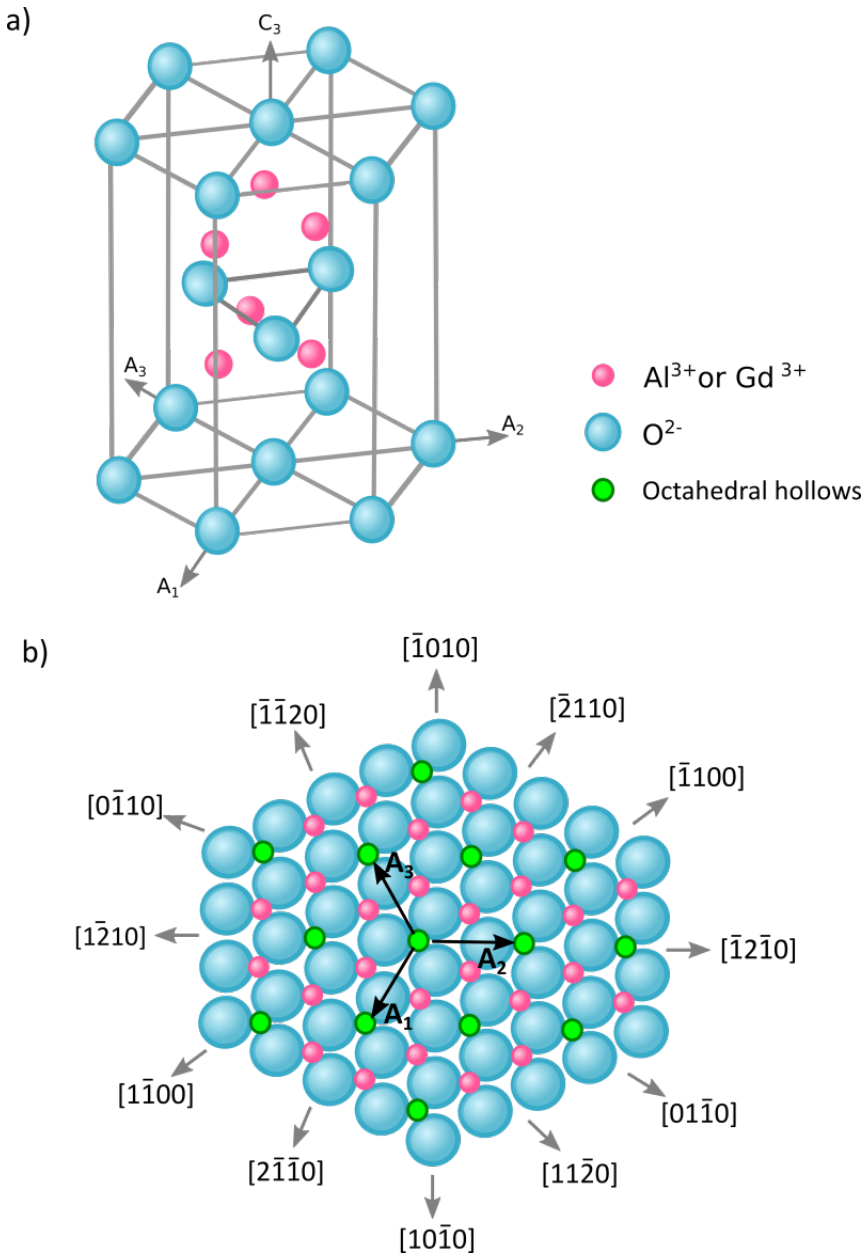

Fig. 3.2 a) A schematic of the Al_2O_3 hexagonal crystal lattice. b) The oxygen anions define a hexagonal-close-packed structure whilst the Al^{3+} cations occupy 2/3 of the octahedral sites in the hcp lattice.

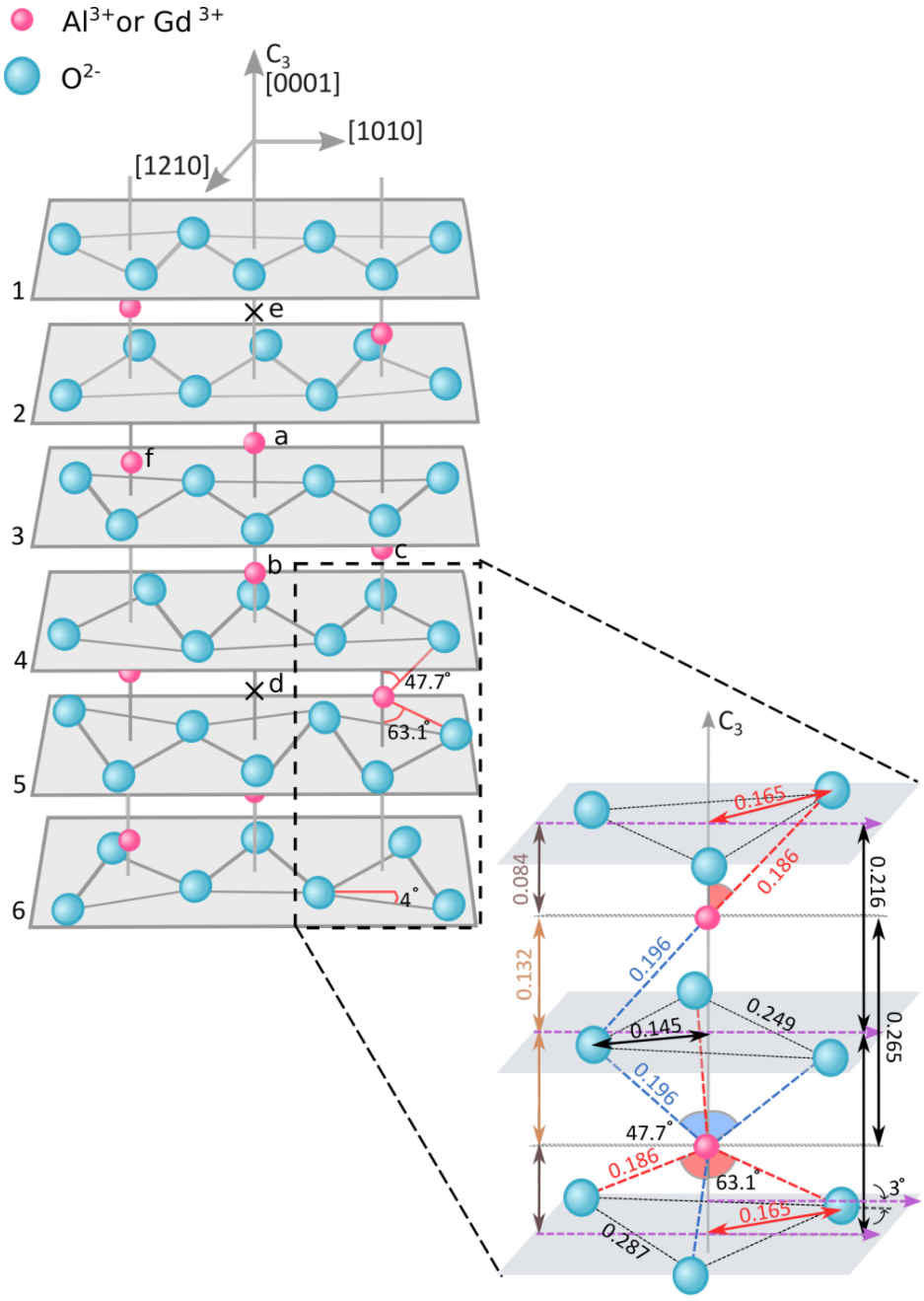

Fig. 3.3 A schematic of the arrangement of Al^{3+} and O^{2-} layers.

3.3.1 The r-cut substrate plane

The Al_2O_3 substrate used in this work is cut in the r-plane, as depicted in Fig. 3.4. Previous resonator measurements performed within the group typical employ an r-plane sapphire substrate, which has been shown to exhibit a low level of losses.

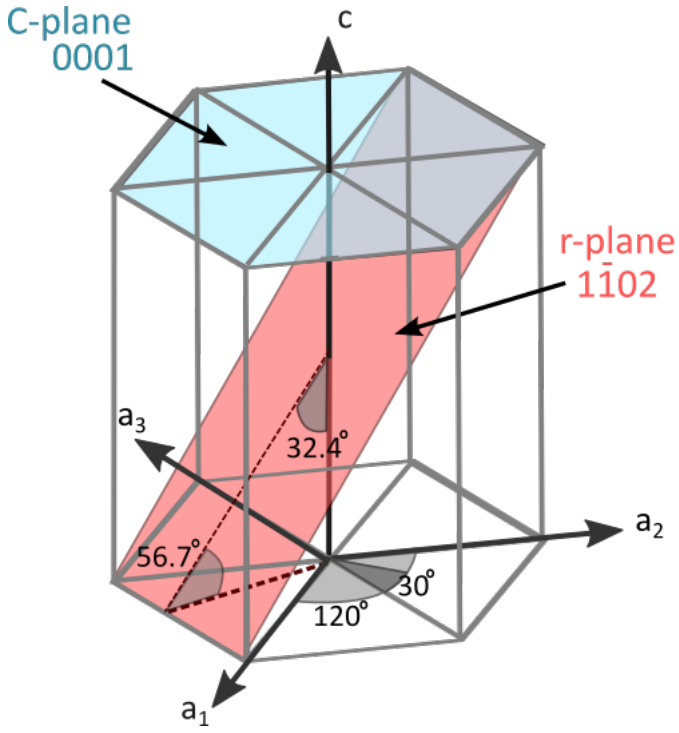

Fig. 3.4 Depicting the sapphire r-plane.

3.3.2 Natural impurities in sapphire

For this work, the Al_2O_3 substrate is chosen specifically due to the low intrinsic concentration of natural impurities. Previous experiments in the group using superconducting microresonator devices fabricated on this substrate have yielded extremely low loss tangents [40, 51, 64] - highlighting the low intrinsic losses within sapphire. Other measurements of Al_2O_3 performed in Ref. [65] used ultra-sensitive microwave spectroscopy at millikelvin temperatures to identify the presence of Fe^{3+}, Cr^{3+} and V^{2+} impurities

within the substrate. For the purpose of this work, it is important to be aware of these impurities, since they may also provide electron-spin-resonance (ESR) responses within our experiments.

3.4 Gd^{3+} doped Al_2O_3

The Al^{3+} sites are available for substitution by another trivalent ion; in our case the Gd^{3+} rare-earth ion. When substituting these sites, it is important to be aware that there are 3 possible structural configurations available, see Fig. 3.5. The 3 sites are all physically equivalent and all have C3 point symmetry. However, the sites differ energetically due to differing bonds between the implanted ion and lattice where within Fig. 3.5 this bond is weaker in (a) than in (b) and stronger in (c) than in (b).

In addition to this, the Al^{3+} sites between adjacent planes of O^{2-} ions are magnetically inequivalent. For example, in Fig. 3.3, sites (b) and (c) are magnetically inequivalent to those on the next plane, (a) and (f), in that their y axes are rotated from each other by nearly 60°. These differences may be of importance when performing our micro-ESR experiments, where ions may couple differently to an externally applied magnetic field due to their crystalline environment.

Whilst these sites are available for substitution, we must next consider the effect that doping of Gd^{3+} may have on the crystal structure. This is particularly worth considering since Gd^{3+} has an ionic radius twice as large as that of Al^{3+}. This raises the question of how severely the environment is distorted, or if the substituted Gd^{3+} is compressed. This was previously explored in works Ref. [62, 66], where Gd^{3+} was grown into an Al_2O_3 lattice. In these works, it was reported that at 'low concentrations' of 100 ppm, Gd^{3+} can enter the lattice without disrupting the overall structure. In this work, the implantation dose is varied around 100 ppm.

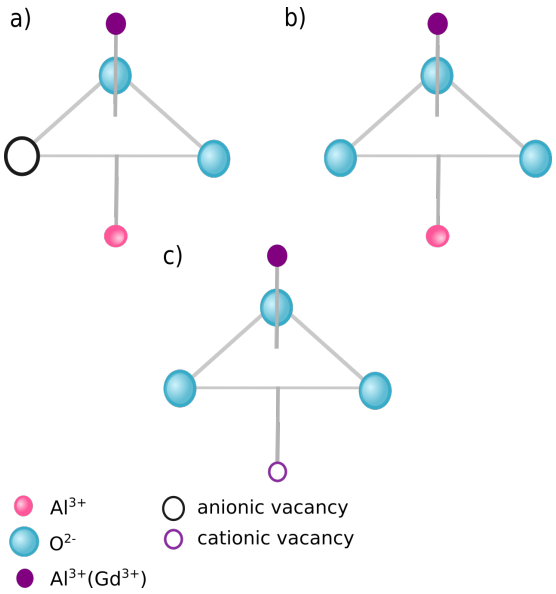

Fig. 3.5 A schematic depicting the 3 available sites for substitution. In a) substitution of Al^{3+} is next to the anionic vacancy, in b) substitution of Al^{3+} is in the regular lattice, and in c) substitution of Al^{3+} next to the cationic vacancy.

3.5 Crystal field interactions

The $4f$ electrons of the implanted rare-earth ion are subject to a number of interactions with their surroundings. These interactions are characterised within the system Hamiltonian by a single-ion interaction term, and a two-ion interaction term. The single-ion interactions act independently at each ionic site. This term does not account for coupling between different ions, which is accounted for within the two-ion interaction which involves two sites i and j.

Since the implanted $4f$ ion is embedded within an number of the surrounding ions, it is subject to an electric field with the local point symmetry. This gives rise to magnetic anisotropies. The crystal field contributes to the potential energy, V_{cf} of a $4f$ electron, e,

$$V_{cf}(\mathbf{r}) = -\int \frac{e\rho(\mathbf{R})}{|\mathbf{r}-\mathbf{R}|} d\mathbf{R}, \tag{3.1}$$

where $\rho(\mathbf{R})$ is the charge density of the surrounding electrons and nuclei. Assuming these do not penetrate the $4f$ charge cloud, $V_{cf}(\mathbf{r})$ is a solution of Laplace's equation, and may be expressed in terms in spherical harmonics as,

$$V_{cf}(\mathbf{r}) = \sum_{lm} A_l^m r^l Y_{lm}(\hat{\mathbf{r}}), \tag{3.2}$$

where A_l^m is,

$$A_l^m = -(-1)^m \frac{4\pi}{2l+1} \int \frac{e\rho(\mathbf{R})}{R^{l+1}} Y_{l-m}(\hat{\mathbf{R}}) d\mathbf{R}. \tag{3.3}$$

It is customary practice to redefine this in terms of Stevens operators $O_l^m(\mathbf{J})$ [67], such that the crystal field Hamiltonian may be written as,

$$\mathcal{H}_{CF} = \sum_i \sum_{lm} B_l^m O_l^m(\mathbf{J_i}), \tag{3.4}$$

where the crystal field parameters B_m^l are constants which may be determined from the experiment. For an ion of C_3 symmetry, the corresponding crystal field parameters are for $l = 2, 4, 6$, and $m = 0, 3, 6$, such that

$$\mathcal{H}_{CF} = B_2^0 O_2^0 + B_4^0 O_4^0 + B_6^0 O_6^0 + B_4^3 O_4^3 + B_6^3 O_6^3 + B_6^6 O_6^6. \tag{3.5}$$

The O_l^m operators are defined as,

$$O_2^0 = 3S_z^2 - S(S+1), \tag{3.6}$$

$$O_4^0 = 35S_z^4 - [30S(S+1) - 25]S_z^2 - 6S(S+1) + 3S^2(S+1)^2, \tag{3.7}$$

$$\begin{aligned} O_6^0 = {} & 231s_Z^6 - 105[3S(S+1) - 7]S_Z^4 \\ & - [105S^2(S+1)^2 - 525S(S+1) + 294]S_z^2 \\ & - 5S^3(S+1)^3 + 40S^2(S+1)^2 - 60S(S+1), \end{aligned} \tag{3.8}$$

$$O_4^3 = \frac{1}{4}[S_z(S_+^+S_-^3) + (S_+3^+S_-^3)S_z], \tag{3.9}$$

$$\begin{aligned} O_4^6 = \frac{1}{4}([11S_z^3 - 3S(S+1)S_z - 59S_z](S_+^3 + S_-^3) \\ + (S_+^+S_-^3)[11S_z^3 - 3S(S+1)S_z - 59S_z]), \end{aligned} \tag{3.10}$$

$$O_6^6 = \frac{1}{2}(S_+^6 + S_-^6) \tag{3.11}$$

It is further customary to redefine the B_l^m operators as specified in Table 3.3.

$b_2^0 = 3B_2^0$	$b_4^0 = 60B_4^0$	$b_6^0 = 1260B_6^0$
$b_4^3 = 3B_4^3$	$b_6^3 = 36B_6^3$	$b_6^6 = 1260B_6^6$.

Table 3.3 The redefinition of the B_l^m operators.

The commonly used second-order zero-field splitting parameters D and E are related to the Stevens coefficients as, $D = 3B_2^0$ and $E = B_2^2$. Further details on the Stevens operators and derivations, can be found in Ref. [67, 68]. These operators are used in defining the effective spin Hamiltonian of our system.

3.5.1 The effective spin Hamiltonian

Gd^{3+} is unique in that it has an s state as the lowest state, therefore the resultant magnetic moment is due to the spin $S = 7/2$. When a magnetic field is applied, the eightfold degenerate state splits in first approximation into 8 equidistant components, where $g = 2$. Since the excited states are no longer S states, they too will be split by any external crystal field into $J + 1$

Stark components. Each component is split by the magnetic field into two Zeeman components. The Zeeman pattern of each absorption line should, therefore, consist of 16 components if no selection rules restrict the number of observable transitions. Assuming the implantation of Gd^{160}, with nuclear spin $I = 0$; the full effective Hamiltonian is given by

$$\mathcal{H} = \underbrace{g\mu_B B \cdot S}_{\text{Zeeman}} + \underbrace{\mathcal{H}_{CF}}_{\text{Crystal field}} , \tag{3.12}$$

where μ_B is the Bohr magneton, B is the magnetic field and the second term is described in terms of higher order crystal field operators, as discussed in the previous section. Eq. 3.12 fully expands as,

$$\mathcal{H} = g\mu_B B \cdot S + B_2^0 O_2^0 + B_4^0 O_4^0 + B_6^0 O_6^0 + B_4^3 O_4^3 + B_6^3 O_6^3 + B_6^6 O_6^6. \tag{3.13}$$

The effective spin Hamiltonian for Gd^{3+} in the Al_2O_3 system was previously determined experimentally in the work of Ref. [62, 66]. In Ref. [62, 66], the B_l^m coefficients were determined experimentally for a polar angle of $\theta = 0$ through standard cavity 4.2 K ESR measurements on grown Gd^{3+} in Al_2O_3. The substrates had a Gd^{3+} impurity concentration of 100 ppm. The results from this work are shown in Table 3.4. In addition, the g factor was found in this work to be $g = 1.9912$ [62]. These parameters provide the basis of the modelling of the experiments in this work, as presented in Section 5.

$b_2^0 = +1032.9 \pm 2.0$	$b_4^0 = +26.0 \pm 1.0$	$b_6^0 = 1.0 \pm 0.5s$
$\lvert b_4^3 \rvert = 18.3 \pm 1.0$	$\lvert b_6^3 \rvert = 5.0 \pm 0.5$	$b_6^6 <= 1.0$

Table 3.4 The Gd^3+ in Al_2O_3 coefficients determined experimentally in Ref. [62, 66].

Chapter 4

Coupling a spin ensemble to a superconducting microresonator

Having considered the superconducting resonance cavity and locally doped spin system independently, we now begin to integrate the hybrid element of this work by considering the coupling mechanism and energy exchange rate between a single spin degree of freedom and the magnetic field of the superconducting microresonator.

In this chapter, we first demonstrate that the coupling rate for a single spin system is orders of magnitude below what is required for coherent information transfer between these systems. We then consider the collective coupling of N_{spins} spins to a resonator, yielding stronger coupling rates, as performed in this work. We next present the temperature dependence of the collective coupling and describe the operational regimes which may be accessible within experiments.

4.1 Single spin coupling

We begin by considering a calculation of the single spin coupling rate of a spin-1/2 to a superconducting resonance cavity mode of frequency ω_0. The single spin coupling rate $\Gamma_{n=1}$ of a spin-1/2 system is given by the product of the magnetic moment μ_s and the vacuum field

fluctuations $\mathbf{B}_{vac}$ [69],

$$\Gamma_{n=1} = \frac{1}{2}\mu_B g \frac{\mathbf{B}_{vac}}{\hbar}, \tag{4.1}$$

where μ_B is the Bohr magnetron, and g is the effective g-factor. $\mathbf{B}_{vac}$ may be calculated by considering the ground state energy $|0\rangle$ of the cavity,

$$\langle 0| \int \frac{1}{\mu_0} |\mathbf{B}_0^2 V_{mode}|0\rangle = \frac{\hbar\omega_0}{2}, \tag{4.2}$$

where μ_0 is the vacuum permeability, $\mathbf{B}_0$ represents the root mean square (r.m.s) magnetic field amplitude of $\mathbf{B}_{vac}$, and V_{mode} is the effective cavity mode volume. This is defined where the electric field per photon is $\approx 1/\sqrt{V_{mode}}$, determining the atom-field coupling strength and is approximately determined by,

$$V_{mode} = \int |f(r)|^2 d^3\mathbf{r}. \tag{4.3}$$

where $f(r)$ is the electric field distribution of the cavity mode evaluated at a given location $\mathbf{r}$. As such, from Eq. 4.2, $\mathbf{B}_{vac}$ can be calculated as:

$$\mathbf{B}_{vac} = \sqrt{\frac{\mu_0 \hbar \omega_0}{2V_{mode}}}, \tag{4.4}$$

such that,

$$\Gamma_{n=1} = \frac{1}{2}\mu_B g \sqrt{\frac{\mu_0 \omega_0}{2V_{mode}}}. \tag{4.5}$$

For the lumped element resonators used in this work, the coupling strength can be estimated using the inductance and the magnetic field dependence of the current: The average current through the inductance L per one oscillation period is $I = \sqrt{E/4L}$, where E is the electromagnetic energy. The fluctuation current may be estimated by substituting $E = \hbar\omega_0/2$, where $f_0 = \omega/2\pi$. The magnetic field may be estimated from this current and may be substituted into Eq. 4.1 to obtain an approximate single spin coupling rate - typically at a rate of order

0.1 Hz. The approximated rate of 0.1 Hz is far too small for coherent information transfer since at these rates a photon would not be absorbed before it leaked out of the cavity.

4.2 Collective coupling: the Tavis-Cummings Hamiltonian

The single spin coupling rate $\Gamma_{n=1}$ may be increased by coupling an ensemble of N_{spins} spins to the magnetic field of the cavity to give a collective coupling rate Γ_n. This system may be described by a simplification of the Jaynes-Cummings Hamiltonian: the Tavis-Cummings Hamiltonian. The Tavis-Cummings model considers the collective coupling of N_{spins} identical spin degrees of freedom to a single cavity [70] in the rotating wave approximation, and is,

$$\hat{\mathbf{H}}_{TC} = \underbrace{\hbar\omega_c \hat{a}^\dagger \hat{a}}_{cavity} + \underbrace{\sum_{k=1}^{N} \frac{1}{2}\hbar\omega_s \hat{\sigma}_k^z}_{spins} + \underbrace{\sum_{k=1}^{N} \hbar\Gamma_{n=1}(\hat{a}\hat{\sigma}_k^\dagger + \hat{a}^\dagger \hat{\sigma}_k^-)}_{interaction}, \tag{4.6}$$

where ω_c, ω_s are the cavity and spin resonance frequencies respectively, $\Gamma_{n=1}$ is the single spin-cavity coupling rate between a single spin k and the cavity field, $\hat{a}^\dagger$ the creation and annihilation operator of the field, $\hat{\sigma_k^+}$ and $\hat{\sigma_k^+}$ are the corresponding operators acting on the spin k, and $\hat{\sigma}_k^z$ is a Pauli operator. The Hamiltonian commutes with the total number of excitations present in the system: $\hat{n} = \hat{a}^\dagger \hat{a} \sum_{k=1}^{N} |\uparrow\rangle\langle\uparrow|$.

In this model, the effective coupling of the ensemble is given by $\Gamma_n = \sqrt{\sum_k^N |\Gamma_{n=1}|^2}$; increasing the resonator-spin coupling rate by the square root of the number of spins. The remaining eigenstates have energies $\hbar\omega_s$ and are antisymmetric combinations of the $|0;\downarrow ... \uparrow_i ... \downarrow\rangle$ states. These remaining eigenstates do not couple into the cavity.

The ideal Tavis-Cummings Hamiltonian is not representative of a real world experiment. This is because the spin ensemble is not a true 'identical' system and instead will take the form of some distribution. There are additional dependencies due to inhomogeneous broadening, crystal magnetic anisotropy and temperature effects. Additionally, the resonator system is

connected to the outside environment, as it is experimentally probed in either transmission or reflection via a Vector Network Analyser (VNA), making it an open quantum system. Assuming measurement in transmission (as in this work), the physical model under consideration may be considered as shown in Fig. 4.1. Here, the bath operators c_i, c_r and c_t represent the incident, reflected and transmitted microwave signal interacting with the cavity of resonance frequency $\omega_c/2\pi$ respectively, such that the signal detected by the VNA in complex transmission is $S_{21} = \langle \hat{c}_t \rangle / \langle \hat{c}_i \rangle$. The cavity has an intrinsic loss rate κ_i and coupling rate κ_c, and the spin ensemble comprises N_{spins} spins with a distribution of spin transition frequencies about a mean frequency $\omega_s/2\pi$ and has a decay rate of FWHM $= \gamma$, assuming a homogeneous spin line-width.

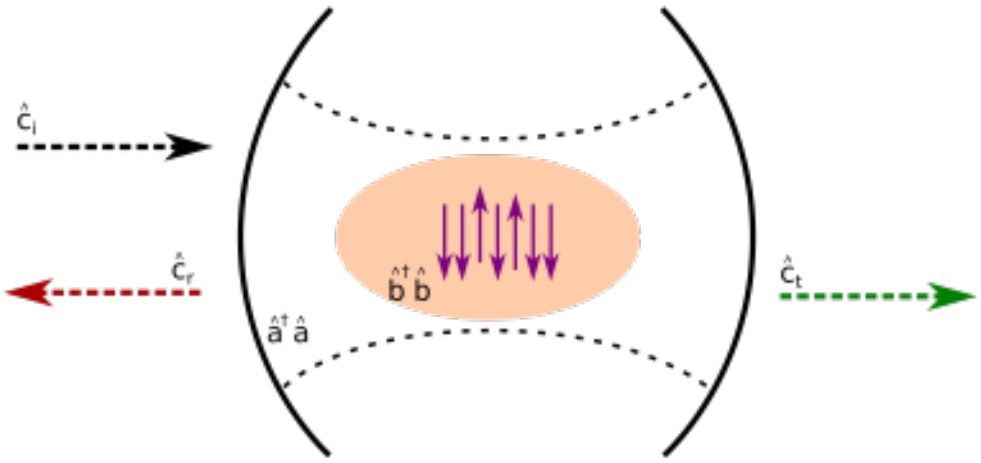

Fig. 4.1 A schematic of a resonator cavity and spin ensemble, coupled to the environment.

Considering the operation of this collective spin system in the few photon limit, the spin operators $\hat{s}_k$ can be considered bosonic by the Holstein-Primakoff approximation [71], $[\hat{b}\ \hat{b}^\dagger] = 1$. The cavity field and collective spin excitation therefore behave as two coupled oscillators [25] with a coupling strength that is enhanced from the single spin coupling rate with a factor $\sqrt{N_{spins}}$. From here, the S_{21} transmission response expression (here, $S_{21} = \langle \hat{c}_t \rangle / \langle \hat{c}_i \rangle$) may be

derived, utilising the Holstein-Primakoff approximation [71],

$$S_{21} = 1 + \frac{\kappa_c}{i(\omega - \omega_c) - (\kappa_c + \kappa_i) - W(\omega)}, \tag{4.7}$$

where $W(\omega)$ is the distribution of spin frequencies. $W(\omega)$ is dependant on the collective coupling strength,

$$W(\omega) = \Gamma_n^2 \int_{-\infty}^{\infty} \frac{\rho(\omega')}{\omega - \omega' + i\gamma} \delta\omega', \tag{4.8}$$

where ρ is the normalized distribution of spin frequencies. Assuming any spin ensemble broadening mechanisms results in a Lorenzian lineshape, we may define the S_{21} as,

$$S_{21} = 1 + \frac{\kappa_c}{i(\omega - \omega_c) - (\kappa_c + \kappa_i) + \Gamma_n^2 / i(\omega - \omega_s) - \Gamma_2^*}, \tag{4.9}$$

where $\Gamma_2^*/2\pi$ is the total inhomogeneous linewidth.

4.2.1 Linewidth broadening

The linewidth γ and shape of the ESR response is intrinsically defined by the interaction between the electron spin and the external magnetic field, as well as by the interaction of the spins within themselves or the sample environment.

There are a number of mechanisms which may contribute to an excessive linewidth broadening. Such linewidth broadening is undesirable and will reduce the coherence time of the spin ensemble, and lower the collective coupling rate. It is therefore highly important to this project that we understand these broadening mechanisms and their corresponding lineshapes.

ESR lines may be broadened either homogeneously (resulting in a Lorentzian line shape), when all spins have the same environment or inhomogeneously (resulting in a Gaussian lineshape) when spins view a different environment. In the current context of cQED hybrid systems, previous experiments have revealed lineshapes between Gaussian and Lorentzian in shape, known as a Voigt profile, and remains an area of active research [21, 72].

We next explore broadening mechanisms which may be particularly relevant to the context of this work:

Inhomogeneous broadening

Many ESR spectra experience inhomogeneous broadening, an effect often caused by variations in the external magnetic field. This may be particularly prevalent in this work, where we consider that the resonator device itself may broaden the ensemble. This is because the superconductor may disrupt the applied magnetic field (due to the Meissner effect) to an order of magnitude significant to the spin ensemble. This disruption may result in magnetic field inhomogeneities which result in different parts of the spin ensemble experiencing differing magnetic fields, effectively reducing the number of spins contributing to the signal at a given magnetic field.
Another cause of inhomogeneous broadening effects are excess spin-spin interactions. These interactions account for all dephasing effects present due to the presence of magnetic fields created by the magnetic dipole bath surrounding a single spin. Dipole-dipole interactions, or strong exchange interactions broaden the absorption due to energy incoherently leaking to other spins within the spin ensemble. This is typically a problem for when the spins are situated in too close in proximity to each other. This results in a Gaussian broadening, and is approximated empirically as,

$$f(\boldsymbol{B}) = \frac{1}{(2\pi\langle \boldsymbol{B_i^2}\rangle)^{1/2}} \exp\left(-\frac{(\boldsymbol{B}-\boldsymbol{B_0})^2}{2\langle \boldsymbol{B_i}\rangle^2}\right). \tag{4.10}$$

where B_0 is the centre field of the lineshape and $\langle \boldsymbol{B_i}\rangle$ is the mean second moment of the line.

Homogeneous broadening

One particular cause of homogeneous broadening within this work may be caused by excess exchange interaction. This becomes prevalent when operating at scales < 0.5 nm - such that the exchange interaction exceeds that of dipole-dipole interaction resulting in 'exchange narrowing'.

This results in a Lorentzian broadening of the lineshape described by,

$$f(\boldsymbol{B}) = \frac{1}{\pi}\frac{\Delta B}{(\Delta \boldsymbol{B})^2 + (\boldsymbol{B} - \boldsymbol{B_0})^2}. \tag{4.11}$$

This is an important parameter to consider when choosing appropriate ion implantation concentrations. Within this work, exchange interaction Lorentzian broadening should not be a problem due to the low concentration of doped ions.

Relaxation times

In the case of performing pulsed ESR measurements, the spin-lattice relaxation time T_1 may be determined and represents the time constant for the equilibration of populations between two electron spin energy levels. The spin-spin relaxation time T_2 represents the time constant for mutual electron spin exchange, which accounts for dephasing mechanisms in the form of spectral diffusion, instantaneous diffusion, spin diffusion, cross relaxation and nuclear spin diffusion effects. Further details of these mechanisms may be found in Ref. [73].

4.2.2 Coupling regimes

The coupling regime is determined by the magnitude of the coupling rate compared to the losses within the resonator (κ) and spin ensemble (γ). An effective quantum memory requires coherent information transfer, where energy is not lost via external energy dissipation channels. We explore the expected responses from the perspective of S_{21} transmission measurements and work under the assumption that the resonator quality factor $1/Q < \gamma$ since we otherwise would not be sensitive to a response. We can explore three regimes, depicted in Fig. 4.2.

We begin with Fig. 4.2 a), where the spin ensemble is strongly coupled to the microwave resonator. Here the coupling strength Γ_n is greater than the linewidths of both the spin ensemble γ and the resonator κ;

$$\Gamma_n >> \kappa, \quad \Gamma_n >> \gamma \tag{4.12}$$

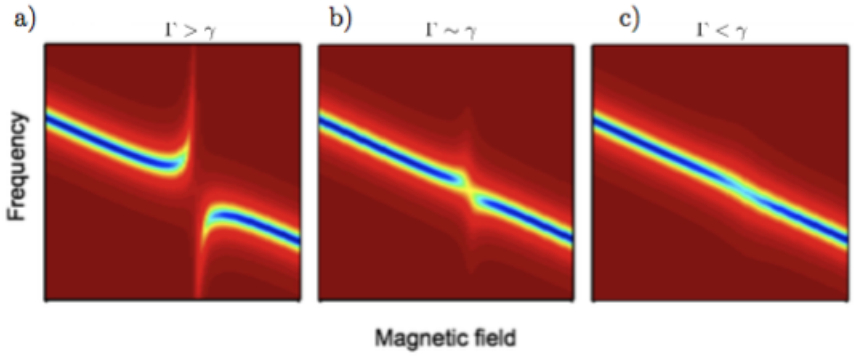

Fig. 4.2 The expected responses in transmission amplitude of a $\lambda/4$ cavity measured in transmission when coupled to a spin ensemble. The responses show various coupling regimes where operating a) in the strong coupling regime, with an observable mode splitting, b) a lesser strong coupling, where Γ is comparable to γ: a frequency shift is observed and c) the weak coupling regime where absorption alone is observed. In all cases $1/Q < \gamma$. Figure taken from [45].

The observed response is a splitting of the resonance modes. In Fig. 4.2 b), Γ_n is comparable to γ, and the splitting has disappeared, however, the frequency shift and increased energy dissipation remain.

$$\Gamma_n >> \kappa, \qquad \Gamma_n \approx \gamma \tag{4.13}$$

In Fig. 4.2 c), the spin ensemble is only weakly coupled to the microwave resonator, such that the coupling strength Γ_n is smaller than the line widths of the spin ensemble,

$$\Gamma_n >> \kappa, \qquad \Gamma_n << \gamma \tag{4.14}$$

Here, the frequency shift is negligible, however, increased dissipations are observed. There is active research to accurately describe the theory of these weak coupling regimes [74]. This is approached in Ref's. [75, 76] as a 'simplified phenomenological treatment of the observed effect'. Weak coupling is likely to be caused by either an inadequate collective coupling rate or due to excessive spin line-widths (factors for which are discussed in a later section).

An inadequate collective coupling rate may be attributable to an inadequate number of spins in the spin ensemble, or alternatively may occur due to an inadequate microwave field distribution. This may result in magnetic field inhomogeneities, attributable to the Meissner effect, resulting in inconsistencies in the magnetic field magnitude across the spin ensemble. As a consequence of this, a lesser number of spins may be available for coupling, therefore reducing Γ_n.

4.2.3 Temperature dependence of collective coupling

Whilst the experiment is performed in the low-power, low-temperature regime, there will be some finite temperature effects determining the energy level population within the spin system. This may be described by the Boltzmann distribution,

$$P(|x\rangle) = \frac{\exp\left(-E_{\uparrow,\downarrow}/k_\beta T\right)}{\exp\left(-E_\uparrow/k_\beta T\right) + \exp\left(-E_\downarrow/k_\beta T\right)}, \tag{4.15}$$

where the ground state energy $E_\downarrow = -\frac{1}{2}g\mu_B B$ and $E_\uparrow = +\frac{1}{2}g\mu_B B$.

The collective coupling strength Γ_n is proportional to the difference between the number of thermally excited spins and the number in the ground state. Assuming a perfect paramagnet (ie. negligible spin-spin interaction), this fraction is both temperature and magnetic field dependant, and can be derived from the Fermi distribution as,

$$\Gamma_n = \Gamma_n(T=0)\sqrt{\tanh\left(\frac{g\mu_0 B}{2k_B T}\right)}. \tag{4.16}$$

Chapter 5

Modelling techniques and methods

Before beginning experimental investigations, it is useful to simulate the system to assist in obtaining a thorough understanding of the system. This will help to determine if the chosen system is capable of the desired operation, as well as assists in providing some guidance to the design process. We may also utilise these simulations later in making comparisons between the experiment and theory. This may assist in identifying any discrepancies which may occur between the two.

We begin with a simulation of the expected spectral response of the system. This is performed with the assistance of the software package, EasySpin. We next explore the expected collective coupling strengths (Γ_{coll}). This is a particularly interesting parameter to extract since it will provide assistance in design parameters (ie. the number of spins required) and provide an idea of what coupling regime we may expect to operate in during the experiment, see Section 4.2.2.

5.1 Simulating the continuous wave electron spin resonance spectra

We first wish to explore the expected magnitudes of the magnetic fields required to bring the spin system into resonance with a typical superconducting microresonator. To model the expected spectra, we use 'EasySpin' [77], an ESR simulation package which runs with

MATLAB. EasySpin defines a basic workflow for setting up the ESR environment with a collection of functions. These functions assist in the back-end computation and visualisation of the resulting spectra. EasySpin is primarily created for the simulation of 'standard' cavity-ESR experimental set-ups. Since our system takes the form of an implanted crystal and the cavity is a microresonator device, careful consideration must be given to accurately describe the set-up in the case of this work. Further details of the software package can be found in Ref. [78, 79]. This section first summarises the key concepts and functions of the EasySpin software. The functions are then broken down and described in relation to our spin and experimental systems. Particular consideration is given to any changes from the standard EasySpin procedure which are required due to the use of the microresonator device as a cavity. Finally, the simulation methods and results are discussed.

5.1.1 An overview of EasySpin

EasySpin operates using parameters which are input by the user through a number of functions within higher primary arguments. Three primary arguments are used to express the key features of the simulation: the physical regime of operation (ie. solid state, semi-rigid, powder), the spin system, and the experimental setup. The spin system argument (`'Sys'`) and experimental argument (`'Exp'`) further breakdown into multiple functions which allow the user to provide parameters accurately representative of the overall system within the simulation.

Operationally, the simulation of a field-swept cw EPR spectra is performed using the function `'pepper'`. This function supports spin systems governed by the spin Hamiltonian:

$$H = \sum_i \left[\hat{H}_{EZI(i)} + \hat{H}_{ZFI(i)}\right] + \sum \left[\hat{H}_{NZI(i)} + \hat{H}_{NQI(i)}\right] + \sum_i \sum_{j>i} \hat{H}_{EEIi,j)} + \sum_i \sum_k \hat{H}_{HFI(i,k)} \quad (5.1)$$

where,

$\hat{H}_{EZI(i)}$ is the Electron Zeeman Interaction of electron spin i,

$\hat{H}_{ZFI(i)}$ is the Zero-Field Interaction of electron spin i (for systems with more than one electron spin ($S > 1/2$), reflecting the strong dipole-dipole interaction between the electrons),

$\hat{H}_{NZI(i)}$ is the Nuclear Zeeman Interaction of nuclear spin k,

$\hat{H}_{NQI(i)}$ is the Nuclear Quadrupole Interaction of nuclear spin k,

$\hat{H}_{EEI(i)}$ is the Electron-Electron Interaction between electron spins i and j,

$\hat{H}_{HF(i)}$ is the Hyperfine Interaction between electron spins i and nuclear spin k.

The appropriate spin Hamiltonian is defined by the user, within a number of primary arguments as discussed later in this Chapter. The spectra are then computed using a triangular grid and the function `'resfields'` to determine the energy eigenvalues and eigenstates using matrix diagonalisation. The resonance fields and line intensities are hence determined with energy level diagram modelling.

We next break down these primary arguments into the functional inputs required to accurately portray our expected experimental parameters. The MATLAB code used to produce the final simulation is provided in Listings at the end of each section where relevant.

5.1.2 The physical regime

In this work, the spin system comprises locally implanted Gd^{3+} within a crystalline Al_2O_3 substrate. Since this is a solid-state spin system, the simulation operation mode is defined as in the 'solid-state rigid-limit' through the use of the EasySpin function, `'pepper'`.

5.1.3 The spin system

The spin system parameters are input into the simulation using the EasySpin argument `'Sys'`. The spin system parameters used as a starting point for the simulation are extracted from

```
1  %Input spin Hamiltonian Stevens operators
2  uc = 2.998; % Conversion from cm-1 to Mhz
3  Sys.B2 =[0 0 1032.9*uc/3 0 0];
4  % B20: q = +2 +1 0 -1 -2
5  Sys.B4=[0 18.3*uc/3 0 0 26.0*uc/60 0 0 18.3*uc/3 0];
6  % B40,3: q = +4 +3 +2 +1 0 -1 -2 -3 -4
7  Sys.B6=[ 5.0*uc/1260 0 0 1.0*uc/36 0 0 1.0*uc/1260 0 0 1.0*uc/36 0 ...
       0 5.0*uc/1260];
8  % B60,3,6: q = +6 +5 +4 +3 +2 +1 0 -1 -2 3 -4 -5 -6
9
10 Sys=('S',7/2,'g',1.9912,'Nucs','160Gd');
11 % Specification of the electron spin quantum number, g-factor and ...
       isotope
12 Sys.lw = 1; % approximate spin linewidth is specified in mT
```

Listing 5.1 Spin parameters (`'Sys'`) chosen as input to EasySpin, specifying the Gd^{3+} in Al_2O_3 spin system.

Ref. [62]. When comparing this model to experimental results, the spin system parameters may need optimising since the physical crystalline systems may differ. This is particularly probable due to the difference in doping techniques between our work and that of Ref. [62] - where doping is achieved through growth in Ref. [62], and by implantation in ours. The parameters specified by this argument include:

	Listing 5.1
The spin centre: which is specified to simulate the Gd^{3+} ion of isotope Gd^{160}.	line 10
The spin quantum number, which for a Gd^{3+} ion is 7/2.	line 10
The associated nuclear spin, which for the specified Gd^{3+} isotope is $I = 0$.	line 10
The g-value: $g = 1.9912$ as reported in Ref. [62].	line 10
The Spin Hamiltonian: here specified through the definition of Stevens operators (as previously described in Section 4.2 and previously determined experimentally in Ref. [62, 66]).	lines $2 - 8$
The line-width broadening: Since the resulting experimental line-width is unknown, an arbitrary FWHM value of 1 mT is specified.	line 12

5.1.4 The experimental system

The experimental settings required to define the system are input using EasySpin argument `'Exp'`, which contains a number of functions:

	Listing 5.2
The superconducting microresonator centre frequency, f_0 (equivalent to the spectrometer frequency in standard ESR) is specified using the input argument `'Exp.mwFreq'`(GHz). For this work, a value between $2-8$ GHz is chosen.	line 4
The magnetic field ranges over which we wish to compute the spectra is specified. Reasonable static magnetic field values applied to tune the spin ensembles are from 0 to ≈ 200 mT. These values are input in the argument `'Exp.Range'` (mT)	lines 1-3/6
The number of points to be calculated in the spectrum is specified in the argument `'Exp.nPoints'` and is set to 400, for 0.5 mT resolution in this preliminary investigation.	line 7
The spectrum format (ie. the choice of spectral output in either absorption or first harmonic mode) is required. Since we expect the experimental output as an absorption trace, this argument is input as `'Exp.Harmonic = 0'`.	line 9
The temperature at which the experiment is performed: this is expected to range from 10-300 mK and is specified though the argument `'Exp.Temperature'`. This allows EasySpin to include the relevant polarisation factors resulting from thermal equilibrium population of energy levels. For preliminary modelling investigations, this is specified as $T = 0.3$ K.	line 8

```
1 Bstart = 0; % magnetic field start value (mT)
2 Bstop = 200; % magnetic field end value (mT)
3 Fieldrange = [Bstart Bstop]; % in mT
4 MWFreq=3.34; % microwave frequency in GHz
5
6 Exp =('mwFreq',MWFreq,'Range',Fieldrange); %specify argument of ...
      microwave frequency and magnetic field range
7 Exp.nPoints = 400; %specify number of points to determine ...
      simulation resolution
8 Exp.Temperature =0.3; % experimetal temperature (K)
9 Exp.Harmonic=0;% Specify to plot absorbtion trace
```

Listing 5.2 Indicating the experimental parameters (`'Exp.'`) chosen

In addition to these physical parameters, the crystal orientation and the cavity 'operational mode' must also be defined. Definition of these parameters becomes more complex due to the use of a microresonator device. This is explained further in the following subsections.

Crystal orientation and the relative reference frames

We begin by considering the crystal orientation within the experimental set-up. During the ESR spectroscopy, a static magnetic field B_0 is applied in parallel to the crystal substrate, which is mounted vertically within the cryostat. This means that the B_0 field is applied in the crystal r-cut substrate plane. To specify this within EasySpin requires the definition of the relative orientations between a number of given reference frames. These reference frames comprise,

the laboratory frame: $L_\mathrm{f} = [x_\mathrm{L}, y_\mathrm{L}, z_\mathrm{L}]$,

the crystal frame: $C_\mathrm{f} = [x_\mathrm{c}, y_\mathrm{c}, z_\mathrm{c}]$,

and the molecular frame: $M_\mathrm{f} = [x_\mathrm{M}, y_\mathrm{M}, z_\mathrm{M}]$.

EasySpin operates such that L_f is a fixed reference frame. C_f is therefore defined with respect to L_f and M_f with respect to C_f. The relative orientations of these frames are defined by Euler transformations $[\alpha, \beta, \gamma]$.

The laboratory frame

By convention in standard cavity-ESR, z_L is defined along B_0 whilst x_L and y_L are parallel to the oscillating microwave field components (B_{1x} and B_{1y}), see Fig. 5.1(a).

The crystal frame

The crystal frame relative orientation is specified relative to L_f using the function `'Exp.CrystalOrientation'`, as shown in Listing 5.3 (lines 1-4). Experimentally, the r-cut Al_2O_3 plane ($1\bar{1}02$ in Miller indices) is mounted such that B_0 acts within this plane. The r-plane is shown in Fig. 5.1(b) and intersects with the crystalline c-axis at an angle of 32.4° and an angle of 56.7° to the normal. The plane is rotated about the c-axis by 30° from the crystalline a_2 axis.

Working under the assumption that the oscillating microwave field and laboratory frame x_L axis coincide with the crystallographic a_1 axis, a transformation in Euler angles of $[\alpha, \beta, \gamma] = [30, 32.4, 0]$ (degrees) is required to align the relative axis, as shown schematically in Fig. 5.1(c).

The molecular frame

The molecular frame defines the orientation of the spin centre within the crystal, which rarely aligns with that of the crystal axes. This information is modelled using the EasySpin field `'Exp.MolFrame'`. The spin centre orientation was unknown and for preliminary investigations was assumed to coincide with the crystal frame. This is shown in Listing 5.3 (line 5).

The operational mode

Standard cavity continuous wave (cw) ESR resonators operate in either perpendicular or parallel mode. In perpendicular mode the static applied magnetic field B_0 is perpendicular to the oscillating microwave components $B_{1\mathrm{x}}$ and $B_{1\mathrm{y}}$. In parallel mode, intuitively, B_0 acts parallel to an oscillating microwave component. Typically, most standard ESR measurements are performed in parallel mode.

We now consider the mode of operation in our experiment, where the standard ESR cavity is replaced with a superconducting lumped element microresonator. It becomes clear that

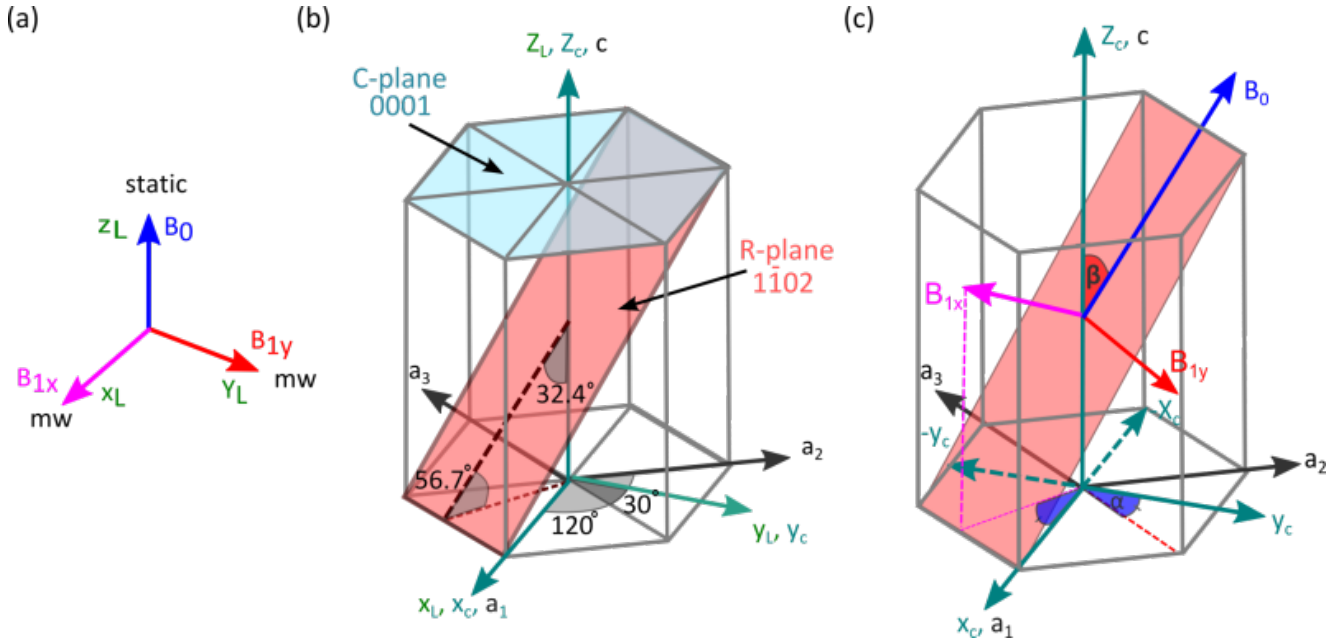

Fig. 5.1 Showing the relative orientations of the experiment (a) The laboratory frame $L_{\mathrm{f}} = [x_{\mathrm{L}}, y_{\mathrm{L}}, z_{\mathrm{L}}]$ is defined by a right-hand cartesian coordinate system where the static magnetic field, B_0 (blue) acts along z_L and is perpendicular to the oscillating microwave magnetic field components which act in y_L and x_L. (b) Depicts the Al_2O_3 hexagonal unit cell, where the r-plane $(1\bar{1}02)$ is highlighted (light red). The hexagonal crystal axes $(a_1, a_2, a_3$ (black)) are 120° apart. The r-plane intersects the crystalline c-axis at an angle of 32.4° angle and the c-plane (light blue) at an angle of 56.7°. The crystal reference frame z_{c} and x_c-axes (turquoise) share the c and a_1 axes (black) respectively. y_{L} is therefore at an angle of 30° from a_2 and a_3 in the c-plane. Initially within Easyspin, the laboratory frame is assumed to coincide with the crystal frame. (c) A transformation is required to align the crystal frame within the laboratory frame, since the applied magnetic field is orientated in the r-plane. To align the axes, a transformation in Euler angles of $[\alpha, \beta, \gamma] = [30, 32.4, 0]$ degrees is required (as shown in purple and red angle transformations), bringing B_0/z_{L} and $B_{1\mathrm{y}}/y_{\mathrm{L}}$ into the r-plane.

```
alpha = 30;
beta = 32.4;
gamma = 0;
Exp.CrystalOrientations = [alpha beta gamma]*pi/180; % relative ...
    orientation between $C_{\text{f}}$ and $L_{\text{f}}$ (in Rad)
Exp.MolFrame = [0 0 0 ]*pi/180; % relative orientation between ...
    $M_{\text{f}}$ and $C_{\text{f}}$ (in Rad)
Exp.Mode = 'perpendicular' % When operating the system in ...
    perpendicular mode
Exp.Mode = 'parallel' % When operating the system in parallel mode
```

Listing 5.3 The experimental parameters (`'Exp.'`) input in to EasySpin to define the various frame orientations.

the definition of operational mode is more complicated due to the LE resonator device. This is because the LE device is patterned with an inductive meander, as depicted in Fig. 5.2(a). The meander geometry results in a change in the orientation of the oscillating microwave field components with respect to a static applied B_0 where current flows both parallel (5.2(b)(i)) and perpendicular (5.2(b)(ii)) to B_0. In the case i), B_{1x} and B_{1y} are always perpendicular to B_0, and therefore is accurately modelled in EasySpin operating in `'perpendicular mode'`. However, in the case ii), current flows perpendicular to B_0, such that the oscillating microwave field components act both perpendicular and parallel to B_0.

It is, therefore, evident that in order to accurately model this system in EasySpin, operation in both `'parallel mode'` and `'perpendicular mode'` must be calculated.

5.1.5 Simulation of the Gd^{3+}:Al_2O_3 micro-ESR spectra

Confidence is next gained in the EasySpin simulation by replicating the results of Ref. [62] with our simulation (see Appendix B). The experimental results were accurately simulated using this simulation, therefore we may next perform simulations in relation to our experimental set up with good confidence. We here present the results obtained from these simulations.

We begin with an example of a single EasySpin calculation: an energy level diagram Fig. 5.3(a) and resulting spectral output Fig. 5.3(b). The highlighted lines between the energy level

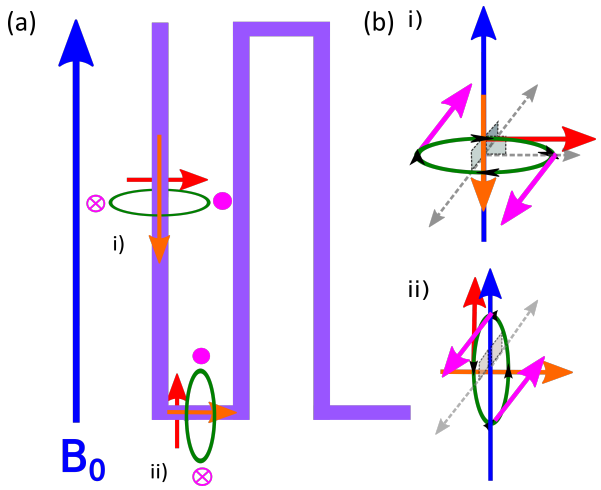

Fig. 5.2 The orientation of B fields in the micro-ESR experiment (a) A schematic of a lumped element resonator inductive meander (purple) coupled to a locally implanted spin ensemble beneath it. The microwave current (orange) flows through the inductive meander (purple) with oscillating microwave field components (green circles) in B_{1x} and B_{1y}. (b) Assuming B_0 is applied in the plane, as shown, there are two operational component modes (i) where current flows parallel and (ii) where current flows perpendicular to B_0. i) In the case where current flows parallel to B_0, all oscillating microwave field components are perpendicular to B_0, therefore the system operates in EasySpin is defined `'perpendicular mode'`. In case (ii), the current flows perpendicular to the applied field B_0. The oscillating microwave field component operates both parallel and perpendicular to B_0. This requires simulations in EasySpin to operate in both `'perpendicular'` and `'parallel'` modes. It must be appreciated that this is an idealised situation, where there will be intermediate modes at corners.

transitions (grey-red) represent transitions where energies match that of the photon energy from the superconducting microresonator centre frequency. The grey lines represent weaker transitions, and the red lines higher intensity transitions. This energy level diagram is translated into an ESR spectra in the lower panel, where the relative intensity of the accessible transitions is depicted more clearly.

From Fig. 5.3, we can be assured that there are multiple accessible transitions available to us within an experimentally accessible applied magnetic field limit of 200 mT. We also observe that the accessible transitions span many energy levels, and are not limited to the ground state. This is an interesting observation, since the energy level populations are temperature dependent (see Section 4.2.3), so it may be interesting to explore the transition intensity with respect to temperature.

This calculation may be performed many times with respect to individual changes in experimental parameters. Our experimental set-up includes a vector magnet, which allows for rotation in planes α, β, γ. It is therefore of particular interest to explore what effect such rotations of the static applied magnetic field yields on the spectra.

Spectra are calculated with respect to a change in the angle of the applied static magnetic field B_0 from 0 to 360 degree rotation. This angular change may be rotated in α, β and for γ, and are independently simulated, whilst maintaining the required α and β angles to replicate the r-cut sapphire, as discussed in Section 5.1.4. The results (inclusive of both parallel and perpendicular operational modes) are shown in Fig. 5.4, where we present a 'top-down' view of an individual ESR spectrum (as previously shown in Fig. 5.3(b)).

From Fig. 5.4, we observe that a change in β (a rotation within the r-plane) presents the most interesting spectral features to study, with plenty of transitions accessible within a magnetic field limit of 200 mT. Again, the spectra contain many unique features with multiple energy level transitions. Replicating this spectrum within an experiment would provide many transitions to compare with modelling and should help to identify any discrepancies between the simulation and results. The model may then be further utilised by exploring changing to other individual parameters, such as the Stevens operators or 'molecular orientations', which may identify where

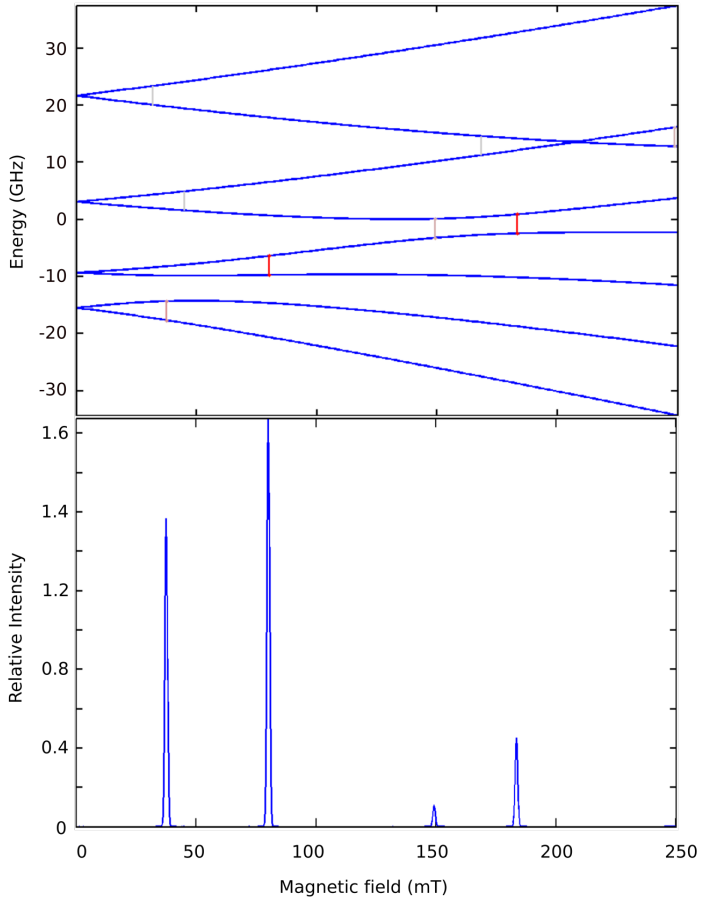

Fig. 5.3 An EasySpin calculation, as directly displayed by EasySpin. Upper panel: the calculated energy level diagram of Gd^{3+} in Al_2O_3, the transitions highlighted in red are frequency matched to the resonator centre frequency in this example. The transitions are colour mapped with respect to relative intensity, as displayed by EasySpin. Lower panel: an example of the ESR spectra with the relative intensities of the individual transitions obtained from the energy level diagram presented above.

any such discrepancies may originate.

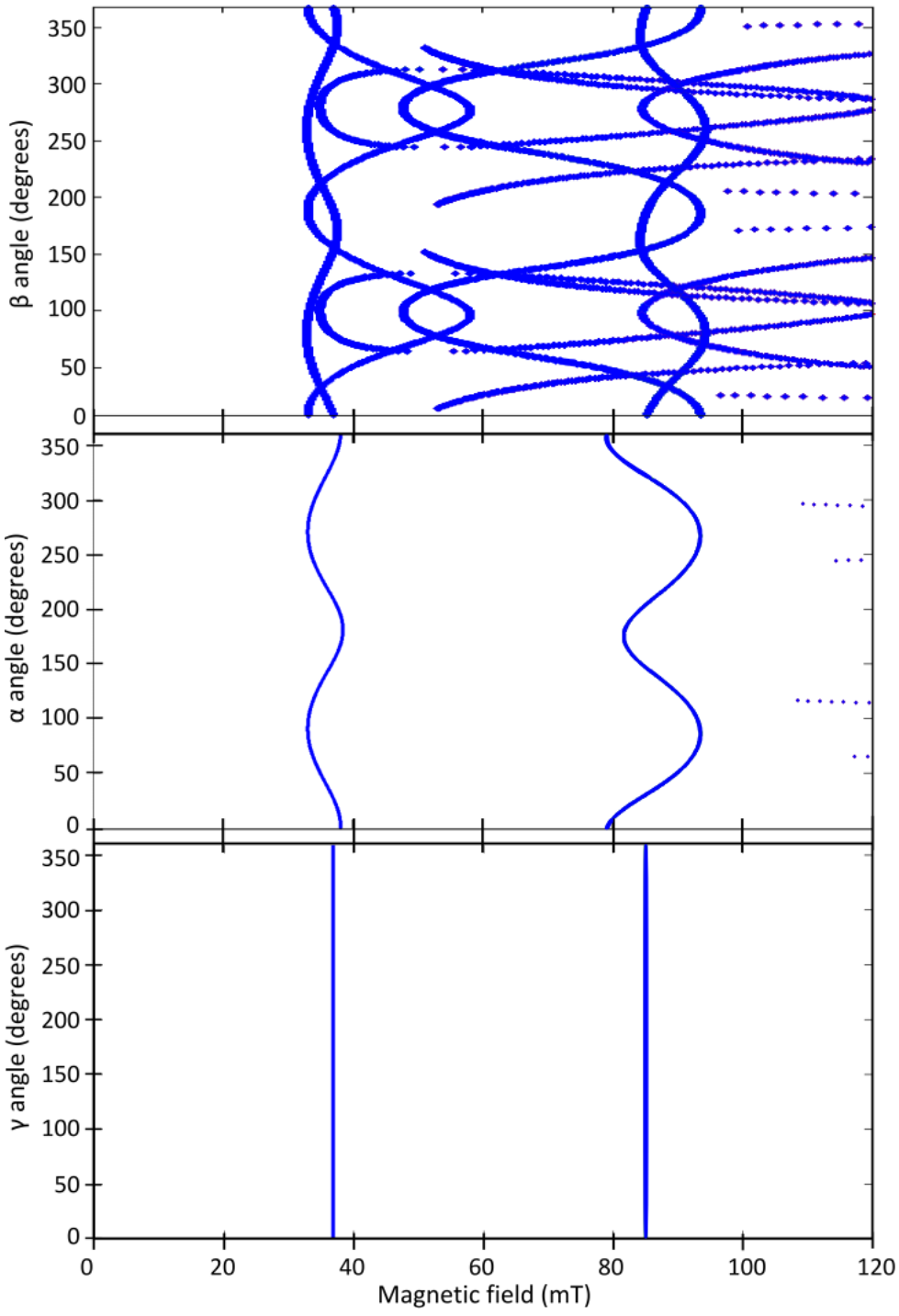

Fig. 5.4 EasySpin simulations depicting the expected ESR spectral positions for an r-plane Gd^{3+} in Al_2O_3 system, with respect to a changing B_0 angle in β, α and γ.

5.2 Numerical modelling of the collective coupling strength

We next seek to model the expected collective coupling strengths (Γ_{coll}) achievable from our experimental system. This is an important parameter to estimate since the outcome will determine the coupling regime we may operate in, and thus the scope of experiments available to us.

Determining an accurate model for Γ_{coll} in our experimental set-up is not trivial. Where we have a locally implanted spin ensemble coupled to a lumped-element resonator geometry, there are variations in both spin and magnetic field density due to the implantation and resonator geometry respectively. As a result of this, each individual spin will experience a slightly different single spin coupling rate. To model Γ_{coll} more accurately, it is beneficial to independently model the spin density distribution and magnetic field distribution as a function of the volume used, $\rho(v_{spin})$ and $H(v_{spin})$ respectively, before evaluating over the volume of interest. The explicit code can be found in Appendix C. A description of the operation of the code follows.

5.2.1 Evaluating the magnetic field distribution

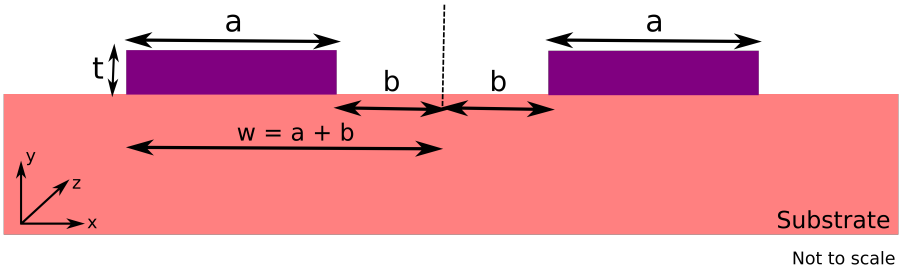

Fig. 5.5 A schematic representative of a cross-section of two inductive meanders of film thickness (t), of a width = a and spacing = $2b$, such that $W = a + b$.

We begin with an approximate calculation of the magnetic field distribution. This is determined by the geometry of the resonator device and the inductive meander. For simplicity we consider

the inductive meander geometry for the computation of coupling as two parallel current carrying strips. The strips are of film thickness, t and width a. The spacing between the parallel strips is $= 2b$, such that the total width $W = a + b$ as depicted in Fig. 5.5. The current I_0 flows along the parallel strips in opposite ($\pm z$) directions. When the strips carry current and are subjected to an applied magnetic field, the resulting magnetic field $\boldsymbol{H}$ is two dimensional and can be expressed as $\boldsymbol{H}(x, y) = \hat{x}H_x(x, y) + \hat{y}H_y(x, y)$ [80]. This can be described using analytic functions $\bar{H}(\zeta) = H_y(x, y) + iH_x(x, y)$ of the complex variable $\zeta = x + iy$. We may assume the magnetic field penetration into the superconducting strips makes only a negligible perturbation of the magnetic field distribution. Under these conditions, the situation may be expressed as [45, 80],

$$H(\zeta) = -H_0 \frac{W^2}{\sqrt{(\zeta^2 - b^2)(\zeta^2 - W^2)}}, \tag{5.2}$$

and evaluated in the real and imaginary parts. To do this, the constant H_0 (the magnetic field intensity at $\zeta = 0$) must first be determined. H_0 may be extracted from the corresponding current density of the magnetic field profile,

$$J_z = \frac{2H_0}{d} \frac{x}{|x|} \frac{W^2}{\sqrt{(x^2 - b^2)(W^2 - b^2)}}, \tag{5.3}$$

where H_0 is the magnetic field intensity at $\zeta = 0$, when the resonator is populated by a single photon. To find the total current I_t, we integrate the current density along the strip, which gives the relation for H_0 in terms of I_0,

$$H_0 = \frac{\mu_0 I_0}{2W\kappa\sqrt{1 - b^2/W^2}}, \tag{5.4}$$

where $I_0 = \sqrt{\hbar\omega/2L}$ is the current due to a single photon; where $\omega = 2\pi f_0$ and L is the superconductor inductance, $L = z/w_0$, where z is the material impedance.

The resulting magnetic field distribution is evaluated within the desired limits of the spin ensemble volume as $H(v_{spin}) = |H(x, y)/H(x, 0)|^2$ to provide a resulting magnetic field distribution profile.

A COMSOL approach

Another approach to modelling the magnetic field distribution is utilising COMSOL multiphysics software to simulate the electromagnetic field of the LE device, making use of the RF module. The resulting simulation is shown in Fig. 5.6. It is easy to see how the magnetic field distribution changes dramatically within the substrate. Since we wish for the spin ensemble to experience as close to the constant magnetic field as possible, we use this simulation to determine an optimal depth for the ion implantation: ranging from $150 - 250$ μm. This range is highlighted in purple within Fig. 5.6.

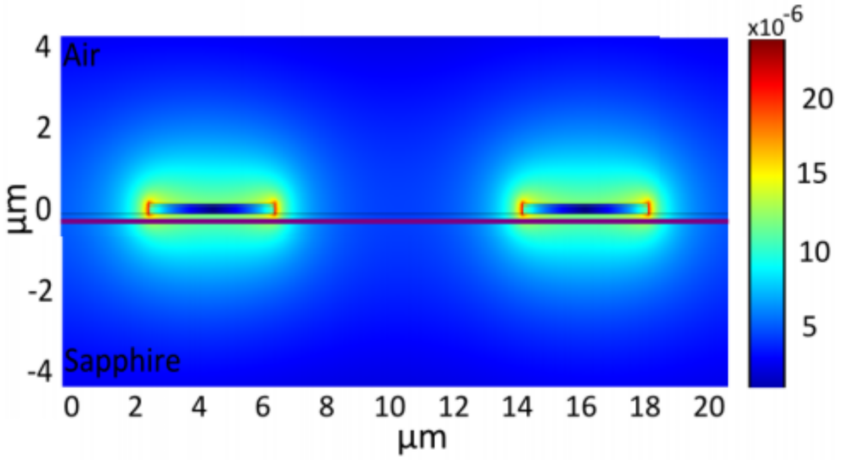

Fig. 5.6 A COMSOL multiphysics calculation of the electromagnetic field of two inductors within an LE device. The potential region for implantation, with relatively constant electromagnetic field under the inductive strips, is highlighted in purple ($150 - 250$ nm).

5.2.2 Evaluating the spin distribution

The spin ensemble available for coupling is locally implanted within our sapphire substrate. The implantation procedure (discussed in Section 6) results in a variation in the spin density with respect to the depth of the implantation, y. The implantation concentration profile can be

approximated as,

$$C_y = C_p \exp^{-(y-R_p)^2} / 2\gamma_p^2, \tag{5.5}$$

where R_p is the peak implantation depth and C_p is the peak spin concentration, which can be expressed as $C_p = \frac{d_i}{\sqrt{2\pi}\gamma_p}$, where d_i is the implantation dose in spins/m^2 and γ_p is the FWHM. The concentration profile is converted into a spin density distribution by consideration of the proportion of lattice sites available for substitution which are occupied in the substrate. Where in sapphire, the substitutionally accessible site density, $\rho_s = 1.4 \times 10^{28}$ m^{-3}. Assuming an implantation dose (as in Section 6) of $d_i = 10^{14}$ cm^2, a peak implantation depth of 160 nm and a linewidth of 33 nm, the resulting spin density profile is shown in Fig. 5.7. The total number of spins available for coupling across the given volume N_{spins}, can then be extracted by an integration of $\rho(v_{spin})$ in y. This is then multiplied by the area of implanted spins.

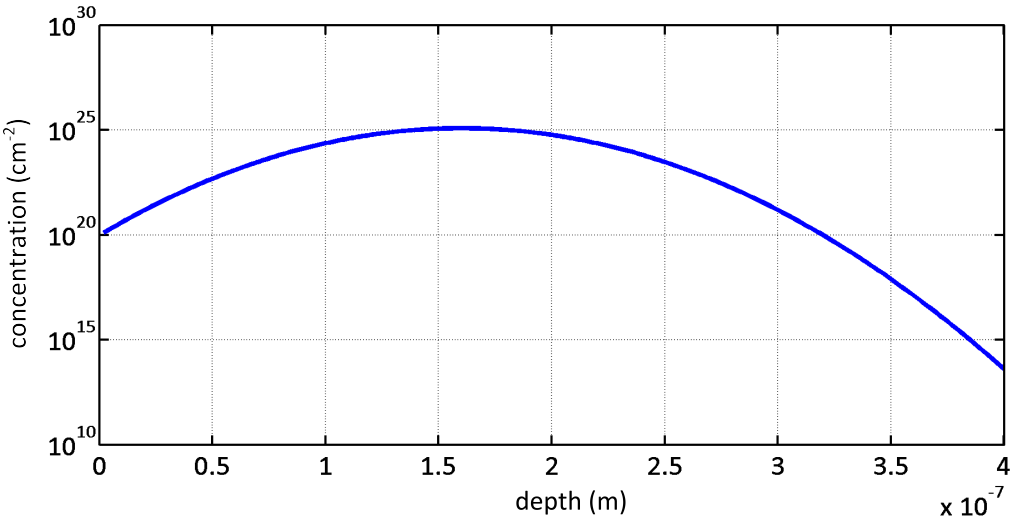

Fig. 5.7 The spin ensemble concentration profiles of ^{160}Gd in Al_2O_3 for the implantation parameters specified in the text.

5.2.3 Calculation of the collective coupling

An effective coupling rate may be calculated by integrating the spin density and magnetic field distribution within the volume of interest (V_{spins}):

$$g_{eff} = \sqrt{\int_{V_{spins}} \rho(v_{spin}) H(v_{spin}) dV}. \tag{5.6}$$

The total collective coupling rate is then determined by multiplying this effective coupling rate by the square root of the number of spins, and the single spin coupling rate,

$$\Gamma_{coll} = \Gamma_N g_{eff} \sqrt{N_{spins}}. \tag{5.7}$$

where $\Gamma_N = \mu_b \sqrt{\mu_0 \omega_r / (2\hbar V_{mode})}$.

Additional considerations

Further adjustments can be made to Eq. 5.7 to account for the effects of thermally excited spins. At finite temperatures, a fraction of the available spins will be thermally excited and will not contribute to the overall coupling rate. The number of thermally excited spins N_{ex} is dependent on both the temperature and the Zeeman splitting field, as derived from the Fermi-distribution (Section 4.2.3),

$$N_{ex} = N_{spins} \sqrt{\tanh \frac{g \mu_b H}{2 k_B T}}. \tag{5.8}$$

The resulting thermal factor, $T_f = N_{ex}/N_{spins}$ may then be included as a factor in Eq. 5.7. Additionally, the solution must be scaled up from two current carrying wires, to represent a lumped element geometry by a factor, $N_m - 1$, where N_m is the number of meanders,

$$\Gamma_{coll} = \Gamma_N g_{eff} T_f (N_m - 1) \sqrt{N_{spins}}. \tag{5.9}$$

5.2.4 Calculation results

By evaluating Eq. 5.9 with respect to the relevant experimental parameters, it is possible to estimate: the number of spins in the implanted volume, N_{spins}, the percentage of polarisation of spins, T_f, the number of maximally coupled spins, $N_{max} = \Gamma_{coll}/\Gamma_N$ and the total collective coupling rate, Γ_{coll} (MHz). The experimental parameters required to extract meaningful calculations include:

The experimental temperature:

This is expected to range from $T = 20 - 250$ mK, depending on the experiment.

The Zeeman splitting field:

This is estimated based on the ESR simulations in Section 5.1, and ranges from approximately $40 - 150$ mT. Transitions greater than 150 mT may not be accessible due to excess flux jumping within the superconductor.

The spin ensemble implantation area:

We assume this to be of length $z \approx 200$ um, which is around the length of a typical lumped element superconducting resonator design.

The implantation parameters:

These are discussed further in Section 6.3.2 and are specified as: dose $d_i = 10^{14}$ cm^2, $R_p = 160$ nm and $\gamma = 33$ nm,

The resonator centre frequency:

This typically ranges between $2 - 8$ GHz. A standard device used in our designs is assumed, where $\omega_0/2\pi = 3.35$ GHz.

The superconductor inductance $L = Z/\mu_0$.

Previous devices utilising a NbN superconductor of thickness 140 nm have an impedance $Z = 33\ \Omega$.

In evaluating our model with respect to these experimental settings, we are able to extract the various parameters including Γ_{coll}. An example of these results is shown in Table 5.1.

T (mK)	H (mT)	N_{spins}	N_{max}	T_f (%)	Γ_{coll} (MHz)
20	45	4.82×10^{11}	1.31×10^{11}	95.2	4.45
20	150	4.72×10^{11}	6×10^{10}	99.9	5.69

Table 5.1 Detailing the model parameters and the collective coupling rates of an implanted spin ensemble coupled to a lumped element resonator at 20 mK.

A discussion of the calculation results

From Table 5.1, the magnitude of Γ_{coll} looks promising in the context of producing a successful experiment since they are greater than typical values of resonator decay rates we have experienced ($\kappa \approx 0.5$ MHz). This tells us that the transitions should at least be visible to us. The values of Γ_{coll} are also greater than the expected spin ensemble line-widths. Provided our line-widths are of a similar order of magnitude, we should be operating in the strong coupling regime. Furthermore, the coupling rates correspond to a determinable number of spins. Since the implantation process is highly controllable, N_{spins} should be relatively accurate.

Chapter 6

Sample design, fabrication and preparation

Having demonstrated that we believe the system is capable of the desired operation, we next turn to the sample design, fabrication, and preparation. We first consider the sample designs we wish to produce, and the materials we wish to produce them with. To do this coherently, we first present an overview of the fabrication process and how this motivates the design layers which are required to produce an effective device design. We next turn to the device fabrication, first providing an overview of the facilities and the key micro-fabrication techniques used in this work. A fabrication procedure is then set out, the detailed recipes can be found in Appendix A. The final procedures to ready the device for the experiment are then listed.

6.1 An overview of the process

Here we present an overview of the overall procedure used to produce the device and work backwards to identify the required design layers. A schematic outline of this fabrication approach is shown in Fig. 6.1.

To begin with, alignment markers are deposited on the substrates, see Fig. 6.1 a). The markers are utilised throughout the fabrication process to ensure alignment between multiple nano-fabrication steps. A masked ion implantation technique is next employed, providing control of both the location and density of implanted spin ensembles. This is facilitated by the deposition of a hard nitride mask prior to the ion implantation. The mask is positioned in accordance

with the alignment markers and is patterned with the desired implantation design. The mask, therefore, acts as a stopping barrier where ions are not desired within the substrate, see Fig. 6.1 (b-c). The implanted mask is then removed and the substrate annealed, see Fig. 6.1 (d). The superconducting microresonator devices are next fabricated using standard lithography techniques, again utilising the alignment markers, see Fig. 6.1 (e-f).

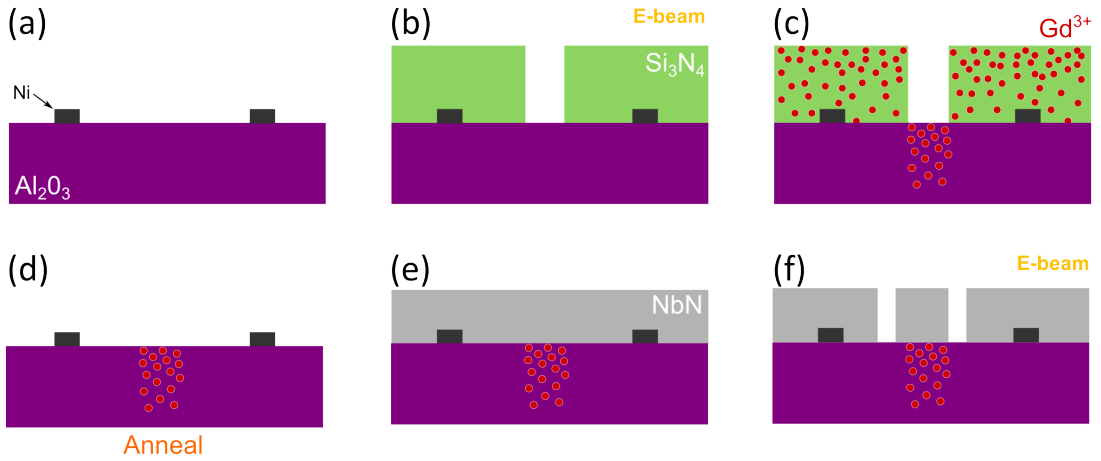

Fig. 6.1 An overview of the fabrication procedure: a) Alignment markers are first deposited on the substrate. b) A hard nitride mask is patterned on top of the substrate. c) Ions are then implanted. The mask stops unwanted ions reaching the substrate such that ions are preferentially implanted in lithographically defined regions. d) The mask is removed and the doped substrate is annealed. e) A superconducting thin film is deposited. f) The film is patterned with resonator devices ensuring alignment to pre-existing markers such that the resonator device lies directly over the implanted region.

From this overview, we can identify three key layers, which must integrate together seamlessly to produce successful and well-aligned devices. These layers include:

The alignment marker design used to ensure the careful alignment throughout the fabrication process.

The ion implantation mask layer deposited prior to any ion implantation process in order to reduce penetration of the ions during the implantation process within regions we do not wish to be exposed.

The superconducting microresonator layer used to pattern the microresonator devices after the ion implantation processing.

6.2 Design

The designs are developed using the software package 'Tanner - L-edit', where these independent layers may be incorporated in one common design. We consider the process and thoughts behind the design of each of these layers in Section 6.2.2. Before we can do this though, we must first establish the materials which are to be used in the fabrication of the samples, since the material properties will have a large effect on the designs.

6.2.1 Material choices

An r-cut sapphire substrate is used as previously extensively discussed in Section 3. The motivation for the use of this substrate lies in the history of the group, and the low-loss measurements which we have previously attributed to this substrate [40]. A NbN thin film is chosen as the superconductor of choice as motivated in Section 2.5.4. NbN is advantageous for operation of superconducting devices in magnetic fields, due to a higher thermodynamic critical field H_{c2} and large kinetic inductance. NbN resonators have been demonstrated to maintain high-quality factors in magnetic fields greater than 450 mT without a significant change in quality factors [81]. Additionally, the fabrication process for NbN deposition has been previously optimised by group member Sebastian de Graaf. This material is, therefore, an advantageous choice of superconductor for this project.

The alignment markers must survive many iterations of material deposition and removal, therefore must be resilient to these processes. Additionally, the material must be able to survive the high-temperature annealing process required after implantation. This leads us to use Nickel (Ni) for these preliminary investigations, with a melting point of 1455° C, the alignment markers should maintain shape during the anneal process which we estimate to require temperatures of up to 1400° C. We should be aware that Ni is a ferromagnet which will be placed within the

magnetic field, however, the distance of these alignment markers should be sufficiently far from the microresonator devices that they should be detected. However, we should keep an eye out within the experiment for any signal which may be attributed to this.

The ion implantation mask must be both thick enough in the deposition, and strong enough to withstand the bombardment of the ion implantation process. It must also be removable. It was recommended by the Surrey Ion Beam Centre (IBC) that for the desired ion-ensemble profile, a thick, low-stress Si_3N_4 mask would be required in order to provide a stopping barrier for the unwanted ions during the implantation process. It was calculated by the IBC that a mask of 400 nm thickness should be adequate.

6.2.2 Designs

Having established the materials used within the sample fabrication process, we now turn to the individual layer designs. We start with the alignment marker designs, where it is beneficial to have alignment markers in the shape of a cross for e-beam alignment and to include additional smaller features for finer alignment.

Next, turning to the SiN mask layer, we aim to include a number of different patterns within the designs, such that the samples include different areas of spin ensembles for exploration. These variations in implantation area include masked regions such that the spin ensemble may a) cover the entire inductive coupling area of the corresponding resonator b) cover only the inductive meander metallised strips and c) create spin ensembles of various widths and sizes. The incorporation of these varieties within the design allows for additional spin ensemble parameters for investigation in addition to the ion implantation dose and profile.

Finally, the resonator layer is created. This layer includes a variety of microresonator designs on each chip, which is designed to have centre frequency spread typically from $2 - 8$ GHz. The individual resonators are loosely modelled using the software package, 'Sonnet' to gain an idea of the centre frequency response of the design. This, however, is challenging due to the high kinetic inductance of NbN - which required an approximation of the frequency shift to be applied. Most individual resonator designs were adapted from previous designs in the group.

Examples of these design layers are shown in Figs. 6.2 to Fig. 6.5.

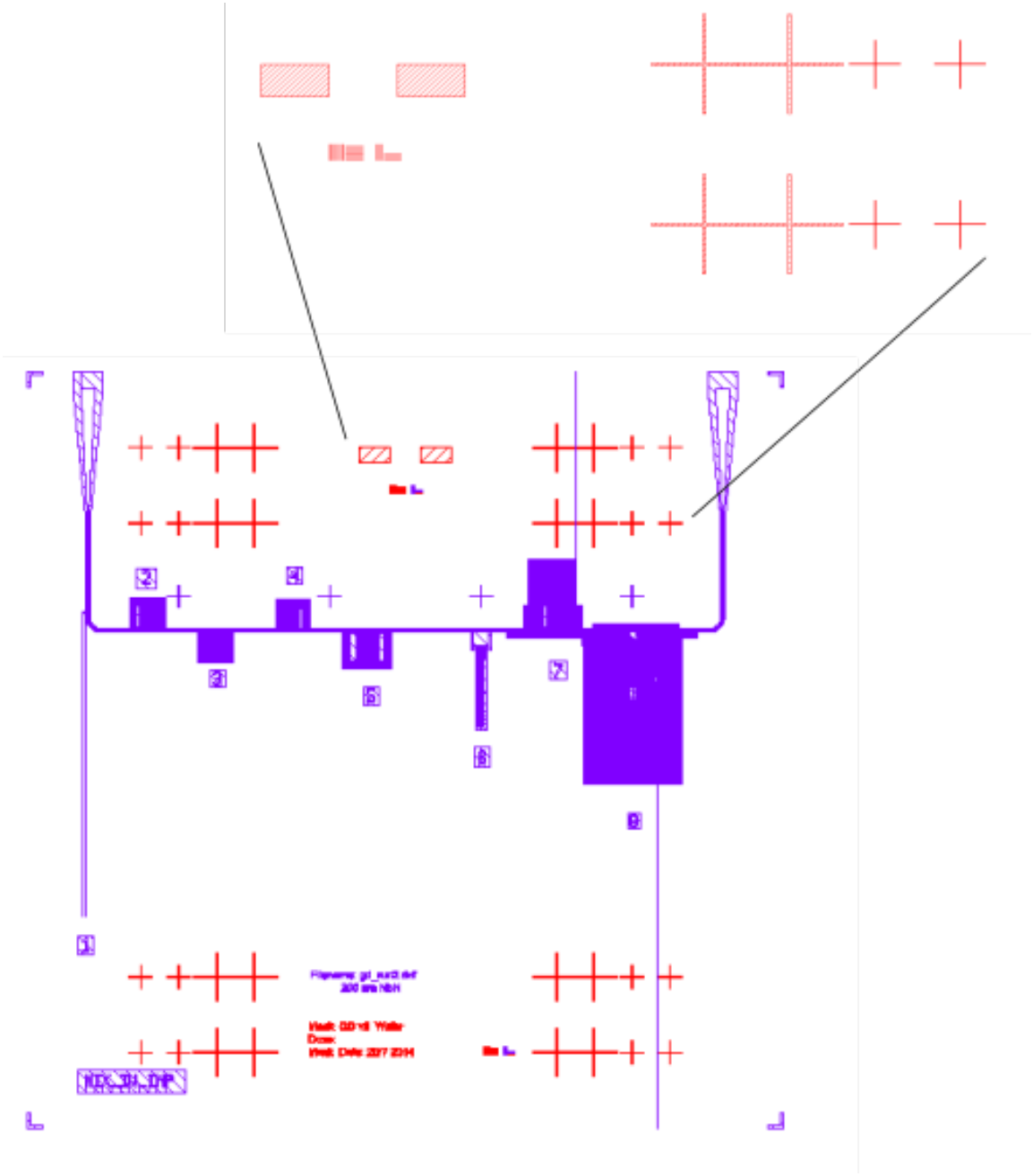

Fig. 6.2 Showing the resonator design layer (purple) and the alignment marker layer (red).

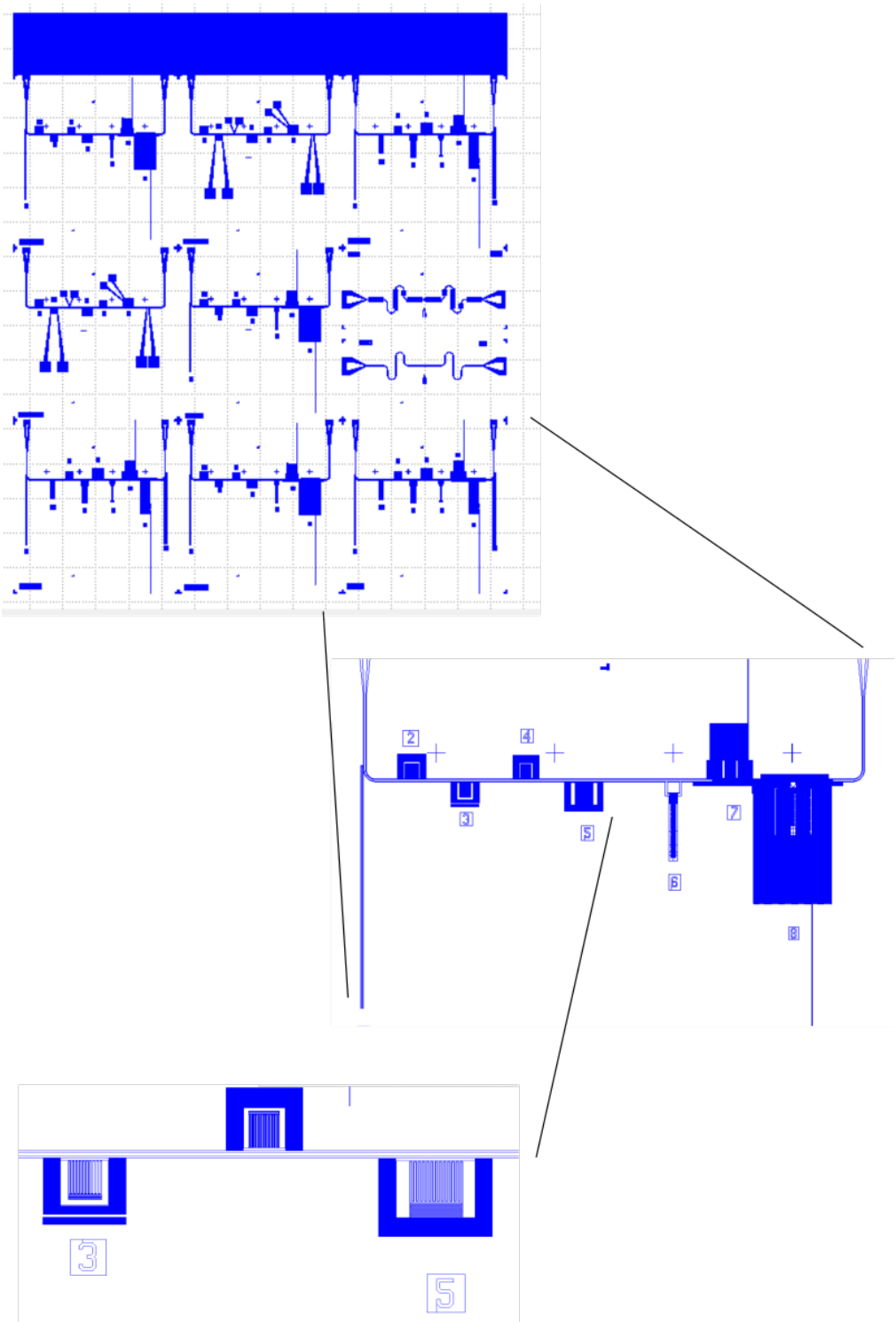

Fig. 6.3 Showing the resonator design layer full in the upper panel, with a focus on an individual chip and a series of lumped element devices on that chip in the lower panel.

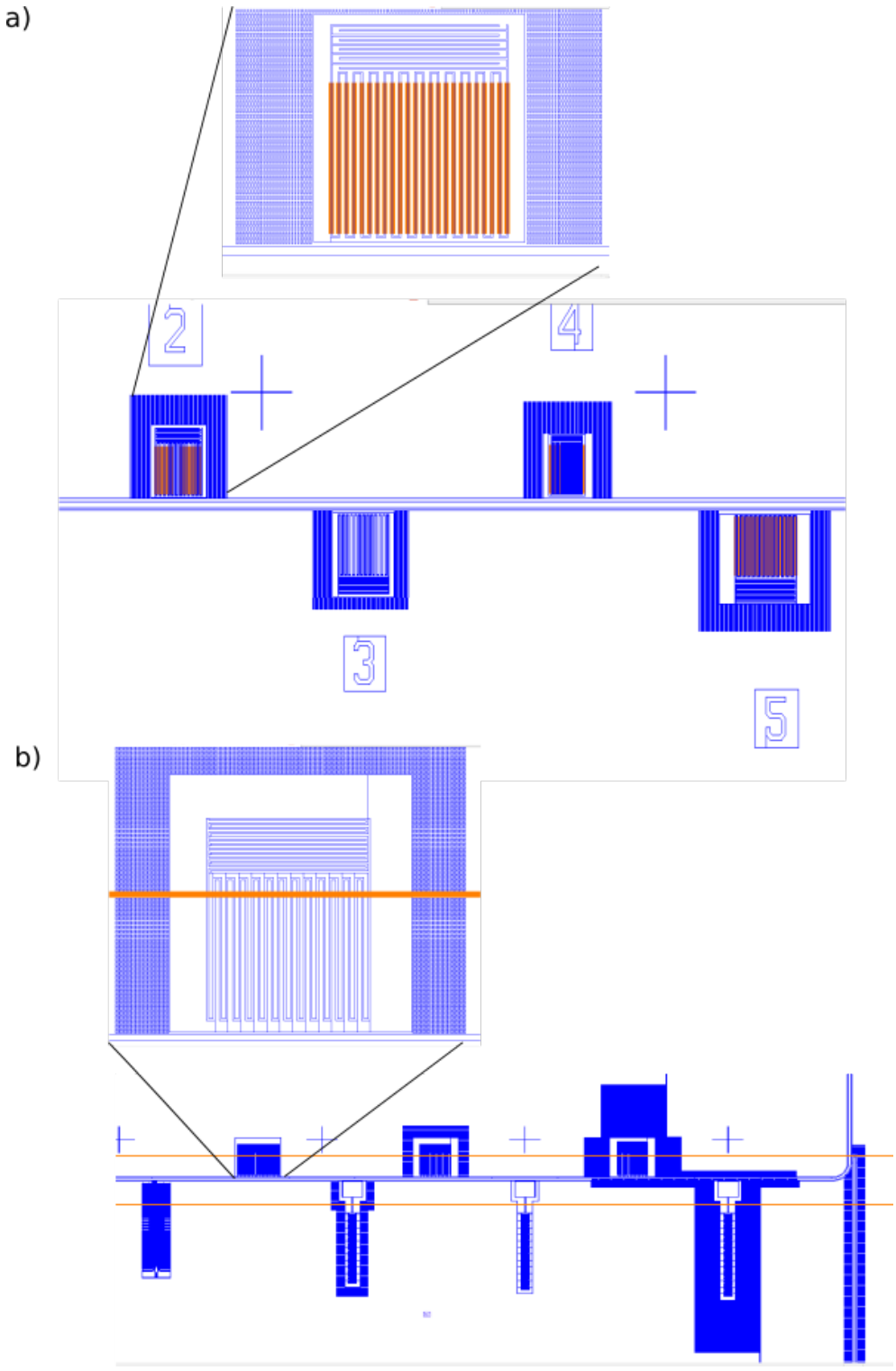

Fig. 6.4 Depicting two examples of the masked ion design (orange) with respect to the resonators (blue). a) The ions are designed to be implanted directly beneath the resonator inductive meander. In b) a small strip of ions are implanted beneath the resonator devices along the chip.

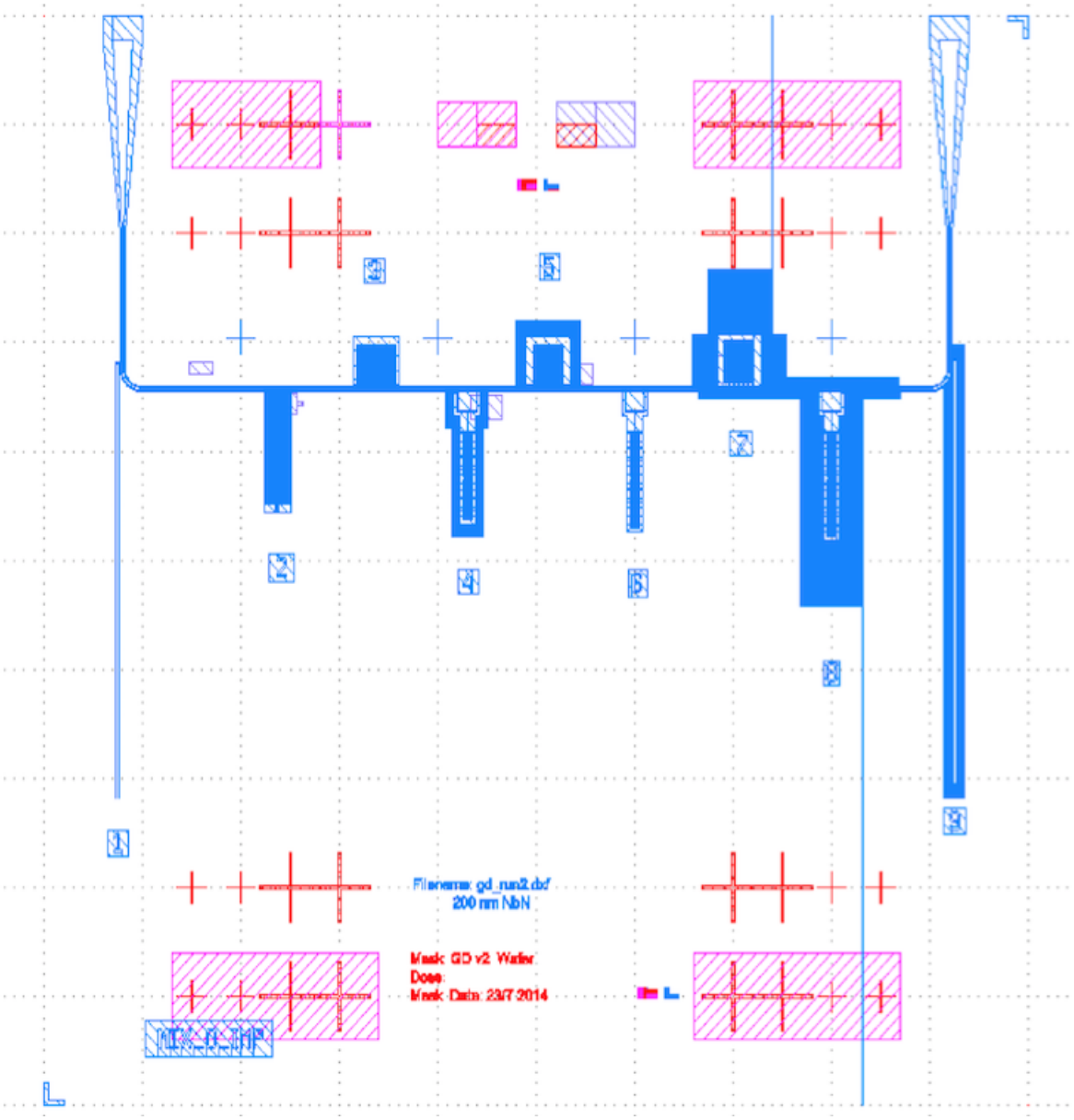

Fig. 6.5 An example of a full chip with all layers shown. In addition to the resonator layer (blue), the mask layer (purple) and the alignment layer (red), an additional layer (pink) is used to open up larger areas of the device.

6.3 Fabrication

To create the desired hybrid device requires the integration of a number of fabrication techniques. There is a particular challenge presented in the integration of a controlled ion implantation technique with micro-fabrication lithography without resulting detriment to the superconductivity. Some time is, therefore, spent describing the motivation behind the choice of certain techniques and steps within this process.

6.3.1 Clean room facilities

During the course of this project, two fabrication runs were undertaken. The first as a trial run to obtain samples for proof of principle experiments and the second with the aim of design and fabrication refinement.

Fundamental fabrication skills were learnt at the clean room facility at Royal Holloway, University of London. All of the fabrication processes described within this Chapter were carried out, where possible, by myself under the supervision of Sebastian de Graaf at the clean room facilities at MC2, Chalmers University of Technology. The ion implantation process was performed at the Ion Beam Centre (IBC), Surrey.

6.3.2 Fabrication techniques

The multi-step fabrication procedure incorporates a number of techniques uniquely suited to the specific requirements of these devices. Here, we provide an overview of the principles behind these techniques. More in-depth information can be found in Ref. [82].

Pattern generation

Pattern generation techniques such as photolithography (PL) or electron beam lithography (EBL) are used in micro-fabrication to transfer designs on either thin films or substrates. Both PL and EBL are utilised in the fabrication of these devices. In both techniques, a photosensitive

film (photoresist) is exposed with the desired design to generate patterns. The resist is then developed to leave the substrate exposed in the desired regions. Then, depending on the polarity of the resist, the material underneath may be etched, or a new material deposited on the substrate.

Photo-resists

Photo-resists comprise a base resin, a photoactive compound and a solvent. The resin determines the mechanical and thermal properties of the resist, the photo-active compound is responsible for radiation sensitivity and the solvent controls viscosity. The photo-resist may be either 'positive' or 'negative', such that the base resin reacts either to form an acidic soluble compound or cross-linked and insoluble polymer respectively, as such determining the 'polarity' of the transferred pattern.

Photoresist films are created using a standard spin coating application method, where the film thickness is dependent on resist viscosity and spin speed. The film is then baked to remove any remaining solvent, where the bake temperature is controlled so as not to be detrimental to the photo-active compound.

Photolithography

Photolithography (PL) employs the use of light to transfer a geometric pattern from a photomask to the photoresist. The photo-mask is prefabricated (usually by EBL) and comprises a quartz plate with chromium patterning. The mask is brought into contact with the resist-covered sample and is exposed for a number of seconds with ultraviolet radiation, typically from a mercury lamp.

In the fabrication of devices in this work, PL is well suited for creating the hard nitride mask detailed in Fig. 6.1 b). This is because PL is a fast process ideal for large-scale exposures. The drawback of PL is its limitation in resolution, typically down to ≈ 200 nm.

Electron-beam lithography

The microresonator devices to be patterned in this work are made from a NbN thin film. High-

quality NbN microresonator devices are very sensitive to any changes in width and uniformity and therefore require very high accuracy patterning. Because of this, it is advantageous to use an electron-beam lithography (EBL) system - which employs the use of a focused stream of electrons in a raster-like process to directly write the desired pattern into the photoresist when creating these devices.

An EBL system consists of an electron gun, a collimator, magnetic lenses, shutter and deflecting coils. The electron gun extracts a stream of electrons from a filament which is accelerated by an electric field. The stream is focused by the collimator and magnetic lenses into position over the surface of the resist-covered sample using the deflecting coils. By this method, patterns are directly written from CAD files without the need of a photo-mask.

The JEOL JBX-9300FS system available at the MC2 facility has a 4 nm diameter Gaussian spot electron beam and is capable of producing features of the order a few nanometres across. This, along with a highly precise alignment stage and automated marker detection system makes EBL extremely successful in creating our detailed microresonator devices and providing good alignment to the spin ensembles beneath.

Development

Both photolithography and EBL photoresists require a post-exposure bake, promoting the diffusion of photo-generated molecules, changing the resist solubility before development. During development, the photo-resist is submerged in a suitable photoresist developer for a given amount of time, such that the soluble areas of resist are removed. Over or under-development, and under or overexposure may result in adverse effects to the desired patterning and are to be avoided. Rinsing and drying complete the development stage.

Lift off

Performing a lift-off procedure involves the metallization of an exposed area of photo-resist and is depicted in Fig. 6.6 a). It is of note that an additional sacrificial photoresist layer is here used to perform lift-off, to assist in creating an undercut during exposure. After lithography, metal deposition is performed, followed by resist dissolution in solvent and lift-off - removing all

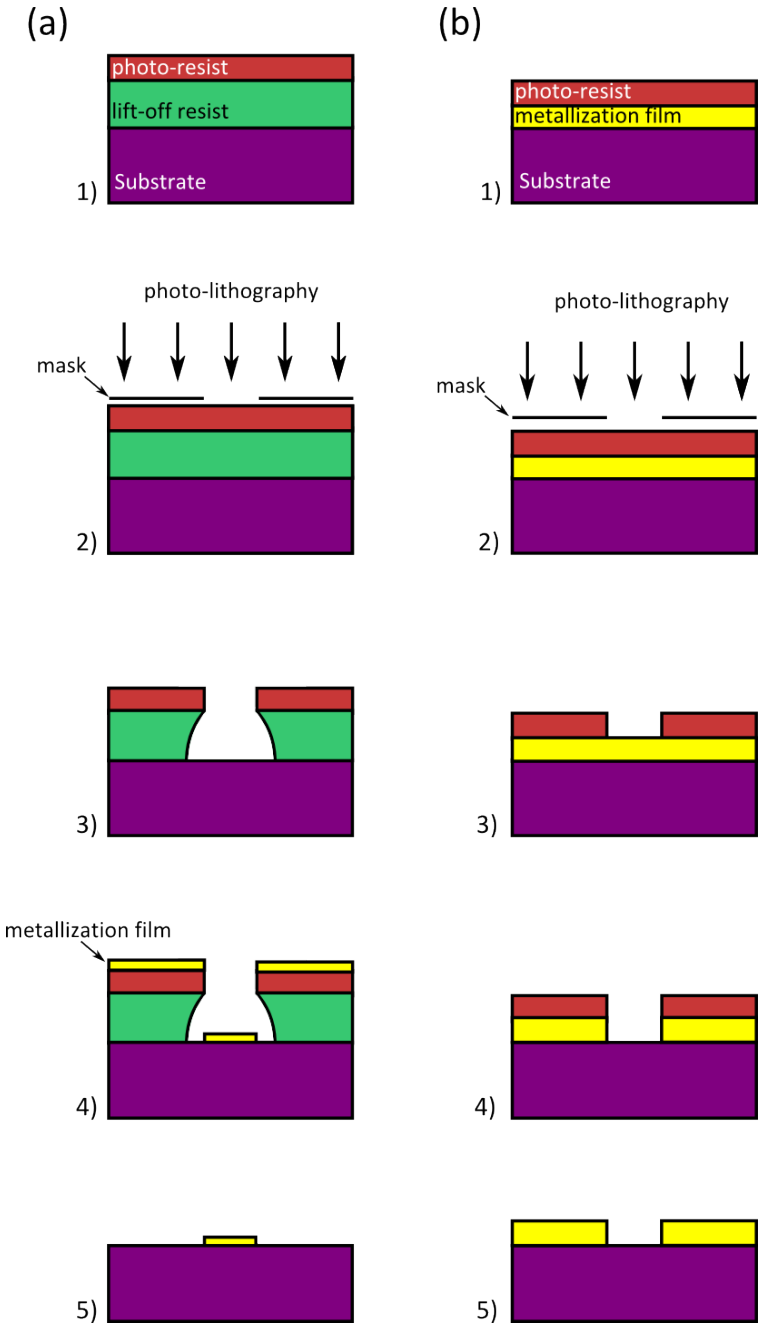

Fig. 6.6 a) Schematic of a lift-off process: 1) lift-off resist and photoresist are spun on top of the substrate. 2) Photo-lithography patterns the resist 3) and is developed with an undercut. 4) metal is deposited on the surface of the substrate. 5) The sample is placed in developer, leaving the metallised patterned film. b) Schematic of an etching process: 1) The sample is covered with a thin metal film and photoresist. 2) Photo-lithography patterns the resist. 3) The resist is developed. 4) The exposed metallized film is removed by an etching process. 5) The residual resist is removed.

metal not in direct contact with the substrate. The undercut is integral to the process, allowing the solvent access to the photo-resist despite the metallization. The lift-off technique is used in this work to create the initial Ni alignment markers.

Etching

Etching involves an engraving of the exposed pattern on the material underneath the photoresist, as depicted in Fig. 6.6 b). There are many different types of etching techniques, outlined here are those utilised in this fabrication process:

Reactive ion etch

Reactive ion etching (RIE), uses a chemically reactive plasma to etch films on substrates by both chemical and physical processes. The plasma is generated by applying an RF electromagnetic field (typically 13.56 MHz) to an electrically isolated wafer platter in a low-pressure environment. The electric field ionises a reactive gas species, creating a plasma which is accelerated by the field and collides with the sample. Etching occurs primarily chemically, but also etches physically due to the high kinetic energy of the ions on impact. Typically, RIE creates anisotropic etch profiles due to the largely vertical etch process. The RIE process can be tuned by control of pressure, gas flow and RF power. RIE is used in the creation of both the SiN ion implantation mask layer and the NbN microresonator devices.

Wet etch

A wet etch requires immersion of the desired material to be etched in a temperature regulated chemical bath. This results in a purely chemical etch process. Whilst a simple process in terms of equipment and processing, chemical and disposal costs are high. Chemical etching typically results in an isotropic etch profile, which can result in unwanted undercutting and problems in etching small geometries. The use of warm chemicals can also lead to poor photoresist adhesion. Despite this, a chemical wet etch is required in this process for successful removal of the hard nitride mask and implanted contaminants [83]. The RIE process is not suitable for this purpose

as the etch process works faster on the nitride mask than the impurities and would leave a residual layer of unwanted ions on top of the substrate.

Thin film deposition: sputtering

Magnetron Sputtering is a Plasma Vapor Deposition (PVD) process in which a plasma is created and positively charged ions from the plasma are accelerated by an electrical field superimposed on the negatively charged electrode or "target". The positive ions are accelerated by an potential ranging from a few hundred to a few thousand electron volts and strike the negative electrode with sufficient force to dislodge and eject atoms from the target. These atoms will be ejected the target and will condense on surfaces that are placed in proximity to the magnetron sputtering cathode. In a typical sputtering system, a gas moderator within the chamber slows the ejected ions such that transport between the target and substrate is diffusive. This moderator is often argon, but krypton and xenon are also commonly used. By control of the moderator pressure, a range of transfer energy is accessible, controlling sputter rates. Typical sputter rates range from $1 - 10$ nm/s.

The targets are fabricated from materials that one wishes to deposit on the surface of the component facing the electrode. Conductive materials can be deposited using a direct current (DC) power supply and insulators can be deposited by using a radio frequency (RF) power supply. In the case of this work, a Nb target is used alongside a 60 sscm of Ar and 6.5 sccm N2 at a pressure of 12 μbar is used to deposit a 200 nm NbN thin film on the sapphire substrate.

Ion implantation

Ion implantation is a process whereby accelerated ions hit a target with such energy that they penetrate the surface and slow to rest by collisional and stochastic processes within a number of femtoseconds. Dopant concentration profiles are highly controllable, where implantation depth and dopant density are tuned through implantation energy and dosage respectively. Ion implantation disrupts and damages the crystal, therefore it is standard practice that

implantation is followed with a high temperature anneal step to recover a defect-free crystalline environment.

Photo-resists substantially thicker than the projected implantation range can be deposited on top of the substrate pre-implantation to mask the ion implantation in given areas, providing lateral controllability. This masked technique is useful in the fabrication of devices in this work, where accurate control and knowledge of the spin system is highly desirable.

In this work, ion implantation is performed using a 2MV Van der Graaff heavy ion accelerator at the IBC, Surrey. A schematic of an ion implanter is shown in Fig. 6.7 and consists of an ion source whereby ions are generated in plasma discharges. Ions are extracted from the source by an extraction potential and enter into a selection magnet. The selection magnet operates by spectrometric separation according to the radius of curvature in a magnetic field providing the centripetal force. Adjustment of the magnetic field, therefore, allows the required ion mass and velocity to be selected. Within the selected ions, there is a spread of kinetic energies and consequently a spread in the depth profile within the target substrate.

The desired ions are resolved by a selectable resolving aperture and further ion optics and are then accelerated in high vacuum through an acceleration column toward the target substrate. The implantation dose is monitored by a Faraday cup beam monitor measurement.

Post-implantation, the wafer is charged. This is compensated by electron-flooding: an electron gun generates the electrons used to neutralise the wafer; care must be taken not to overcompensate which may result in negative charging.

During implantation, the ions scatter stochastically, with each scattering event resulting in a deceleration of the ion by nuclear and electronic stopping, as depicted in Fig. 6.8 a). Each ion will therefore individually travel for a total distance, R, whilst the peak implantation depth, R_p is determined by the initial implantation energy. The stochastic process results in a lateral dispersion R_L from the incident direction, which ultimately limits the lateral resolution in masked implantation to ≈ 10 nm.

The spread of initial ion kinetic energies results in a depth profile within the target substrate with a dispersion from R_p of ΔR as shown in Fig. 6.8 b). Typically, ΔR is 10% of R_p.

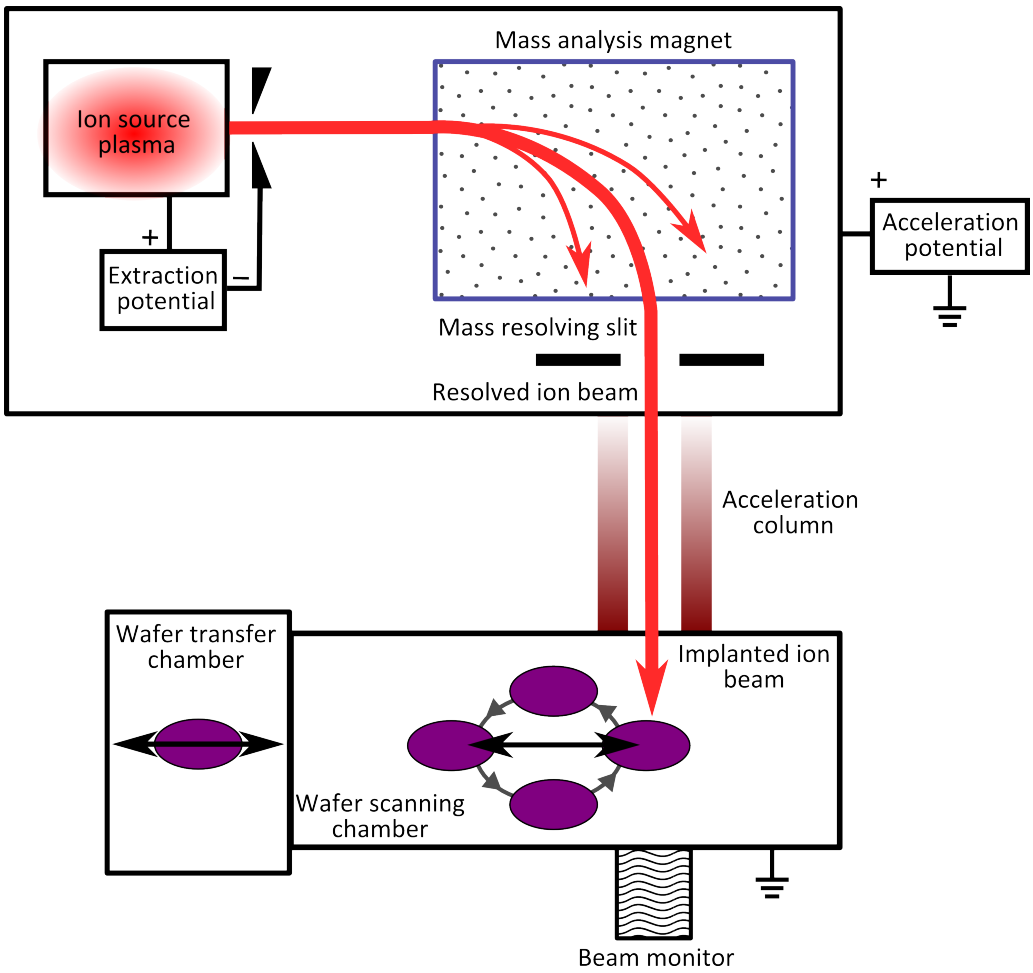

Fig. 6.7 A schematic of an ion implanter. An ion source plasma is generated and the ions are extracted by an applied potential. The ions are accelerated through a selection magnet to resolve the desired ions. The resolved ion beam passes through an acceleration column under vacuum to the target substrate. The beam monitor measures dose throughout implantation. The system is set up such that many wafers may be implanted in one implantation run, with multiple wafer holders and a rotating plate system.

Typical ion implantation energies range from $10 - 200$ keV, with doses of 10^{11} to 10^{16} ions/cm^2. Since implantation depths are typically on the order of a few hundred nanometres, the resulting concentrations are usually between $10^{15} - 10^{20}$ cm^{-3}.

Penetration depths can be simply approximated through calculation of nuclear and electronic energy losses, but are more accurately found with Monte Carlo (MC) simulations. SRIM (Simulation of Ranges of Ions in Matter) is a commonly used MC simulator and is used in this work at the IBC to predict concentration profiles.

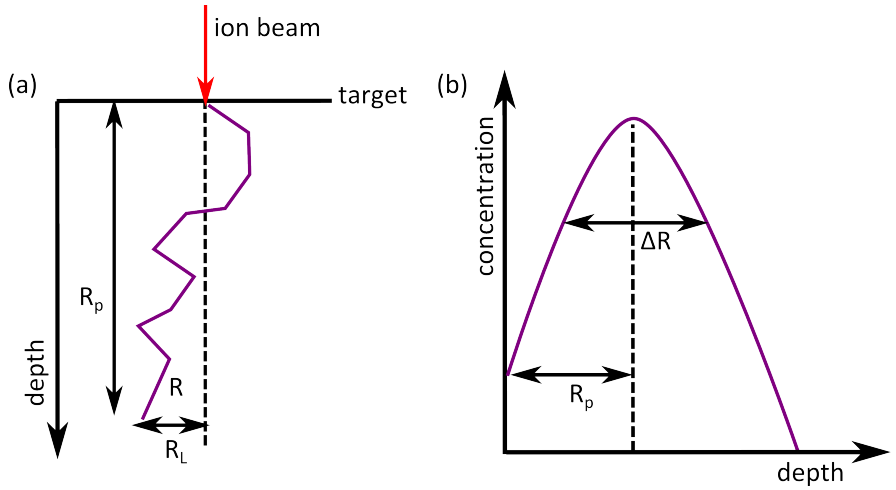

Fig. 6.8 a) Ions scatter stochastically to R_p, travelling an overall distance R. This results in lateral dispersion R_L from initial implantation angle of incidence. b) An example ion implantation concentration profile. Peak implantation depth R_p is determined by implantation energy. The spread of initial ion energies, results in a depth profile within the target substrate with a dispersion from R_p of $\pm\frac{\Delta R}{2}$.

Ion implantation can cause extensive damage to the target substrate crystalline environment. The level of damage depends on the implant species, energy, dose and current. The higher the energy, heavier the ion, and greater the implantation dose - the higher the damage. Damage can take the form of point defects, such as vacancies and interstitials, as well as extended defects such as dislocation loops.

An annealing process assists in repairing lattice damage as well as in activation of the dopant atoms; providing energy to assist movement of dopants into the appropriate interstitial lattice

sites. If the concentration of dopant ions is too high, activation will not be possible since the site availability is saturated.

In this work, the implanted Al_2O_3 wafers are annealed at 980° C for 1 hour, before cooling during approximately 4 hours. This annealing temperature was chosen based on previous literature [84, 85].

The implantation parameters used for ion implantation are detailed in Table 6.1. Prior to implantation, SRIM was used to simulate concentration profiles which are shown in Fig. 6.9.

During the first fabrication run, see Table. 6.1(Run1), 5 wafers were implanted both with and without a hard nitride mask (plain1: p1 and masked:m1 respectively). The implantation doses were also varied across 3 orders of magnitude for preliminary exploration.

The second fabrication run, see Table. 6.1(Run2), sought to optimise alignment. Implantation was performed on 4 substrates with a focus on the variation of dopant profiles and spin ensemble geometries. Additionally, manipulation of implantation profiles using a multi-depth profile implantation process (multi-masked: mm2) was explored.

Run	Wafer	Dose (ions/cm^2)	Energy (keV)
1	$p1_{14}$	10^{14}	1600
1	$p1_{15}$	10^{15}	1600
1	$m1_{13}$	10^{13}	900
1	$m1_{14}$	10^{14}	900
1	$m1_{15}$	10^{15}	900
2	$m2_{5e13}$	5×10^{13}	1100
2	$m2_{14}$	10^{14}	1100
2	$mm2_{1.25e13}$	1.1×10^{13}, 0.49×10^{13}, 0.41×10^{13}	1400, 1000, 700
2	$mm2_{1.5e13}$	5.48×10^{13}, 2.46×10^{13}, 2.05×10^{13}	1400, 1000, 700

Table 6.1 Details of implantation parameters used to implant ^{160}Gd in Al_2O_3. Two implantation runs are performed and are either: implanted with no mask - plain (p), masked (m) or have multiple implantation profiles and are masked (mm). Doses are varied by 3 orders of magnitude and energies are varied depending on the use of mask and the desired peak implantation depth. Resulting profiles are depicted in Fig. 6.9.

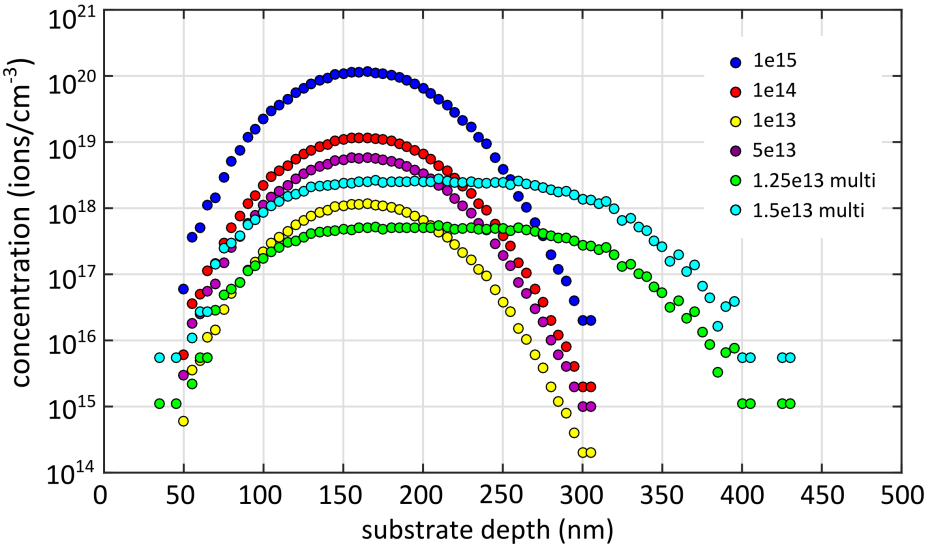

Fig. 6.9 The calculated spin ensemble concentration profiles of ^{160}Gd in Al_2O_3 for the implantation parameters specified in Table. 6.1. The profiles are simulated using SRIM.

6.3.3 Device fabrication

Wafer preparation

All samples used for this project are fabricated using commercially available r-cut $(1\bar{1}02)$ sapphire (Al_2O_3) 2 inch wafers. This substrate was chosen due to its low dielectric loss [40].

Alignment markers

In order to ensure maximal coupling between the implanted spin ensemble and resonator devices, careful alignment must be achieved during the fabrication process. Initial deposition of alignment markers is, therefore, crucial to the success of device fabrication. For this reason, both large crosses and small arrays of lines are used as markers for accurate alignment, see Fig. 6.10 b). Additional consideration is given to the required material properties of the markers; with the need to withstand high annealing temperatures (up to $\approx 1000^\circ$ C). For this reason, Nickel (Ni), with a melting point of 1455°C was chosen as a suitable marker material.

The Ni markers are deposited using a tri-layer resist lift-off mask. The mask is comprised

of 570 nm of photoresist composite 'mmA8.5mAAEL10' and 70 nm of photoresist composite 'Sx Ar-P'. A final thin layer of e-spacer 300-ax01 is spun on top in order to mediate e-beam lithography processing on the insulating substrate. The e-spacer is conductive and stops negative charge build up which can otherwise cause beam deflection, and thus pattern distortion.

A JEOL JBX-9300FS lithography system is used to expose the alignment marker pattern. The e-spacer mask is next removed with H_2O for 30 s. The mask top layer is developed in O-Xylene, and bottom in H_2O:IPA mix (7 : 93). 80 nm of Ni is next evaporated, followed by an acetone lift off. The wafer finally undergoes a short oxygen plasma ashing to remove any residual photoresist. Optical microscope images of the resulting Ni alignment markers are shown in Fig. 6.10.

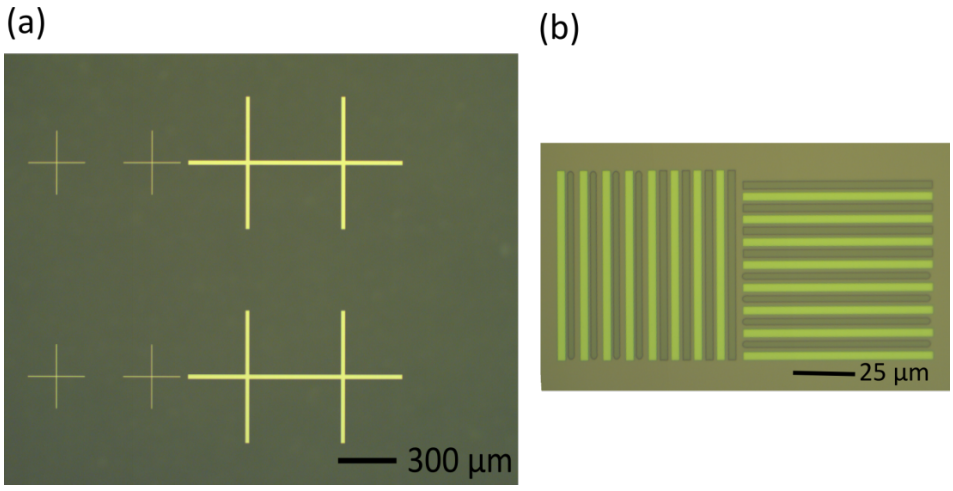

Fig. 6.10 Optical images of the resulting Ni alignment markers a) Large crosses (Ni only) b) Ni markers with SiN mask (light stripes) lines in between original Ni pattern.

SiN implantation mask

For the desired ion-ensemble profile, high energy (> 900 keV) ion implantation is used. Therefore, in order to create local spin ensembles a thick, low-stress Si_3N_4 mask is required in order to provide a stopping barrier for the unwanted ions during the implantation process. To create the mask, Si_3N_4 at a thickness of 400 nm is first deposited. The required thickness is calculated such that it is sure to overcome the stopping energy of the ions during implantation.

The mask is deposited using multi-frequency plasma enhanced chemical vapour deposition (MFSIN(PECVD)), a process which uses a SiH_4 and N_3 gas in an RF plasma and switches between 1 and 13.56 MHz. The two frequencies result in varying tensile stress of the film - which is here optimised for zero stress.

A 70 nm Al mask is then evaporated on top of this film as an etch mask. A further, thin PMMA(A4) resist layer is used to avoid losing lithography resolution since the implantation opening width is in places $< 1\mu$m. The mask is then patterned using photo-lithography by a 250 s deep ultraviolet (DUV) exposure, ensuring alignment to the Ni markers. It is then developed in a H_20:IPA mix $(7 : 93)$.

A reactive ion etch (RIE) is performed to etch the Al in chloride plasma and the SiN in CF_4 plasma. Finally, the Al is removed in a MF319 wet etch, concluding the hard nitride mask fabrication procedure.

Ion implantation

A Gd^{3+} ensemble of isotope ^{160}Gd with nuclear spin $I = 0$ and ground state $f^7S_{7/2}$ is next implanted using a 2MV Van der Graaff heavy ion accelerator manufactured by HVEE at the IBC, Surrey. The implantation is carried out at room temperature with a 7° tilt to the normal of the r-plane in order to limit ion channelling.

For each individual wafer, doses and implantation profiles are varied as previously detailed in Table 6.1. The instantaneous beam current is limited to 1 μA to prevent sample heating with the beam scanned at 1 kHz frequency in the x and y directions over a 5 cm $\times$ 5 cm area to provide a uniform irradiation at $\pm 1\%$.

It is interesting to observe that after implantation, varying degrees of damage to the contaminated mask at different concentrations is visible by an optical microscope as shown in Fig. 6.11, however, ultimately this is not important to the process as the damaged mask is next removed.

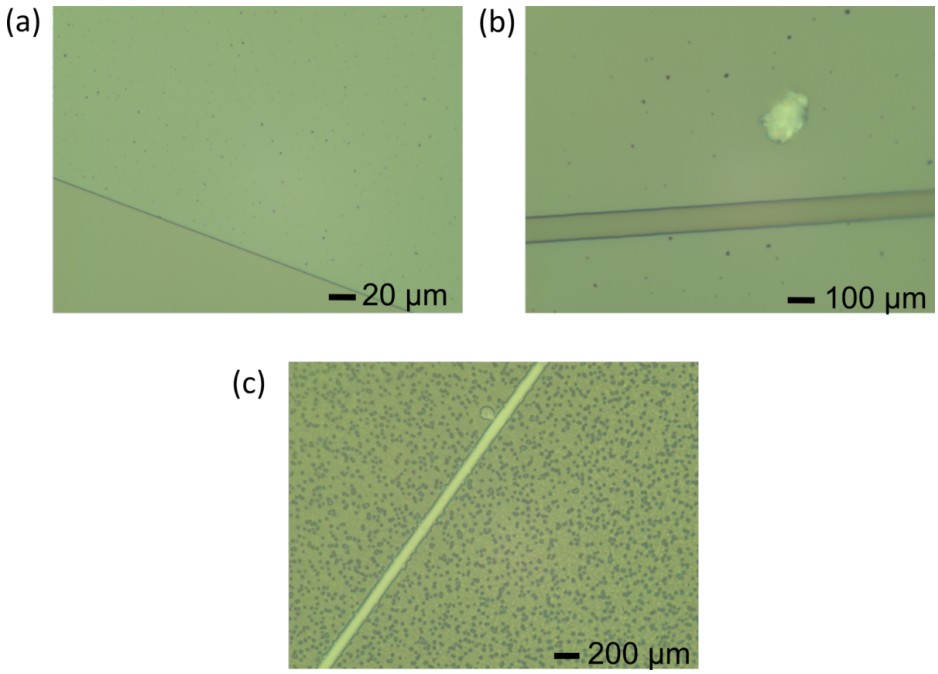

Fig. 6.11 Optical micrographs showing the varying degrees of damage to the SiN mask due to implantation, dependant on dose. a) aW1: dose 1e13 b) aW2: dose 1e14 c) aW3: dose 1e15. Damage to the mask is not important to the overall process since the mask is removed.

Post-implantation processing

The implanted SiN mask is then removed using a buffered oxide etch (BOE) HF bath for a duration of 10 minutes. Such a time period is found to be adequate in fully removing the SiN mask without damaging the Ni markers, see Fig. 6.12 a,b).

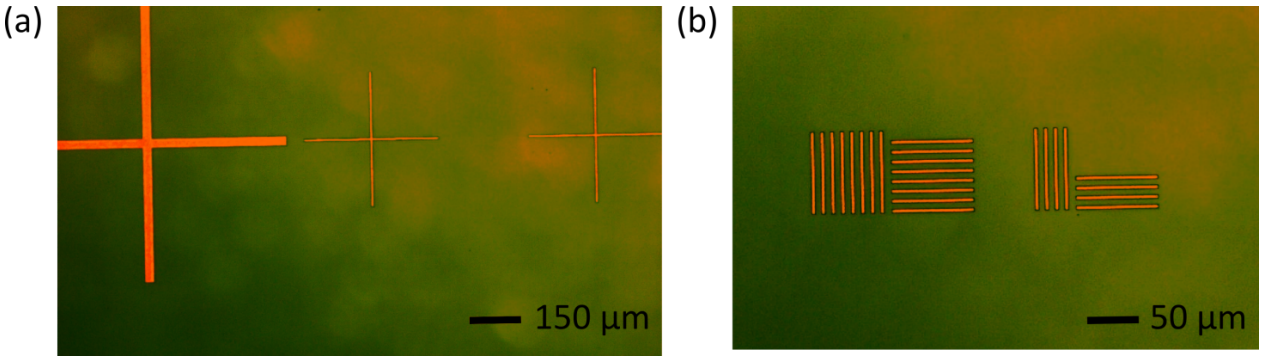

Fig. 6.12 Optical images of wafers after the implanted SiN mask is removed. The Ni markers remain intact and little residue remains on the surface. The red tinge is from polarisation filters used when obtaining the optical image. a) large Ni cross features b) small lined Ni features.

The wafer is then annealed by ramping the temperature at a ramp rate of 10° C/min and is held at 980° C for 1 hour before it is cooled during approximately 4 hours. Post-anneal, the RMS surface roughness is found using AFM to be ±4 nm RMS, comparable to typical values of pristine sapphire wafers.

Resonator fabrication

A 200 nm NbN sputtered thin film is next deposited using a near-UHV DC magnetron sputter system. Whilst good thin film quality is generally achieved, see Fig. 6.13 a), it is found that film quality may be compromised if residual SiN remained on the wafer, see Fig. 6.13 b). In the latter case, the NbN is removed via plasma etch, and NbN deposition procedure started again from the point of SiN removal with a further BOE.

A UV5 − 0.8 photoresist is spun on top of the thin film and is baked at 130° C on a hotplate for 120 s. The wafers are then loaded into the JEOL JBX-9300FS. The e-beam machine is

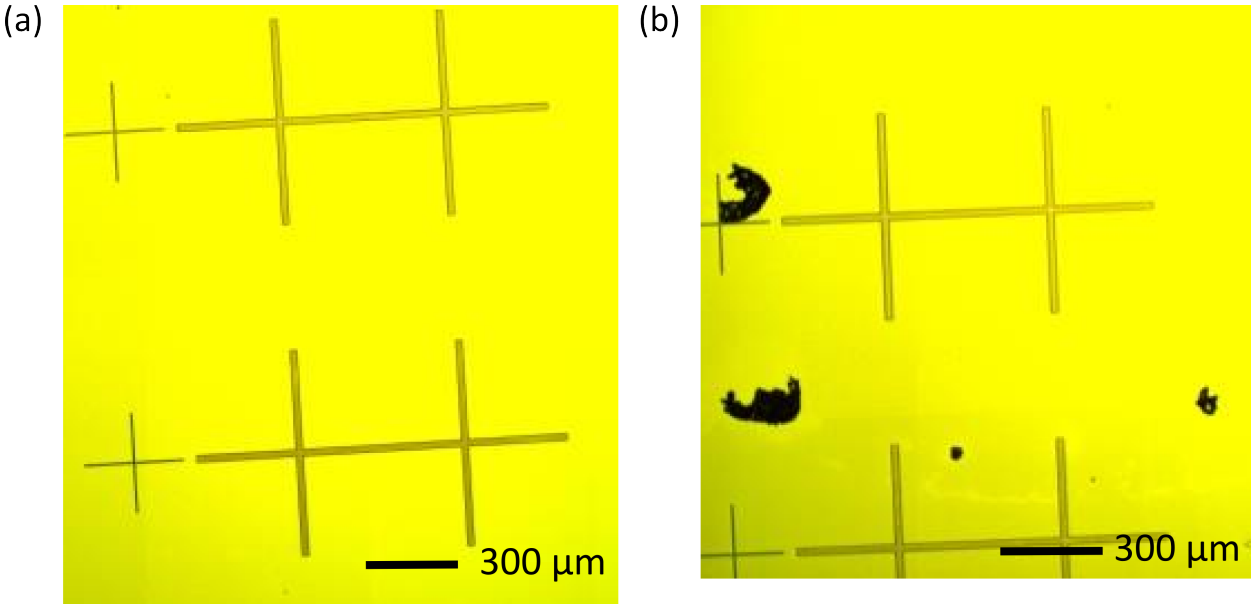

Fig. 6.13 Optical images of a) a good quality NbN sputtered thin film, b) a thin film which has been compromised by resist residue.

carefully calibrated in aperture, current, focus and astigmatism - utilising the Ni markers to ensure good alignment of the resonator pattern with the implanted regions. The e-beam write exposure is next performed using a 35 nA current, and a capacitance rate of 23 μC/cm^2 to pattern the mask with the microresonator devices. After exposure, the mask is baked for a further 90 s at 130° C and developed in MF-24A for 40 s, followed by a water rinse. The NbN is then etched in plasma using NF_3 gas, using a laser interferometer and end-point detection mechanism to over etch for a duration of 10 s, such that a total etching time for 200 nm of NbN is 90 s. The wafers are then cleaned from resist overnight and rinsed in IPA. If resist residues were present, a further O_2 ash process may be performed.
Details of this procedure can be found in Appendix. A. Examples of the resulting microresonator devices are shown in Fig. 6.14.

Final devices

An example of a completed wafer is shown in Fig. 6.15 a). The wafer is divided into individual 10 x 10 mm samples using a double-cut procedure on a diamond saw. An example of an

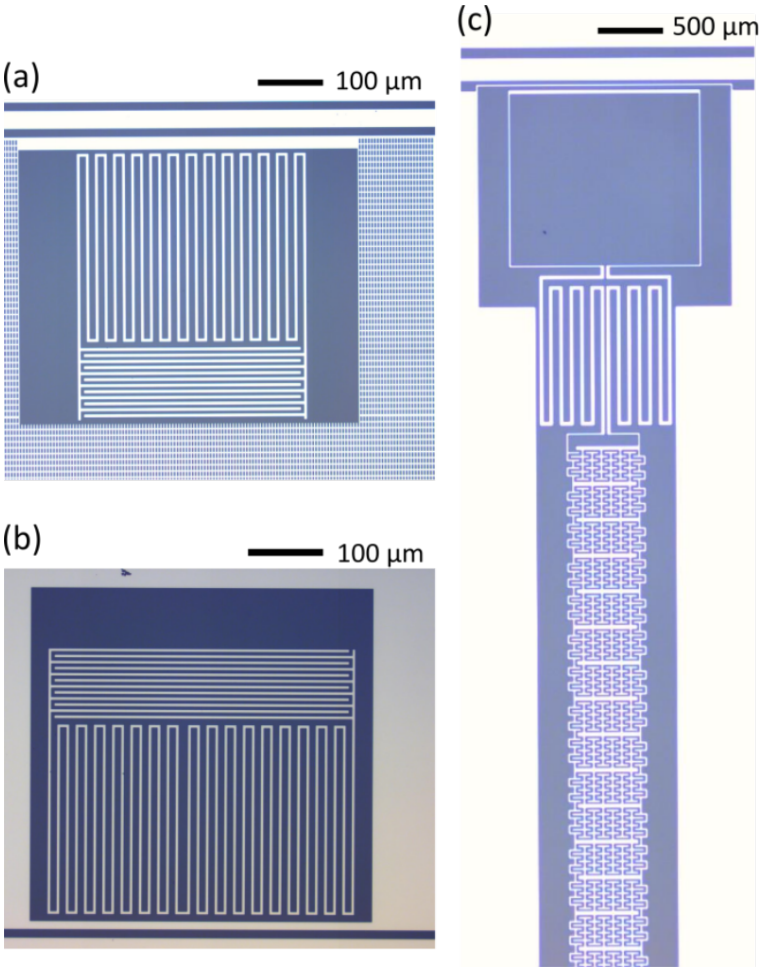

Fig. 6.14 Optical images showing examples of fabricated microresonator devices inductively coupled to the transmission line. a) A lumped element microresonator with a dotted ground plane. b) A standard lumped element microresonator device. c) A fractal microresonator device.

individual chip is shown in Fig. 6.15 b).

When inspecting an individual resonator during the first fabrication run, it was found that the implanted region can be discerned using an optical confocal microscope with polarisation filters, as shown in Fig. 6.16 a). From this, it was found that alignment during the first fabrication run was not optimal due to a mistake in CAD between layers, resulting in an offset between the areas of implantation and maximal coupling regions of the microresonator devices. During the second fabrication run, it was demonstrated that higher accuracy alignment can be achieved, as shown in Fig. 6.16 b). Here, the implanted regions are visible by scanning electron microscope (SEM) and can be observed perfectly aligned underneath individual inductor meander lines.

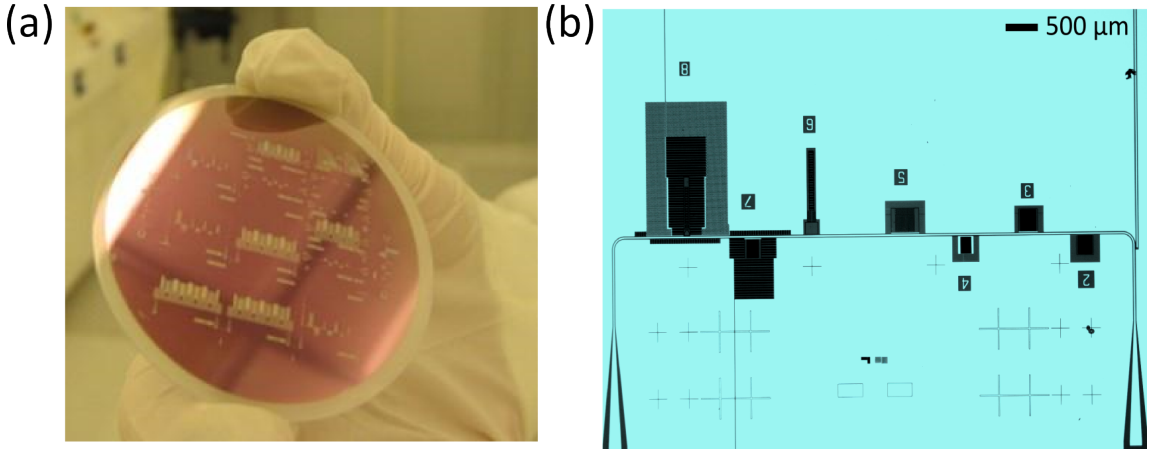

Fig. 6.15 Optical images of a) a completed wafer, comprising a 3 by 3 array of 10 x 10 mm samples of varying designs. b) An individual sample with 7 multiplexed resonators inductively coupled to the transmission line.

6.3.4 Final sample preparation

A typical 10x10 mm sample consists of a 50 Ω, 25 μm transmission line, surrounded by a ground plane within which 7 multiplexed microresonator devices sit, and are inductively coupled to the transmission line typically at distances of $10 - 30$ μm.

The sample and a printed circuit board (PCB) are mounted to a copper plate for both mechanical support and thermal contact. The PCB is metallised with gold and is patterned with a 50 Ω

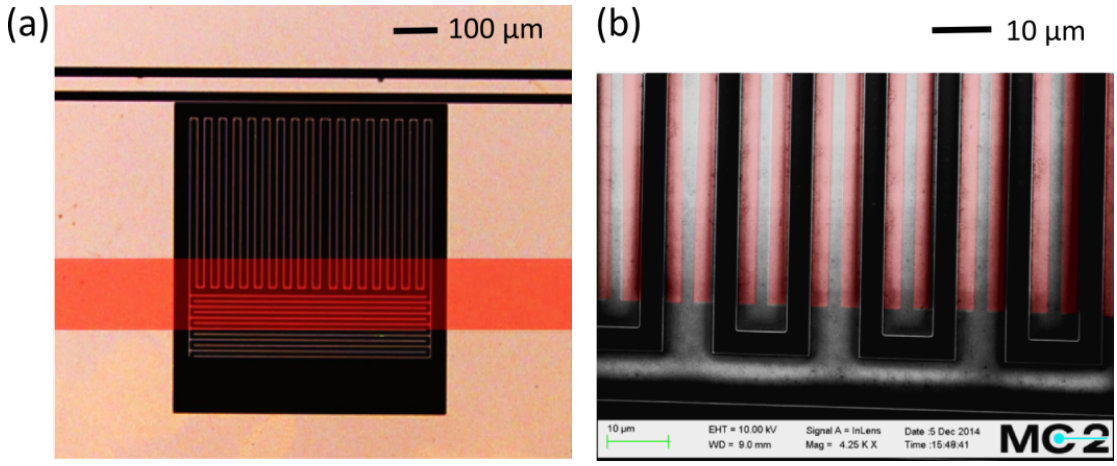

Fig. 6.16 a) Using an optical confocal microscope with polarisation filters during the first fabrication run, the implanted region is visible and is here highlighted with false colouring. Misalignment is observed between the implanted region and the microresonator inductor. This was later understood to be due to an error in the CAD files between layers. b) Alignment is greatly improved during the second fabrication run. Here, implanted regions are visible by scanning electron microscope (SEM) and can be observed perfectly aligned underneath the individual inductor meander lines.

transmission line and the ground plane with vias to suppress measurement interference due to standing modes, a design previously used within the group. 3 or 4 Aluminium (Al) bond wires connect the PCB transmission line to the sample transmission line via the contact triangles. A high density of Al bond wires also connects the sample ground plane to the PCB ground. Fig. 6.17 shows an example of the PCB and sample configuration used for a majority of this work.

The choice of sample

The main focus of the experiments in this work is a 10x10 mm chip fabricated in the first fabrication run. The sample contains 9 frequency multiplexed, inductively coupled resonators of different designs beneath which lie a 100 μm thick region of Gd^{3+} ions implanted at a dose of 10^{14}, to a device design shown in Fig. 6.18 (grey).

The measurements focus in particular on a lumped element (LE) device with resonance frequency

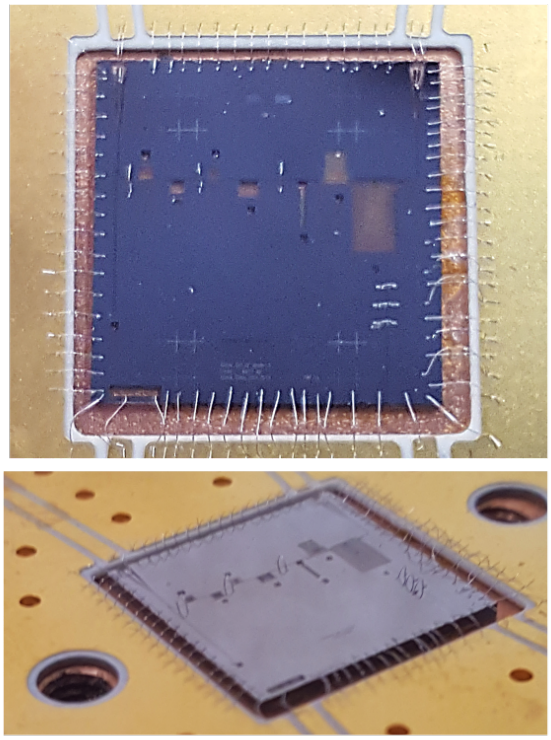

Fig. 6.17 Photo of typical sample mounted to a copper plate and wire-bonded to a standard PCB design.

$\omega_r/2\pi = 3.352$ GHz and is shown in Fig. 6.19 a). The device lies on top of an area of implanted Gd^{3+}, which is highlighted with false colouring for clarity. The implanted area covered by the microresonator device is approximately 100×250 μm. The implantation concentration profile of the implanted ions in this sample is shown in Fig. 6.19 b).

Many devices were measured over the course of the project, however this device consistently provided results across a number of experimental set-ups and across the 3 year time-span of this project. This is the motivation behind presenting these particular results within this thesis.

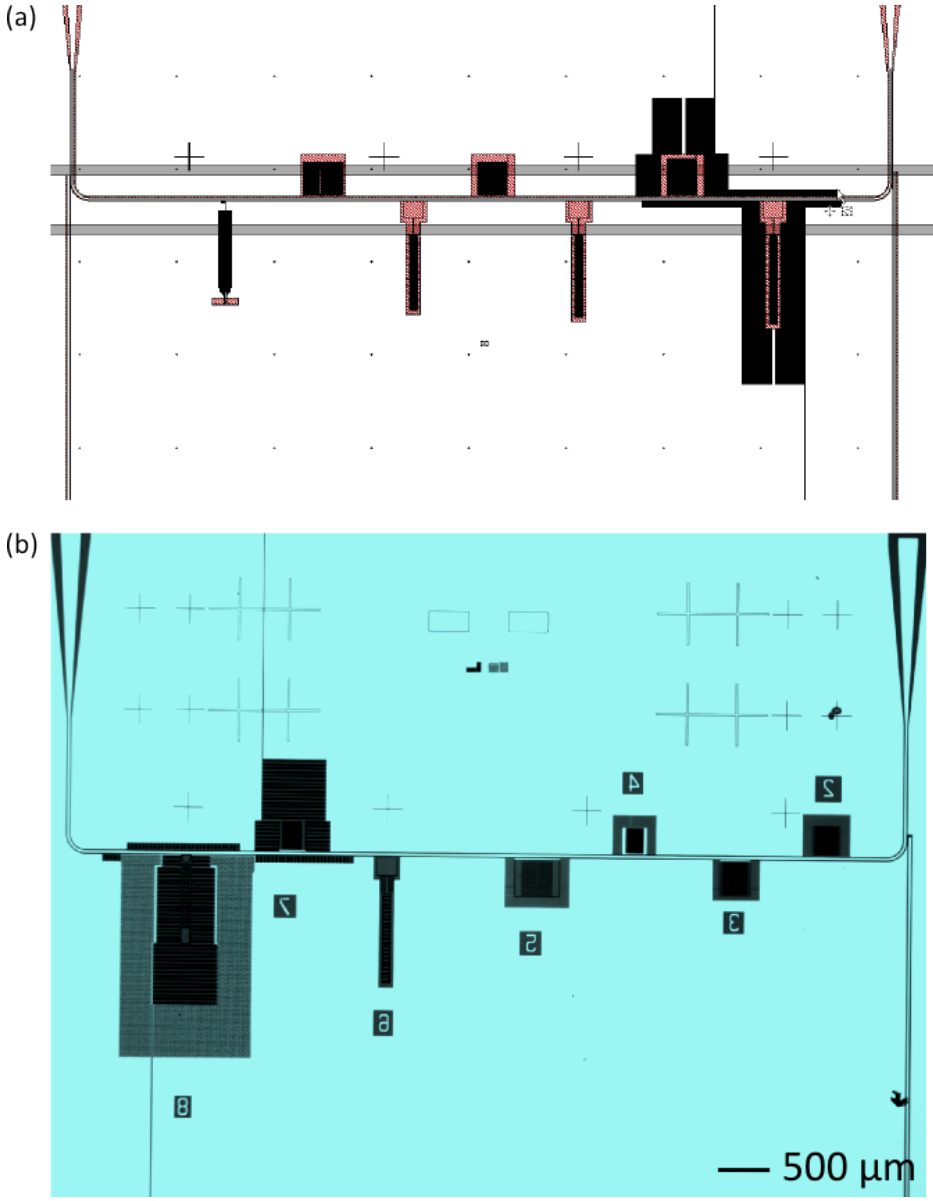

Fig. 6.18 a) Design of the sample which is the main focus of this work. 9 microresonators of various designs ($4-8$ GHz) are inductively coupled to the transmission line. On either side of the transmission line lies a length of implanted spins, of width (100 μm). b) Optical image of the sample of focus.

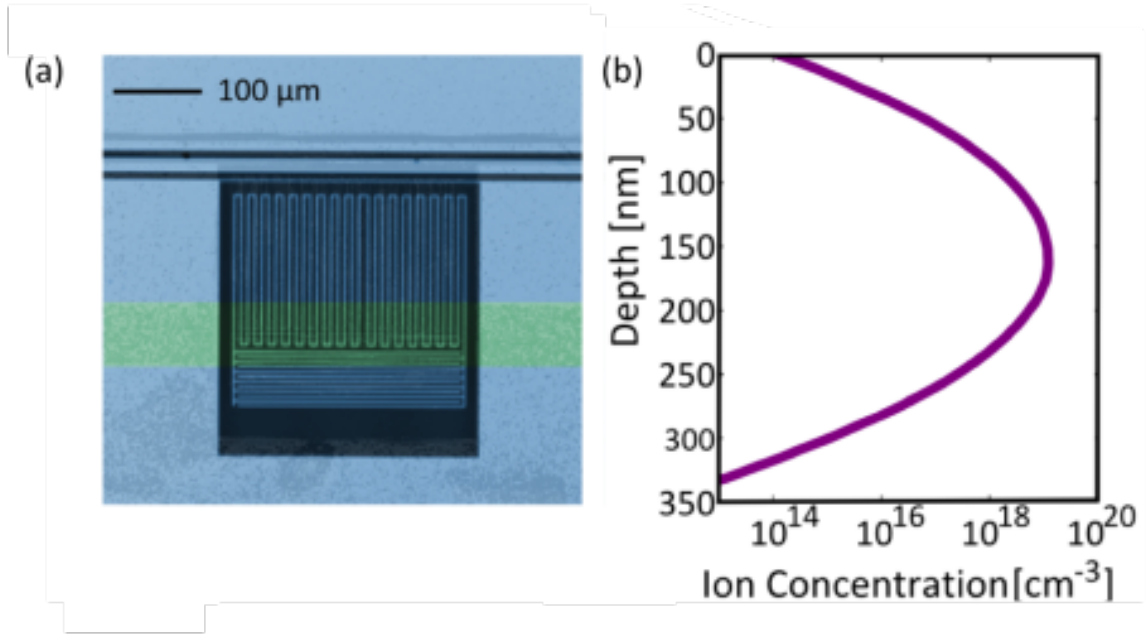

Fig. 6.19 a) Optical image using filtered polarized light, showing a LE resonator coupled to a transmission line with the implanted region highlighted (for clarity) by false colouring. b) The calculated concentration profile of ions with respect to depth for an implantation dose 10^{14} ions/cm^2. The peak implantation depth is 160 nm and FWHM = 77 nm.

Chapter 7

The cryogenic systems, microwave set-up and experimental method

A number of experimental systems were utilised within the course of this project. This chapter provides an overview of the cryogenic systems used alongside the microwave set-up. The experimental method behind the microwave spectroscopy technique at millikelvin temperatures is then presented.

7.1 The cryogenic systems

Experimental investigations across the course of the project were performed using a number of dilution refrigerator units. Each cryostat differed in operation (cryogenic/cryogen free) as well as the capability of the base temperature and magnetic field application. A brief summary of the individual cryostat capabilities and the role of each one within the project is here presented.

7.1.1 The 'Oxford Instruments Triton 200'

The 'Triton 200' is a top loading cryogen free dilution refrigerator with a base temperature of 20 mK. The system is fitted with a 0-12 T superconducting magnet operational in B_z. The system was used at the very beginning of the project whilst awaiting the installation of a more suitable system owned by the group and installed with a vector magnet. Since the system

was not set up for these measurements, microwave wiring and components (low-temperature amplifiers and circulators) were installed. Preliminary measurements were obtained using this cryostat, though the results of this work are not presented in this thesis since higher quality measurements were subsequently obtained in other systems.

7.1.2 The 'Cryogenic' re-condensing cryostat

During the 3rd year of the project, a 'Cryogenic' re-condensing dewar was installed and integrated with an older dilution refrigerator system. Along with the dewar also arrived a superconducting magnet, operational in B_z, capable of operation up to 1.5 T. The integration of the new dewar with the old system was not trivial and required extensive troubleshooting, which was performed over a period of ≈ 6 months to yield optimal system operation. Once operational, a large number of experiments, including those presented in Section 8.1.1, were performed using this equipment.

7.1.3 The 'Blufors' cryogen free system

In the 3rd year of the project, a 'Blufors' cryogen-free system with a vector magnet was installed. The Blufors system was pre-installed with 8 microwave lines and has a base temperature of 8 mK. Time was made available on this equipment to exploit the vector magnet which enabled us to perform angular dependent micro-ESR measurements detailed in Section 8.2

7.2 Sample installation

The sample under investigation is attached to a printed circuit board (PCB) which is in turn attached to a de-oxidized copper plate for thermalisation and mechanical support. This plate is in turn attached to a copper cold finger. The finger thermally anchors to an attachment piece which is used to connect the cold finger to the mixing chamber via a variety of puck designs. This is shown in Fig. 7.1 a).

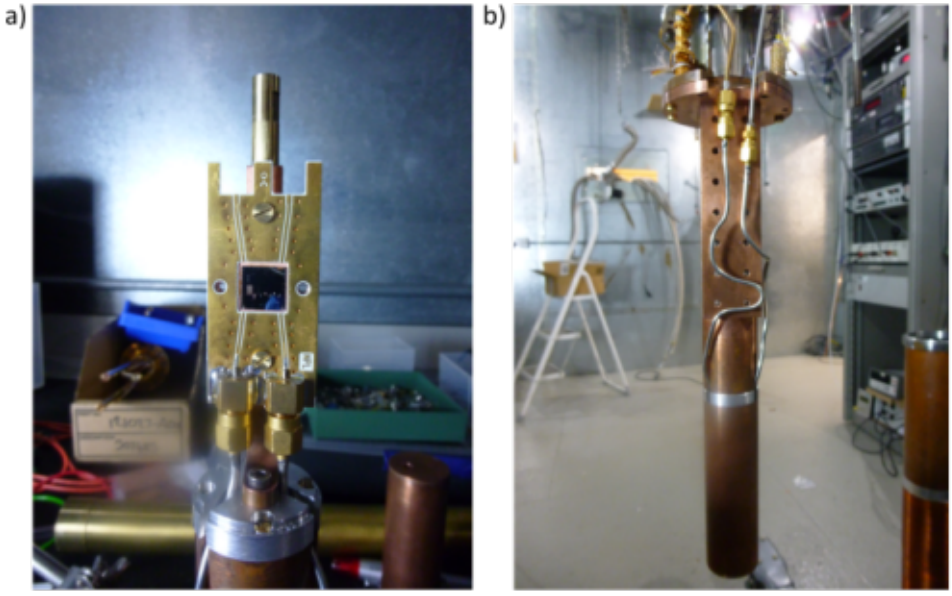

Fig. 7.1 Photographs of a typical a) sample and PCB and copper finger set-up b) covered with an inner can.

An aluminium or copper inner can (depending on application) attaches to the top of the finger, and is shown in Fig. 7.1 b). The open end of the can hugs the inner lip of the attachment, such that the outer edges are flush - acting as a ≈ 50 mK radiation shield. The attachment piece is designed such that it is compatible with a variety of puck designs and is, therefore, compatible across all systems used. The fundamental differences in puck designs are in a) length, such that the sample is always aligned with the centre of an externally applied magnetic field and b) in attachment to the mixing chamber. The puck is then covered with an additional 200 mK radiation shield, reducing interference due to 4 K photons inside the inner vacuum chamber (IVC).

7.3 The microwave set-up

Continuous wave microwave spectroscopy is performed by measuring the S_{21} transmission with a Rohde & Schwartz ZNB Vector Network Analyzer (VNA) and sweeping the magnetic field of a superconducting magnet. Depending on the scope of the set-up, the microwave signal output

from the VNA into the fridge is at a power of ≈ -30 to -20 dB. The signal may be further attenuated at room temperature using 20 dB mini-circuit attenuators.

The microwave in-line typically comprises a high-frequency copper-beryllium-inner-stainless-steel-outer coax from 300-4 K, stainless steel coax from 4 to 1 K, brass from 1 K to the mixing chamber and copper coax from the mixing chamber to the sample. These materials are used to minimise thermal conductivity between stages whilst maintaining good electrical conductivity. The in-lines are attenuated by a total of 50 dB from room temperature. Since measurements are performed at low photon numbers, it is important to ensure cooling of the black-body radiation of the applied microwave signal to ensure a good signal to noise ratio. The attenuation is applied across various temperature stages to ensure thermalisation of the coaxial lines at each stage. This is shown in Fig. 7.2. Additional high pass 3.5 GHz filtering is provided both before and after the sample.

The out-signal passes two cryogenic circulators, where the third port of each is terminated by a 50 Ω resistor, providing sample shielding from any back action of the following cryogenic low noise amplifiers. The amplifiers have a bandwidth of $4 - 8$ GHz, a noise temperature of 5 K and gain of ≈ 28 dB at the 1 to 4 K stage (system dependant). Additional thermalisation is provided by small attenuation to the out signal at the 4 K stage, before passing out of the refrigerator. At room temperature, the signal is often further amplified by a room temperature amplifier.

7.4 Superconducting micro-ESR

We next provide an introduction to the superconducting micro-electron-spin resonance technique which we utilise within this work. It is possible to obtain ESR spectra through the interrogation of the spin ensemble via the microresonator device in a technique very similar to that of standard cavity ESR. Spin-frequency degeneracies are accessible between the spin system and the cavity with the application of an external magnetic field.

An external static magnetic field B_0 is stepped in magnitude. As the magnitude of B_0 changes,

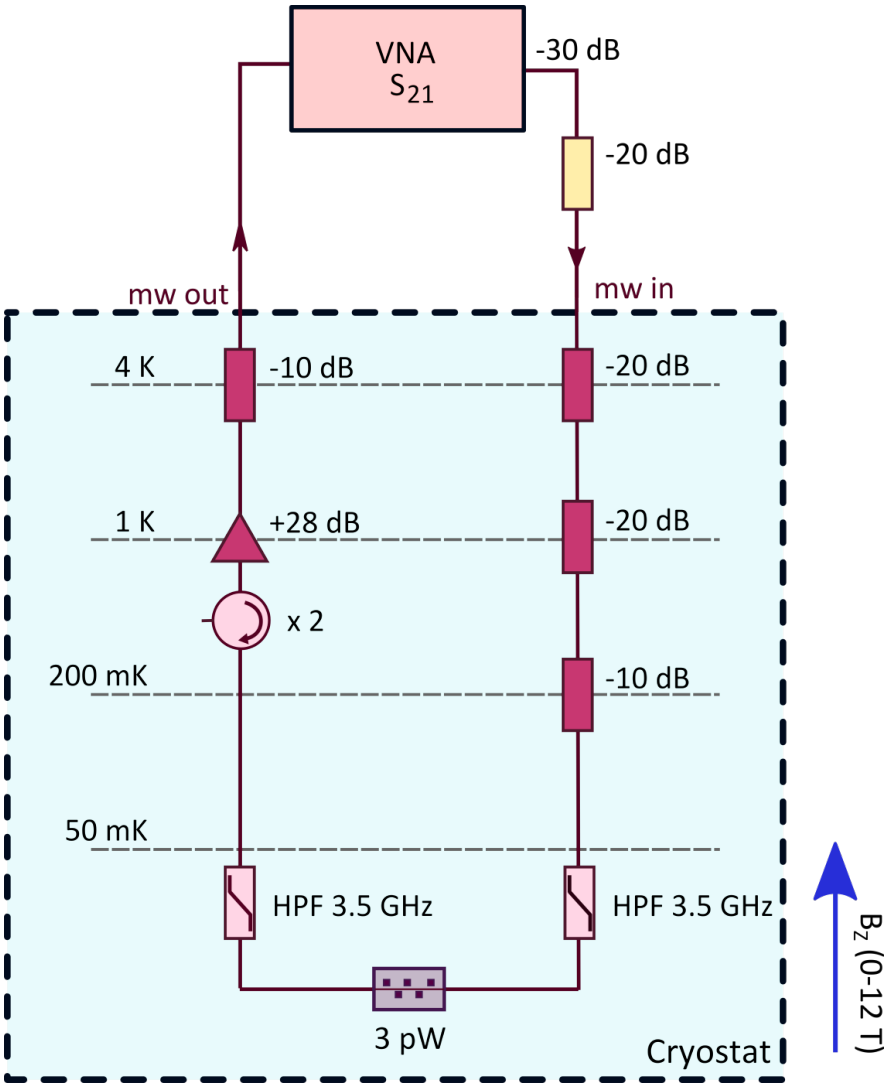

Fig. 7.2 A schematic of the experimental setup: A VNA outputs microwaves of desirable frequency and power. The signal is attenuated further and connected to the cryostat microwave (MW) in-line, which consists of high-frequency coax with 50 dB attenuation and 3.5 GHz high pass filtering (HPF). The MW out-line comprises a high-frequency coax with HPF, and a number of circulators to reduce photon back-action from the low-temperature amplifier. A further 10 dB attenuator is applied for thermalisation. The cryostat also has the capability for an externally applied magnetic field, which, depending on the system, can operate up to 12 T in B_z.

spin ensemble Zeeman transitions are tuned into and out of resonance with the microresonator. The resonator response at each step of B_0 is extracted from S_{21} measurements, which are obtained using a vector network analyser (VNA) (see Section 2.4).

The individual S_{21} traces are fit to Eq. 2.28 in order to extract the resonator Q, Q_i and Q_l. From here, we plot $1/Q_i$ with respect to B_0 to provide an absorption spectroscopy trace. The background magnetic field effects and background at $B(0)$ are substrated from the absorption trace such that only losses due to the ions remain and we have a plot of $\tan\delta_{ions}$ vs B_0. As such, ESR's are observed as an additional absorption mechanism for the applied on-resonance microwave photons.

This trace is then available for spectral analysis. Each observable ESR transition is fit to a equation which describes two coupled harmonic oscillators and the ESR centre field degeneracy B_f, the spin ensemble line-width, γ and the collective coupling rate Γ_{coll} may be extracted. This procedure is further detailed in Section 8.3.

7.4.1 Extracting $\tan\delta_{ions}$

As discussed in Section 2.5, there are numerous quality factors associated with the resonator device which may be extracted. The measured quality factor Q may be broadly separated into losses attributed to coupling to the environment $1/Q_l$ and intrinsic losses $1/Q_i$. The intrinsic losses are attributable to a summation of effects in the dielectric and the magnetic field, as discussed in Section 2.5. The measured quality factor will also be sensitive to losses due to the spin ensemble when the resonator and spin ensemble transition are in resonance. These losses which may be extracted from the intrinsic quality factor,

$$\tan\delta_i = \tan\delta_{diel} + \tan\delta_B + \tan\delta_{ions}, \tag{7.1}$$

The losses due to the ions are isolated by subtracting the zero-field response of the resonator device (regarded as background) and the magnetic field losses from the response. The background magnetic field loss is fit to the overall data (not inclusive of observed ESR transitions) trend

with a polynomial. By this method, an individual absorption spectroscopy trace of loss due to ions can be plotted with respect to applied magnetic field magnitude, such that ESR's are observed as an additional absorption mechanism for the microwave photons, and are viewed as peaks.

The absorption trace may then be analysed using further fitting functions (see Section 8.3) to extract parameters associated with the spin ensemble properties. This method is fundamental to measurements performed in this work and is utilised heavily in Section 8.

7.4.2 Other experimental techniques

A number of other experimental techniques were explored within the project which are not mentioned within this thesis. These techniques include time-resolved spectroscopy techniques, THz spectroscopy and magnetic property measurements. Further details of this work are listed briefly in Appendix D for completeness.

Chapter 8

Measurements and discussions

Before jumping to the experimental results, it is important that we remind ourselves of what we aim to achieved from the project, as set out in Chapter 1. These initial aims included,

1. The development of the integration of a local implantation technique alongside standard e-beam lithography procedures to produced a locally implanted spin ensemble available for coupling to a superconducting microresonator device.

2. The examination of the effect of this fabrication technique on the intrinsic quality factors and crystalline environment of the microresonator devices.

3. Provided previous success: demonstrate the proof of principle of such a hybrid device by achieving coupling between the two systems. Ideally we seek to achieve coherent coupling in the strong coupling regime.

4. Provided previous success: perform pulsed micro-electron-spin-resonance measurements on the device.

We have met the first aim in developing the fabrication procedure to create the locally implanted devices and next seek to determine the device quality. This is achieved by the characterisation of a variety of devices using standard S_{21} measurements. The measured S_{21} responses are then fitted in order to extract the internal properties of the resonator, as discussed in Section 8.1. We compare these parameters between a variety of samples with different implantation parameters,

and also compare these samples to similar samples with no implantation. Overall, we find that to within the level of measurement sensitivity, there is no degradation to Q_i where implantation concentration is less than 100 ppm.

We next move on to explore the ESR responses of the spin ensemble via superconducting micro-ESR experiments in meeting our third aim. From this, information about the spin ensemble's coupling rates, linewidths and quality factor can then be extracted from this data. We observe electron-spin resonances in good agreement with numerical modelling and extract corresponding coupling rates of the order of 1 MHz and spin linewidths of 50-65 MHz. Since we find we are operating in the weak coupling regime, we are not able to perform any pulsed ESR manipulations on the spin ensemble.

Whilst we are not able to achieve pulsed measurements in line with our initial aims, we are instead able to present further measurements examining the locally doped crystals and their structure in detail, on the scale at which coupling is mediated. This is achieved through angular dependent microresonator ESR spectroscopy and temperature dependent ESR measurements. We find the measured angular dependent micro-ESR spectra to be in excellent agreement with the modelled Hamiltonian. This supports the conclusion that the dopant ions are well integrated into their relevant lattice sites and that crystalline symmetries are maintained. Furthermore, we observe clear individual contributions from the spatial components of the microwave field of the microresonator device, emphasising the need for better controlled local implantation. Finally, we present additional preliminary measurements exploring the temperature dependency of a single ESR trace. This work is summarised in publications, Ref. [86, 87].

8.1 Exploring the effect of the fabrication procedure on device quality

We first seek to determine if the integration of the ion-implantation and microfabrication procedures has been detrimental to the device quality. This is achieved by the characterisation of a variety of devices using standard S_{21} measurements. The measured S_{21} responses are then

fit in order to extract the internal properties of the resonator.

The initial characterisation of devices enables us to determine the resulting internal quality of the devices fabricated. By extracting this property, we should be able to compare and determine if there has been any detrimental effect on the superconducting microresonator caused by the local-ion-implantation procedure detailed in Section 6.

To best investigate this, measurements are performed on samples varying in both implantation dose and profile (as detailed in Table 6.1), such that any dependencies on these parameters may be observed. Whilst many more samples were characterised in the course of the project, a summary sample-set representative of each implantation design and dose is here presented for clarity. These samples are detailed in Table 8.1.

Sample	Dose	Implantation	Resonators
(a)	10^{14}	• Hard-nitride mask used • Patterned: 2x200 μm strips	• 6/7 microresonator devices observed • Designs: LE, fractal designs • Frequencies: 2-4 GHz
(b)	10^{14}	• No mask used • Implanted everywhere	• 5/6 microresonator devices observed. • Designs: LE, fractal design • Frequencies: 2-4 GHz
(c)	2.5×10^{13}	• Hard-nitride mask • Multi-implantation profiles	• 4/6 microresonator devices observed. • Designs: LE, fractal designs • Frequencies: 2-4 GHz
(d)	N/A	• Not implanted or processed	• Nb resonators [51] • 5/5 microresonator devices observed. • Designs: LE • Frequencies: 2-4 GHz
(e)	10^{15}	• No mask used • Implanted everywhere	• 1/7 microresonator devices observed. • Designs: LE, fractal design • Frequencies: 2-4 GHz

Table 8.1 A subset of the measured samples and corresponding implantation parameters.

8.1.1 S_{21} measurements and fitting

For each sample measured, the individual microresonator responses are identified and characterised through measurement of the microwave transmission coefficient, S_{21}. This is obtained using a vector network analyser (VNA) to gain phase and magnitude data of the response (see Section 4.2). An example of the raw phase and magnitude data is shown in Fig. 8.1 (blue). The trace is next fit numerically using Matlab Eq. 2.28.

By performing this fitting, it is possible to extract the centre frequency f_0, intrinsic quality factor Q_i, coupled quality factor Q_l, and asymmetry factor, g_a, of each device.

An example of this is shown in Fig. 8.1, where an S_{21} measurement trace is shown from sample (a) detailed in Table 8.1 (blue). The fitted function (red) is used to extract the parameters: $f_0 = 3.076$ GHz, $Q_i = 4.032 \times 10^5$, $Q_c = 3.959 \times 10^4$ and $g = 0.095$.

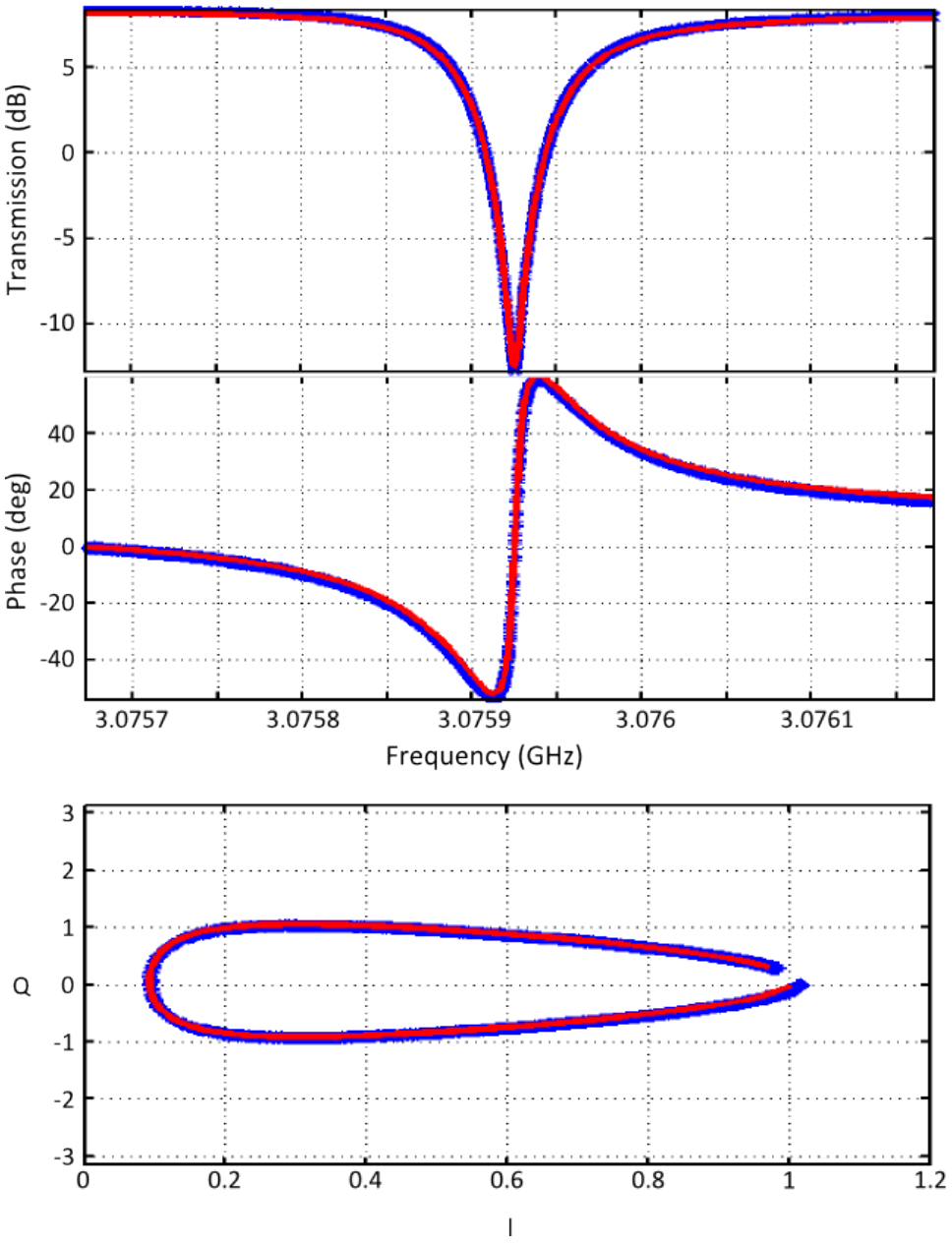

Fig. 8.1 An example of a resonator S_{21} measurement (blue) and fitting function (red). The magnitude response, phase and asymmetry factor fitting factor are shown (top, middle, bottom respectively).

This characterisation is performed on all the samples measured. As previously mentioned, a select few samples of varying implantation parameter dose and implantation profile are presented in this thesis for clarity. Results are shown in Fig. 8.2, which plots the extracted Q_i's of all the measured resonator devices across a number of samples.

From Fig. 8.2 it appears that there is generally very little detrimental an effect on the measured Q_i's due to the ion implantation and micro-processing procedure. This is evident as the extracted Q_i's are comparable to that of a typical non-implanted sample (d).

It is also clear, however, that sample (e), (implanted with no mask at a dose of 10^{15}) does not produce successful resonator devices, with only 1 of the 7 devices providing a resonance response.

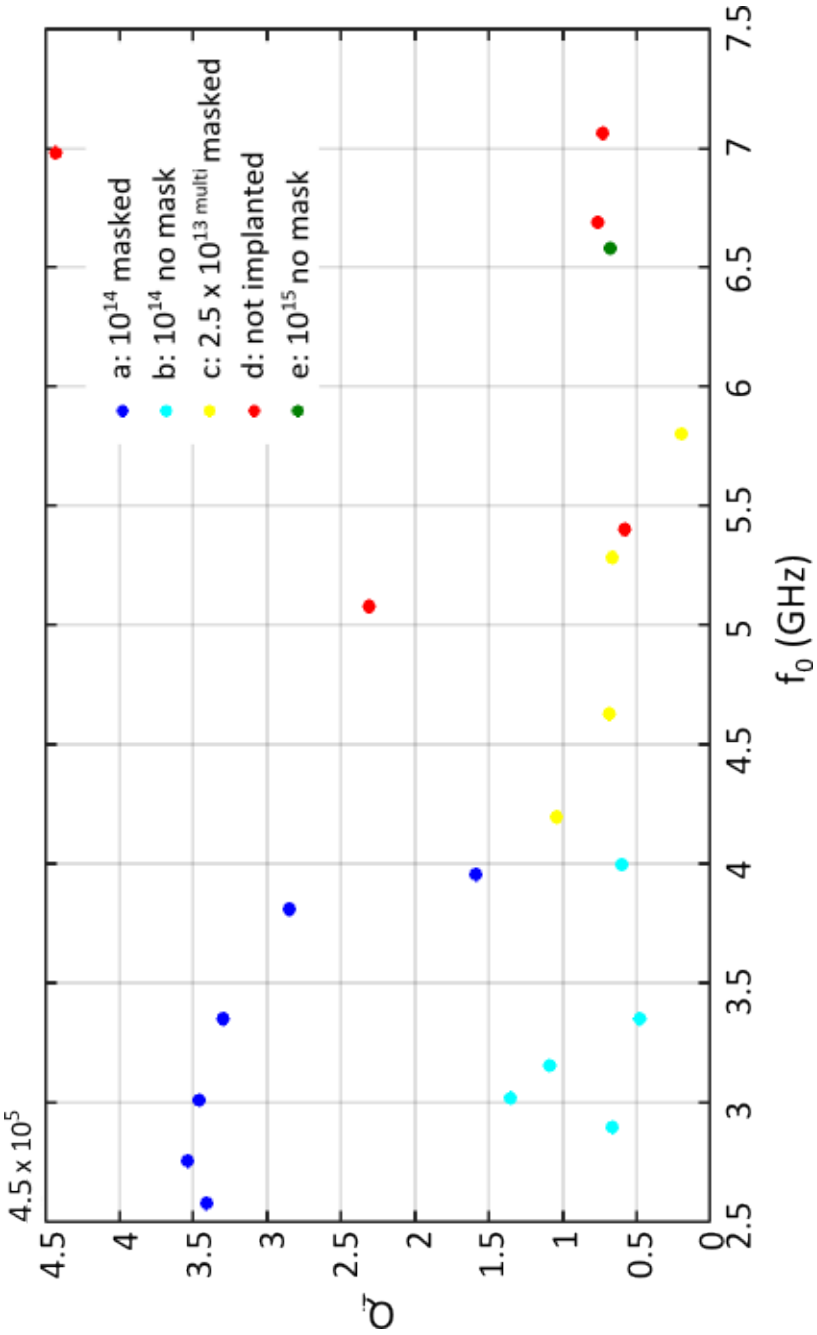

Fig. 8.2 A plot of the extracted Q_i values for microresonator devices measured across a number of samples with a variation in implantation parameters.

8.1.2 Considerations

Looking at the response of sample (e) further - it could be speculated that resonator device responses were unsuccessful due to excess crystalline damage (where an increase in crystal damage is expected from the implantation). However, this does not seem to be the case, since increased crystal or surface damage is likely to result in observable devices responses with dramatically degraded Q_i's. In the case of this data, only one resonator device response is observed, yet has a Q_i's of order 10^5. Another suggestion is that this sample has reached the saturation limit for the implanted Gd^{3+}. If the ion concentration is too high, the resulting ensemble may be considered as a mono-layer of Gd^{3+} ions - either dramatically changing the dielectric properties of the substrate, or, in effect, shorting the resonator devices. Without further investigation using other techniques, it is very difficult to understand the mechanisms behind these results from this measurement alone.

It is also interesting to observe that the devices fabricated in the masked sample (a), with an implantation dose of 10^{14} have higher extracted Q_i's than all of the other samples featured. This could be surprising, particularly when compared to the non-implanted sample (d). This simply demonstrates the high quality of fabrication of these samples, which were fabricated in different clean room environments and at different times.

Sample (a) is also superior in quality to sister sample (b). Both samples have an implantation dose of 10^{14}, whilst sample (b) is fabricated without an implantation mask resulting in implantation all over the sample area, sample (a) utilises the hard-nitride mask technique and has implanted regions of 200 μm beneath the resonator devices. These results imply that this local implantation technique yields higher quality devices. Sample (c) is fabricated with a multi-implantation profile with a lower implantation dose. Despite this, Q_i's are slightly lower as this profile requires higher implantation energies. Irrespective of these observations, the Q_i's of all the samples with different implantations are comparable in quality to the non-implanted sample (d).

8.1.3 Initial conclusions

From these measurements, it can be concluded that a maximal implantation dose of 10^{14} is required for successful fabrication of devices. This in agreement with the hypothesis of Ref. [62], who believed that at 'low concentrations' of 100 ppm, there would be no detrimental effect to the lattice (as discussed in Section 3.4). Within this limit, it can be concluded that the ion-implantation and micro-processing do not affect the intrinsic quality factors of the other devices, which are comparable with Q_i's of microresonator devices of the previous study in this group [64].

8.1.4 Sample of further measurements

Sample. (a) of Table 8.1 is from here-out the focus sample of this thesis. Whilst many devices were explored throughout the project, this is the sample with the most complete and extensive measurements.

The sample consists of 7 frequency multiplexed, inductively coupled resonators which sit on top of a 200 μm wide strip of Gd^{3+} spins implanted at a dose of 10^{14}. Initial characterisation of the device is obtained by performing S_{21} frequency sweeps about the resonance responses and fitting these using Eq. 2.28 as just discussed. From these measurements, it is ascertained that 6 of the 7 expected microresonator devices are observed within the 2-8 GHz range. Individual S_{21} data is taken and fit for each device at $B_0 = 0$, and at $T \approx 20$ mK. The extracted parameters are detailed in Table 8.2. Of the 6 resonators on this sample, device (3), the 3.35 GHz LE microresonator is presented as the focus of study. S_{21} data obtained from this resonance at T $\approx$ 50 mK is shown in Fig. 8.3. The extracted $Q_i = 3.3 \times 10^5$ and coupled quality factor $Q_c = 3.8 \times 10^4$, gives this resonator a zero-field dissipation rate of $\kappa/2\pi = \omega_r/Q_i = 0.13$ MHz.

Device	f_0(GHz)	Q_i	Q_l	g_a	Design
1	2.759	3.54×10^5	3.23×10^4	0.047	LE
2	2.579	3.41×10^5	2.81×10^4	-0.133	Fractal resonator
3	3.351	3.3×10^5	2.97×10^4	-0.30	LE, dotted ground plane
4	3.013	3.46×10^5	3.8×10^4	0.077	LE, fractal ground plane
5	3.810	2.85×10^5	1.85×10^4	0.235	Fractal, SDG design
6	3.958	1.59×10^5	6.84×10^4	0.301	LE dotted ground plane

Table 8.2 Table of extracted parameters of the 6 resonators observed on sample (a).

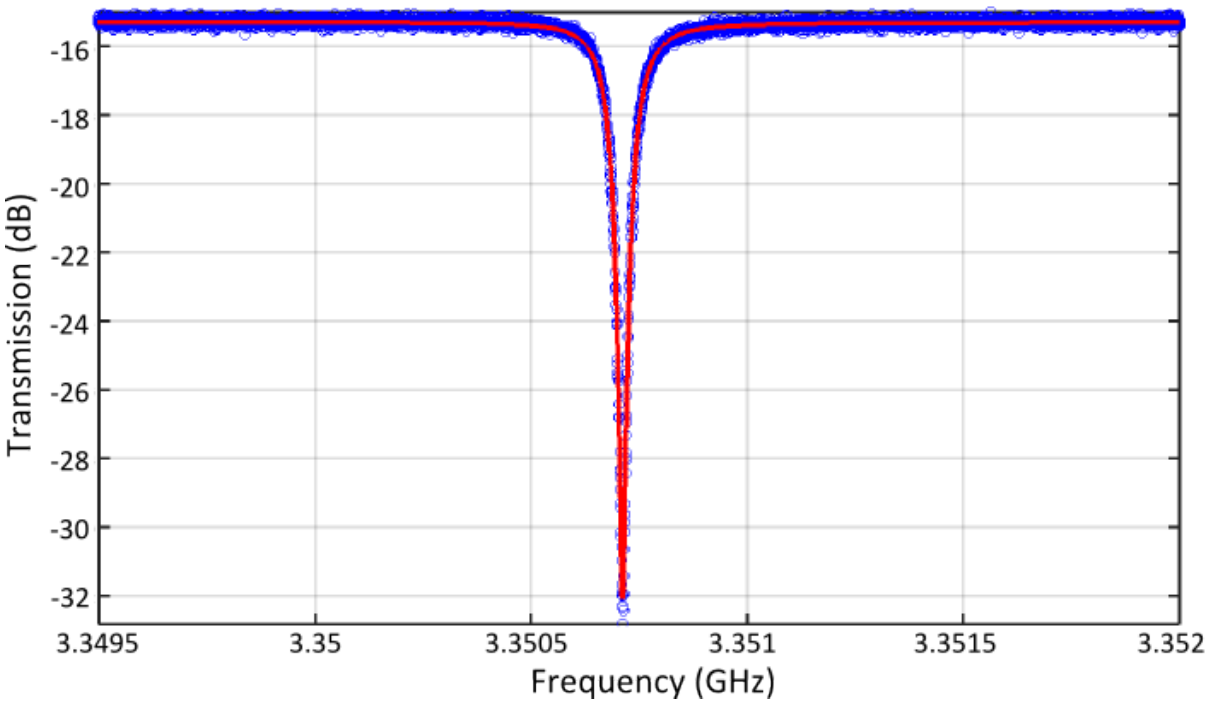

Fig. 8.3 An S_{21} trace of sample (a) device (3), taken at T $\approx$ 20 mK. The data (blue) is overlay with a fitted function (red). This fit yields an extracted $Q_i = 3.3 \times 10^5$, a coupled quality factor $Q_c = 2.97 \times 10^4$ and $g_a = -0.30$.

8.2 Angular dependant superconducting micro-ESR spectroscopy

We next perform angular dependant micro-ESR on the sample (a), device 3 (see Table 8.2) using the measurement technique outlined in Section 7.4. Before beginning the micro-ESR, it is important that the applied magnetic field is aligned to the mounted sample's superconducting plane. The method behind achieving this is first explored before the micro-ESR trace is presented. Finally, the angular-micro-ESR trace is presented and analysed.

Magnetic field alignment

Initial experiments are performed in the 'Cryogenic' dilution refrigerator (see Section 7.1), which is fitted with magnet operational in B_z. The sample is positioned such that it sits within the centre of the superconducting magnet bore. and is mounted with the crystal r-plane and superconducting thin film parallel to $B_0 = B_z$ (green), as depicted in Fig. 8.4. Performing experiments with B_0 parallel to the superconducting thin film is advantageous since it has been shown to be beneficial in minimising flux focusing in the superconductor [58]. However, since this experimental set-up includes a magnet only tunable in magnitude in B_z, the degree of parallel alignment cannot be optimised resulting in an unknown degree of error in θ and ϕ (as shown in Fig. 8.4). An advantage to using the 'Blufors' dilution refrigerator (see Section 7.1) which is fitted with a $B_{x,y,z}$ vector magnet, is that misalignment can be compensated for by minor rotation of B_0 in θ and ϕ. This experimental set-up is therefore utilised from here-on. Alignment is optimised by exploiting the microresonator NbN properties of kinetic inductance in the field, such that optimal field alignment corresponds to a centre frequency maximum (see Section 2). This process is performed using the vector magnet, sweeping B_0 $\pm 10°$ about nominal zero at a magnitude of 10 mT, first in θ and then in ϕ. For each angle, S_{21} data is obtained and fitted to extract the f_0 response, and is plotted with respect to the variation in θ/ϕ such that the frequency maximum is found. The measurement is then repeated around

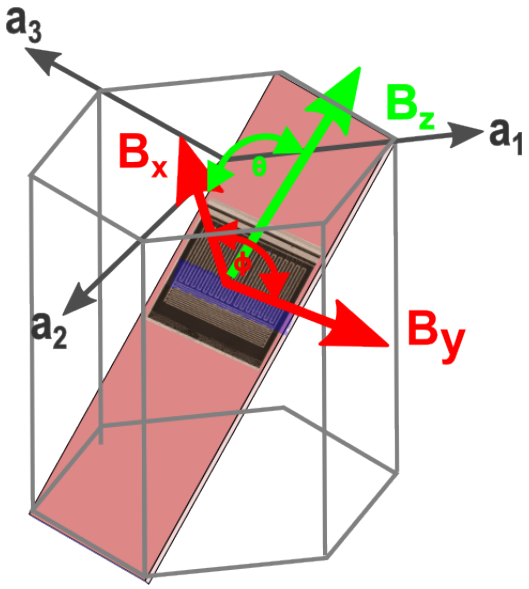

Fig. 8.4 Schematic depicting the LE microresonator device on r-cut sapphire substrate. Magnetic field components B_z and B_y are parallel to substrate and superconductor plane whilst B_x is perpendicular. The magnetic field is aligned by sweeping the applied B_0 in ϕ and θ.

this frequency maximum at a higher resolution, shown in Fig. 8.5 a) to find a residual offset in $\theta = +0.6°$ and $\phi = -1.8°$. The process is repeated to find an offset in $\phi = -1.8°$ whilst applying the residual offset in $\theta = +0.6°$ and is shown in Fig. 8.5 b). The required offsets are maintained throughout all measurements from this point.

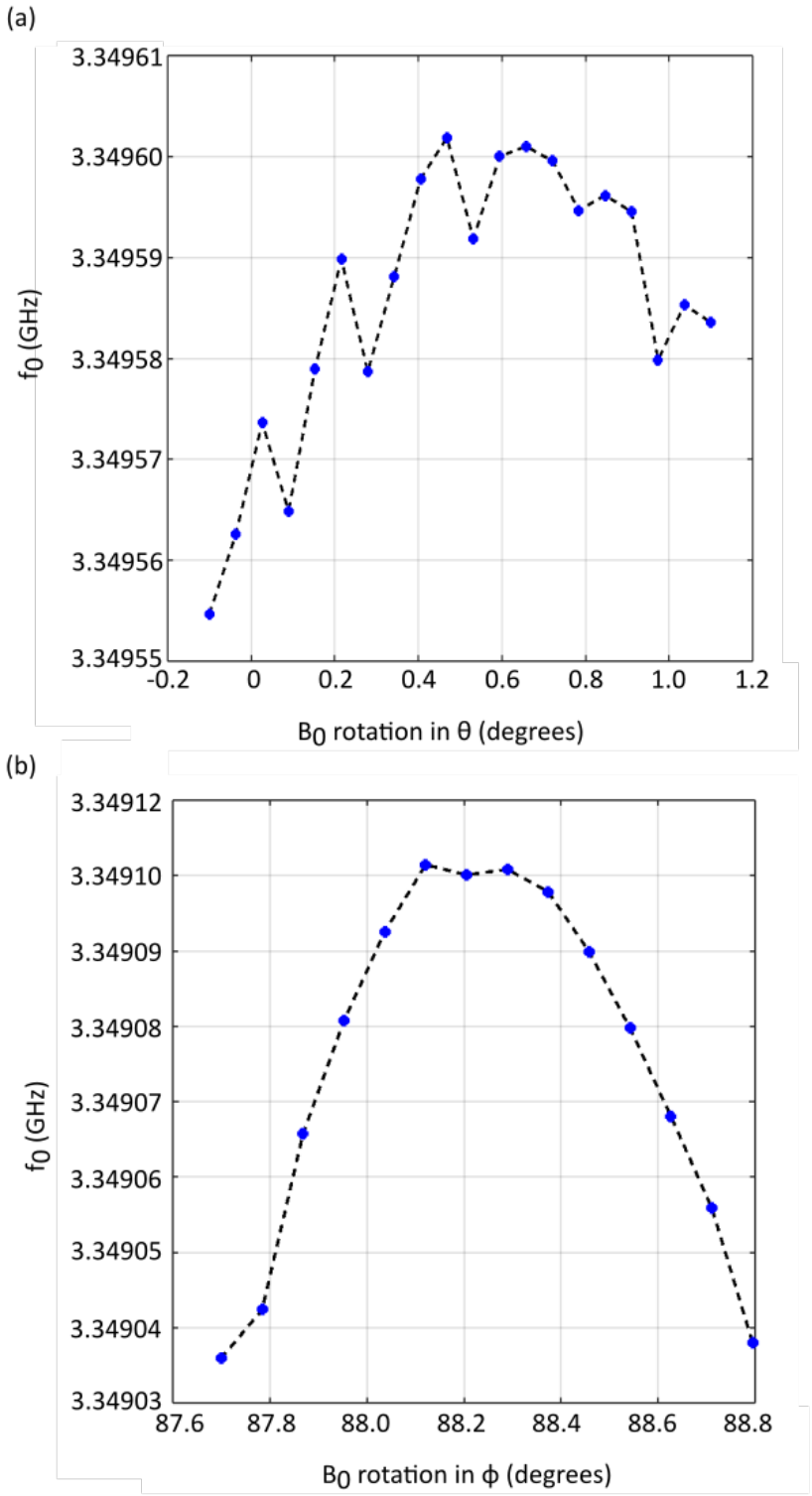

Fig. 8.5 The magnetic field is aligned by sweeping the applied B_0 in ϕ and θ and extracting the resonator f_0 response. The frequency maximum depicts alignment offset a) in θ from 0°: $\theta = +0.6°$ b) in ϕ (with applied θ residual offset applied) from 90°: $\phi = -1.8°$.

A single absorption spectroscopy trace

A single absorption spectroscopy trace is performed on the sample (a), device 3, through the absorption spectroscopy technique described in Section 7.4:

To summarise again for clarity, B_0 is stepped in magnitude and resonator response at each step of B_0 is extracted from S_{21} measurements, which are obtained using a vector network analyser (VNA). The individual S_{21} traces are fit to Eq. 2.28 in order to extract the resonator Q, Q_i and Q_l. From here, we plot $1/Q_i$ with respect to B_0 to provide an absorption spectroscopy trace. The background magnetic field effects and background at $B(0)$ are substrated from the absorption trace such that only losses due to the ions remain. As such, the resulting trace is that of $\tan\delta_{ions}$ vs B_0 and the ESR's are observed as an additional absorption mechanism for the applied on-resonance microwave photons.

The resulting trace is shown in Fig. 8.6 a). As the magnetic field is increased, ESR's are observed as an additional absorption mechanism. By eye, ESR features are observed at $\approx 43, 65$ and 83 mT, and are analysed in greater detail later in this section. There are some experimental anomalies within this data, presenting as single points of high loss. Whilst these at first may seem like exciting points where peaks are observed with line widths of greater resolution that the experimental B_0 magnitude step-size, on closer inspection, these are (disappointingly) occasions where the fitting function has failed. Fitting function failure can be attributable to numerous factors, including poor experimental set-up (ie. small boundaries) or constraints applied to the fitting function itself.

In addition to the loss tangent data, the microresonator f_0 response is also presented with respect to the increasing magnetic field, see Fig. 8.6 b). A frequency response is also expected in the form of an avoided crossing provided operation is in the weak-strong or strong coupling regimes, as discussed in Section 4. Whilst ESR transitions are clearly observed within the loss tangent data, no deviation in f_0 response is seen - suggesting that the system is operating in the weak coupling regime. Further analysis and discussion of these results are shown in Section 8.3, where important parameters such as the spin ensemble's spin coupling rate $\Gamma_{coll(m)}$ and spin-ensemble linewidth γ are extracted for each measured transition.

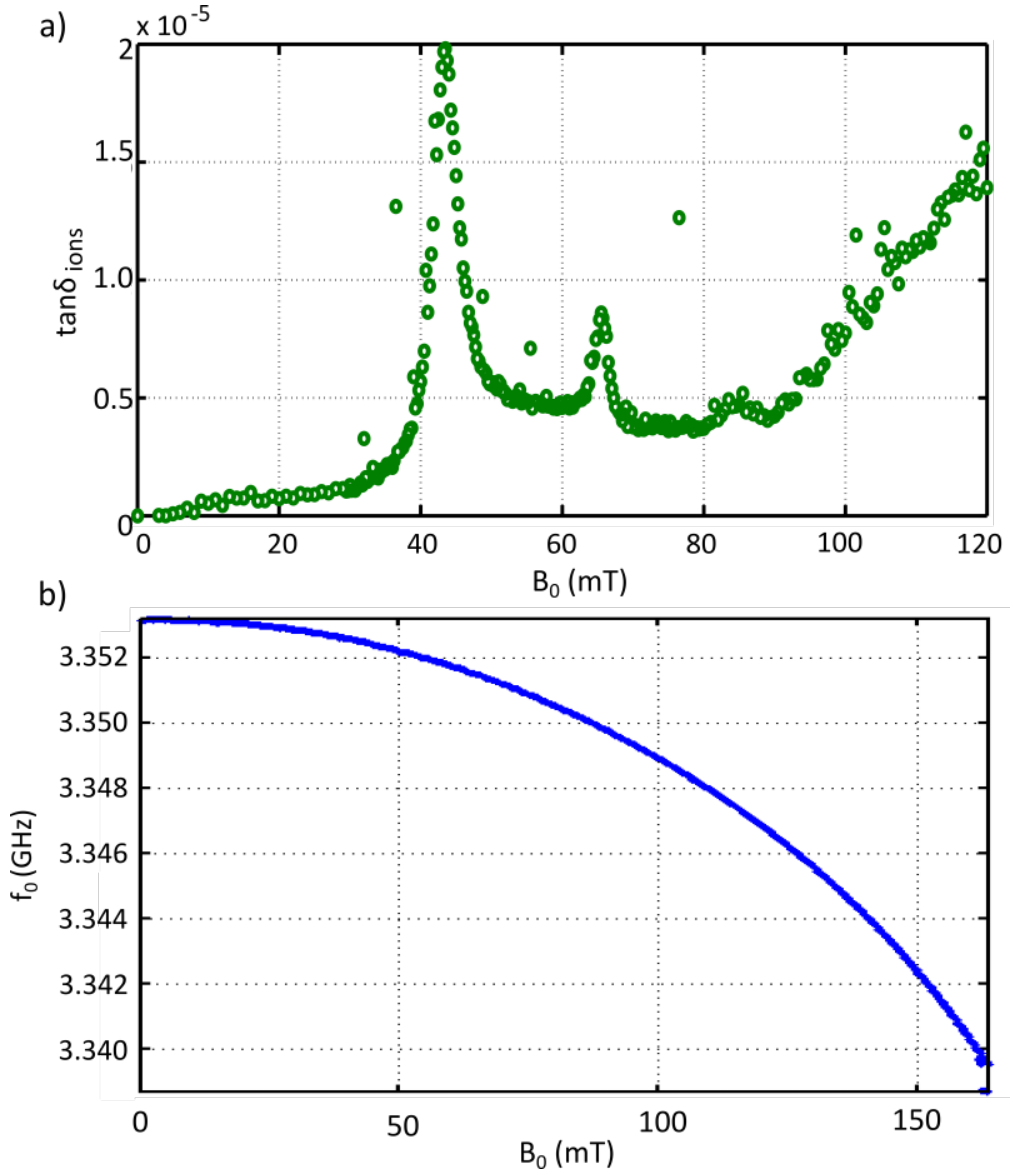

Fig. 8.6 a) An example of an absorption spectroscopy trace: loss due to ions is plotted with respect to applied magnetic field magnitude, such that ESR's are observed as an additional absorption mechanism for the microwave photons, and are viewed as peaks - here key features are observed at $\approx 43, 65$ and 83 mT. Singular points of high loss are experimental anomalies where the fitting function has failed to fit the trace accurately. b) Centre frequency response of the resonator with response to B_0. There is no deviation in f_0 suggesting that operation is in the weak coupling regime.

Angular absorption spectroscopy

By employing the use of a vector magnet, angular dependant absorption spectroscopy is performed on the sample. The sample is mounted and aligned as previously described in Section 8.2 with the assumption that a nominal zero angular rotation is defined whereby $B_0 = B_z$. The applied B_0 is rotated in 4° intervals about a full 360° in the r-plane of the Al_2O_3 substrate. For each B_0 rotation, an absorption spectroscopy trace is obtained.

This experiment was performed at an elevated temperature of 250 mk. This was decided so that we could observe higher-order transitions within the spectra, where higher energy levels are populated as described by the Boltzman distribution, see Section 4.2.3. From the modelling, 250 mK presents as a region of interest, where numerous transitions should be present with good relative intensities. Additional advantages to this temperature are that the microresonator device maintains a high-quality factor, whilst temperature stability of the system can also be accurately maintained.

The result of this angular absorption spectroscopy experiment is shown in the form of an intensity plot in Fig. 8.7. An edge detection filter has been applied in MATLAB in order to enhance the visibility of the weaker transitions by eye in this figure. In this way, areas of high contrast correspond to ESR's, with each individual B_0 angle comprising an individual trace as in Fig. 8.6, if plot individually against B_0 magnitude. This is highlighted by the yellow dotted overlay in Fig. 8.7, which corresponds directly to the trace presented in Fig. 8.6 a) at a 5° rotation.

The process of obtaining such an angular dependent spectra is relatively slow, requiring temperature stability for a period of approximately 24 hours. It is also highly undesirable to change the applied magnetic field angle or magnitude at any great speed, which may result in excess flux trapping within the superconductor.

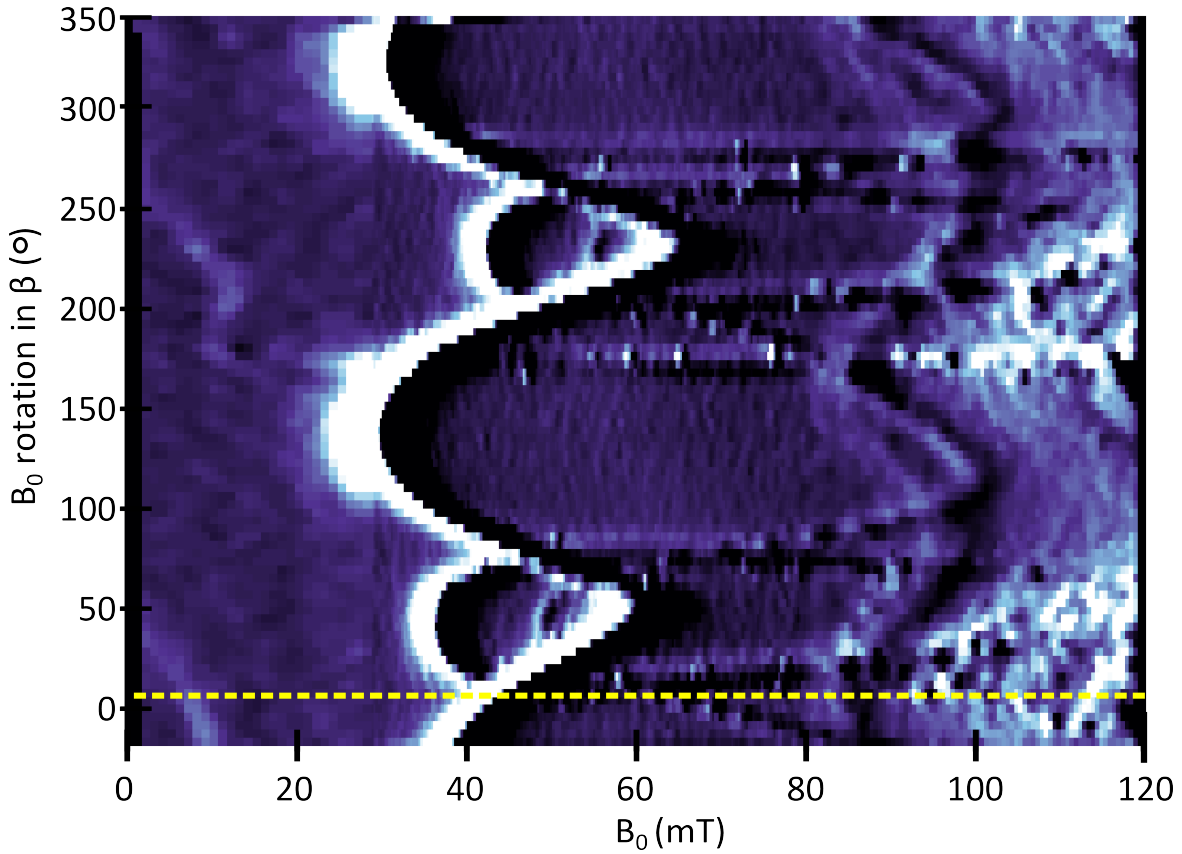

Fig. 8.7 Intensity plot of the total angular dependant ESR spectra obtained by the micro-ESR absorption spectroscopy technique. Areas of high contrast correspond to ESR's. The yellow dotted overlay at a 5° B field rotation corresponds to the trace presented in Fig. 8.6.

8.3 Analysis and discussion

Through analysis of the angular absorption spectroscopy data, a number of important parameters can be extracted using curve fitting functions. These include the spin ensemble transition degeneracy fields B_f, the spin ensemble linewidths, γ and the collective coupling rates, Γ_{coll}. These are extracted as follows:

The features of a single absorption spectroscopy trace can be fit with a number of convolved functions where the spin ensemble and cavity are modelled as a single mode harmonic oscillator, as performed in Ref. [25]:

$$Q_m(B) = \frac{\Delta^2 + \gamma^2}{2\Gamma^2_{\mathrm{coll(m)}}\gamma + \kappa(\Delta^2 + \gamma^2)}\omega_r, \tag{8.1}$$

where Δ is the detuning from the fitted ESR transition, B_f, ($\Delta = B - B_f$), ω_r is the resonance centre frequency, κ is the cavity linewidth = 0.13 MHz, γ is the spin linewidth and $\Gamma_{\mathrm{coll(m)}}$ the collective coupling strength.

Each absorption spectroscopy trace is fit to a summation of the convolved function expressed in Eq. 8.1 using the MATLAB curve fitting toolbox. The fitting function is guided with a start points in finding B_f and by applying constraints to κ. The start points for the B_f fitting are guided from the transition values obtained EasySpin modelling (B_{m}) when simulating the trace. These individual functions are convolved until the fit RMS error between data has $> 97\%$ fidelity. This results in a total number of functions, where many are attributable to the Gd^{3+} system, and additional functions are attributable to background impurities. An example of such a fit is demonstrated in Fig. 8.8 (blue) overlaying the data previously shown in Fig. 8.6. The parameters extracted from this fit are detailed in Table 8.3. The parameters extracted and shown in Table 8.3 and are discussed more extensively later in this section.

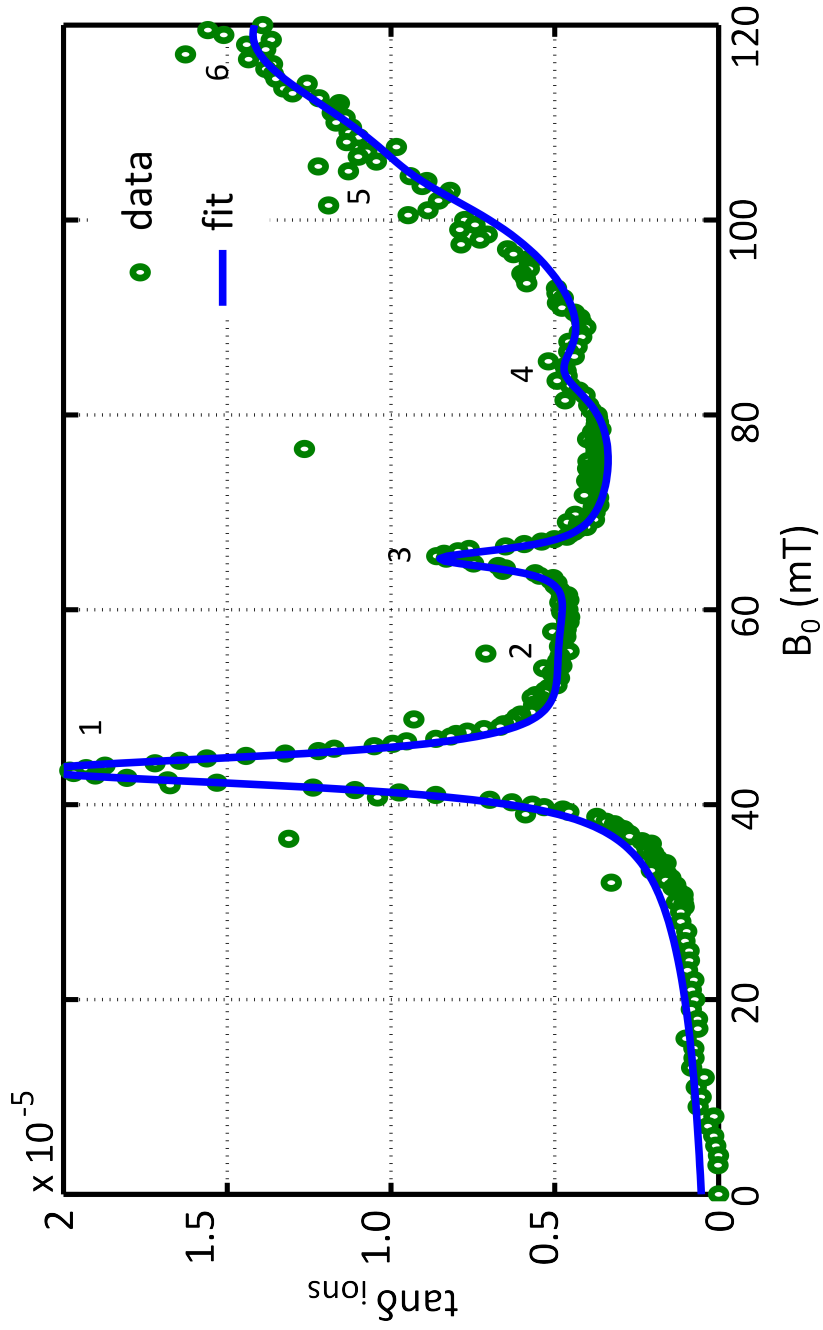

Fig. 8.8 An individual absorption spectroscopy trace taken for B_0 rotated 5°. The $\tan\delta_{\text{ions}}$ data is shown in green whilst the numerical fit is overlay in blue. The fit is a convolution of functions of Eq. 8.1's, and the extracted parameters are detailed in Table 8.3.

Peak_m	B_f (mT)	γ (MHz)	$\Gamma_{coll(m)}$ (MHz)
1	44	53	4.5
2	57	500	4.3
3	66	34	1.8
4	85	100	1.7
5	104	150	2.1
6	119	450	3.0

Table 8.3 The resulting fit shown in Fig. 8.8 is convolved with 6 Eq. 8.1's, with the above extracted parameters, presented in ascending magnetic field centre frequency order. Peaks $1, 3, 4$ and 5 are attributable to the Gd^{3+} system, whilst 2 and 6 are background impurities.

What is immediately apparent from these results are the larger than expected values of γ, where linewidths are an order of magnitude larger than expected. Potential mechanisms behind these excessive linewidths are discussed in further detail in Section. 8.3.3.

From these extracted parameters, we can infer that the system is operating in the weak coupling regime, since the extracted $\Gamma_{coll(m)}$ is an order of magnitude less than the extracted γ in all cases, see Section 4.2.2. This is despite operation where $\Gamma_{coll(m)} > \kappa$, suggesting that excessive line-with broadening is the limitation of the coupling regime. This conclusion is further supported by the fact that no avoided crossing is observed in the frequency response of the microresonator device.

8.3.1 Electron spin resonance measurements

We first wish to explore the veracity of the extracted data. To do this, comparisons made between the spin frequency degeneracy points obtained from the experimental fit, B_f and those obtained from EasySpin modelling, B_m (as described in Section 5.1). This comparison may provide further information about the transitions, for example, which are attributable to the Gd^{3+} system, and which are as a result of impurities/other unknown ESR's.

We begin by running the EasySpin simulation for the Gd^{3+}:Al_20_3 system when rotated in β, with the appropriate temperature parameters to replicate the experiment.

We next overlay the extracted B_{m} parameters with those B_{f} obtained experimentally. We find we may optimise the overlay with minor ($< 3\%$) adaptation of the modelled spin Hamiltonian: changing b_2^0 from +3123 to +3153 MHz.

This comparison of results are shown in Fig. 8.9(a), where the experimentally obtained angular-ESR spectra is shown with the modelled values of the expected B_{m} overlay. For clarity, we also present the previous data presented in Fig. 8.6, in Fig. 8.9(b). The previous trace additionally has the extracted B_{f} degeneracy points marked as vertical lines. Transition intensity is represented by line height. The trace corresponds to the angular ESR trace at $B_0 = 5°$ (yellow) in Fig. 8.9(a). We will discuss the meaning behind the red and pink lines marked 'B_m perp' and 'B_m par' later in the section.

Comparing a single trace: modelled and experimental results

We next look to compare the modelled and fitted results of the trace presented in Fig. 8.9(b). The extracted parameters from modelled results are presented in Table 8.4: where the peak is labelled 'Peak$_m$' corresponding to the marked lines in Fig. 8.9(b). The modelled magnetic field transition frequencies of these points are next stated in column 2 under B_m, alongside the transition component mode as parallel or perpendicular (see Section 5.1.4).

The experimentally determined magnetic field transition frequencies B_f are then aligned in the table with the peak notation 'Peak$_f$' where possible, such that they correspond to the most similar B_m. For example, modelled Peak$_a$ with $B_m = 43.4$ mT corresponds to experimentally extracted Peak$_1$, with $B_f = 44$ mT. This is also observable within Fig. 8.9(b). Those experimentally obtained frequency degeneracies with no corresponding modelled transitions are listed at the bottom of the table as impurities. The experimentally obtained parameters also included the collective coupling rates, $\Gamma_{coll}(m)$ and linewidths, γ.

Looking at Table. 8.4, it is clear that the transitions which are both observed experimentally and that are expected in modelling are in excellent agreement. Whilst Peak$_{\mathrm{d}}$ is expected from modelling, it is not observed experimentally. On closer consideration and playing with the model further, it becomes apparent that this is not surprising. This is because the Peak$_{\mathrm{d}}$'s

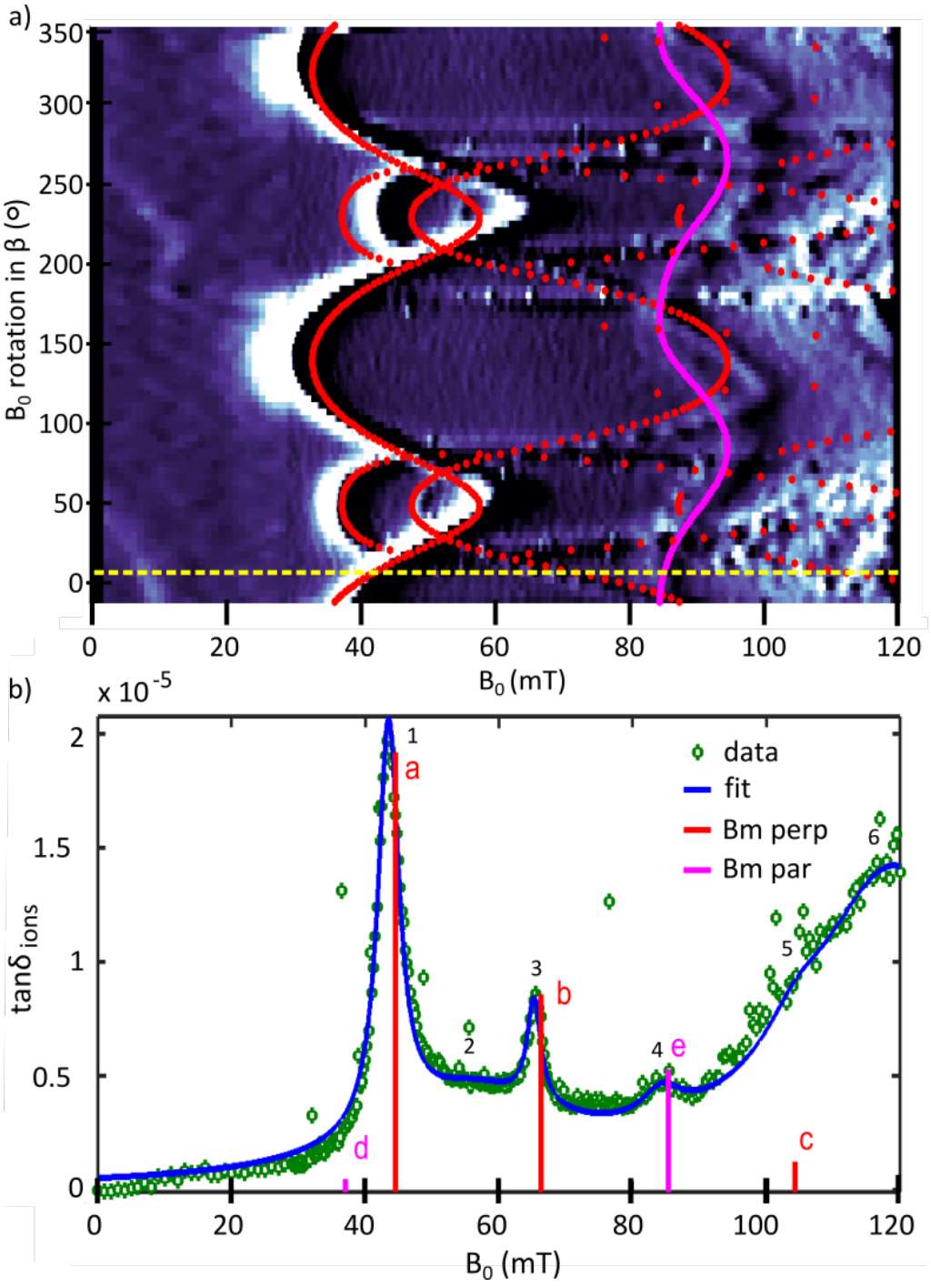

Fig. 8.9 a) Intensity plot of the total angular dependant ESR spectra with modelled spin degenerate field positions B_m. Red is modelled operation in `'perpendicular'` mode, and pink in `'parallel'` mode. Yellow line depicts the position of the trace in b) and Fig. 8.6, at $B_0 = 5°$. b) Raw data (green), fitting function (blue) and expected spin degeneracy fields from modelling (B_m), for perpendicular (red) and parallel (pink) modes, with height representing relative intensities.

Peak_m	B_m (mT)	System	Peak_f	B_f (mT)	γ (MHz)	$\Gamma_{coll(f)}$
a	43.4	Gd^{3+} $\perp$	1	44	53	4.5
b	65.4	Gd^{3+} $\perp$	3	66	34	1.8
c	104.3	Gd^{3+} $\perp$	5	104	150	2.1
d	37	Gd^{3+} $\parallel$	n/a	n/a	n/a	n/a
e	84.1	Gd^{3+} $\parallel$	4	85	100	1.7
n/a	n/a	Impurities	2	57	500	4.3
n/a	n/a	Impurities	6	119	450	3.0

Table 8.4 details the EasySpin modelled spin resonances B_m alongside the fitted spin resonance frequencies, B_f. Where B_m and B_f correspond, they are tabulated beside each other. Additionally, experimentally fitted linewidths, γ and collective coupling rates $\Gamma_{coll(f)}$ are listed. Peak_m and Peak_f correspond to the modelled and fit transition centre frequency points marked in Fig. 8.9(b).

relative intensity to the intensity of the highest populated transition at $T = 250$ mK is less than 1%.

In addition to this, two peaks observed experimentally ($\text{Peak}_{2,6}$) are not predicted from modelling. Presumably, these two features are not attributable to the Gd^{3+}:Al_20_3 spin system, and may be due to impurities. It is interesting to note that linewidths associated with these transitions are excessively large at 450-500 MHz, suggesting a broad distribution. There is speculation that the feature could be attributable to background Fe impurities, or, is a surface spin effect. The latter theory is currently under investigation within the group by S. E. de Graaf. Interestingly, Peak_2 has previously been observed experimentally in literature in the $8 - 20$ GHz regime [65], which corresponds with the transition observed here. The literature also presents no known source for this resonance [65, 86].

Neglecting these inconsistencies, the root-mean-square (RMS) deviation between each Gd^{3+}:Al_20_3 attributable B_m and B_f across the entire angular ESR spectra is calculated, and an average RMS of 3% error in positions is found. Notably, a best fit model is obtained using parameters modified by $< 3\%$ from measurements obtained in grown Gd^{3+} in Al_2O_3 crystals [62]. This suggests good integration of the dopant ions into only the relevant lattice sites and that the expected system symmetries are maintained despite the high energy, near surface implantation.

Considering microwave modes

It is also of note that, as expected from considerations arrived at in modelling Section 5.1, both perpendicular and parallel mode components of the microresonator device are observed.
To further confirm this, the relative areas within which the oscillating magnetic field orientated perpendicular or parallel to B_0 are considered and compared to the relative intensities of the ESR spectra. The ratio of areas where the operation can be considered perpendicular: parallel yields $3400 : 832/2$ μm^2 which is $\approx 8.2 : 1$. This compares to relative intensities of the ESR spectra: $8.75 : 1$, and is accurate to within 10%, further strengthening the argument that the resulting spectra comprises both the perpendicular and parallel operational modes and is highly dependent on the device geometry.
This highlights the need for controllable local implantation techniques in order to create successful hybrid devices integrating spin ensembles and superconducting structures.

8.3.2 Collective coupling rates

It is also interesting to compare the extracted collective coupling rates from the fit, $\Gamma_{coll(f)}$ to those obtained with numerical approximation made in Section 5.2. The numerical modelling is re-run for the spin degeneracy field responses attributable to the implanted Gd^{3+}:Al_20_3 system, and the modelled $\Gamma_{coll(f)}$ results are presented alongside the measured $\Gamma_{coll(m)}$ obtained from the experiment.

$Peak_f$	B_f (mT)	$\Gamma_{coll(f)}$ (MHz)	$\Gamma_{coll(m)}$ (MHz)
1	44	4.5	2.3
3	66	1.8	2.7
4	85	1.7	3.1
5	104	2.1	3.4

Table 8.5 A comparison of the modelled approximation of $\Gamma_{coll(m)}$ and the extracted collective coupling parameters from experiment $\Gamma_{coll(f)}$ for the 3.34 GHz LE resonator at 250 mK.

The values are in agreement to the same order of magnitude, indicating a good level of control of the implanted spin system and reasonable approximations within numerical modelling. However, what is noticeable is an increasing trend $\Gamma_{coll(m)}$ with greater magnetic fields, whereas in $\Gamma_{coll(f)}$ the coupling rate decreases. With further consideration, it is appreciated that the numerical model does not account for thermally excited populations of higher energy level states. Instead, it assumes that all 4 resonances are ground state transitions, when in fact, there are higher order transitions involved, accounting for this discrepancy.

8.3.3 A discussion of linewidths

In these and previous measurements of implanted rare-earth-ion-superconductor systems, coupling strengths have been limited by excessive linewidths [86, 88]. The causes of such linewidth broadening can be manifold, as discussed in Section 4.2.2.

In the presented results, the experimental ESR's are in good agreement with our modelled system. The model is based on crystal field parameters of Gd^{3+} in Al_2O_3 grown at similar concentrations [62] (as oppose to implanted). This suggests that dispersion arising from local defects in the crystalline environment may not be the primary cause of our excessive linewidth broadening.

Notably, in other work, linewidth broadening is not observed within flip-chip devices coupled to superconducting microresonator devices where the relative distances between the two systems are large [89]. Neither is broadening prevalent when coupling to other types of cavities where superconducting structures are not present [90].

With this in mind, one possible explanation for this broadening could be due to local field distortions or crystal strain induced by the close proximity of the superconductor. It is interesting to note that here, there are no observations of any angular dependence in the extracted linewidths.

8.3.4 Q_i in external magnetic fields

It is noteworthy that whilst, for example, coplanar Nb resonators display a large degradation in Q_i when subject to a B field, in these measurements, there is only a 5% degradation when swept to 100 mT, attributable to the use of NbN thin-film, LE geometry and optimal field orientation.

8.3.5 ESR sensitivity

It is also interesting to recognise the relative sensitivity of the system to these relatively small ESR signals and spin ensemble size: of order $\approx 10^{11}$. This is a much smaller number of spins than would be detectable using standard bulk cavity ESR spectroscopy. Since these measurements were performed, Bienfait. et al. [91] have further demonstrated even higher levels of sensitivity, using a similar experimental set-up based on a bismuth in silicon system, and using a Josephson parametric microwave amplifier combined with high-quality factor superconducting microresonators cooled at millikelvin temperatures, to detect 1700 bismuth donor spins.

8.3.6 Conclusions

In the case of this work, the system is not operating within the strong coupling regime - limited by large γ potentially due to inhomogeneous broadening caused by excess spin-spin interactions as well as defects. Previous experiments in Al_2O_3 with 100 ppm doped Gd^{3+} have reported linewidths down to 22 MHz [61], comparable to that of other potential hybrid systems [31]. It is therefore speculated that a decrease in γ could be achieved with a lesser concentration (whilst maintaining N) and reduction in defects, or through use of a the different ion/substrate combination. The strong coupling regime could also be reached by further optimisation of the collective system by increasing the number of coupled spins. The single spin coupling rate g_c can also be maximised further by, for example, operating at higher centre frequencies.

8.4 The temperature dependence of a micro-ESR trace

It is potentially interesting to explore the temperature dependence of the micro-ESR traces, since the ESR responses should demonstrate a temperature dependent response as the energy level populations change, as discussed in Section 4.2.3.

The measurements are performed using the same absorption spectroscopy method discussed in Section 7.4 with heat applied to the sample stage. Traces are not acquired until the temperature is stable across the given set-points. The measurement is performed with a static applied B_0 at an angle of $\beta = 13°$, where there are numerous ESR features for study. The resulting data is shown in Fig. 8.10, where the changes in the population of given energy levels can be observed by eye, with ESR response amplitudes decreasing in ESR transitions at ≈ 48 and 85 mT, and increasing at 57 mT with respect to an increasing temperature. This implies that the first transitions correspond to ground state energy splitting, whilst the latter corresponds to a higher energy level where the population increases with a rise in temperature.

The individual traces are fit, as in Section 8.3 and the frequency, collective coupling and linewidth parameters are extracted. The parameter of particular interest is the extracted Γ_{coll} of the responses corresponding to the $48, 85$ and 57 mT transitions. These are shown in Fig. 8.11 and are plotted with respect to increasing temperature. Dotted lines are added to guide the eye. From Fig. 8.11 the collective coupling rate of the ≈ 48 and 85 mT transitions clearly decrease with respect to an increase in temperature, as the ground state population level decreases. Meanwhile, the ≈ 58 mT transition increases in amplitude as this higher energy level increases in population. Further measurements and analysis, not performed in the scope of this work would be required to determine the exact relation of these responses in relation to Eq. 4.15.

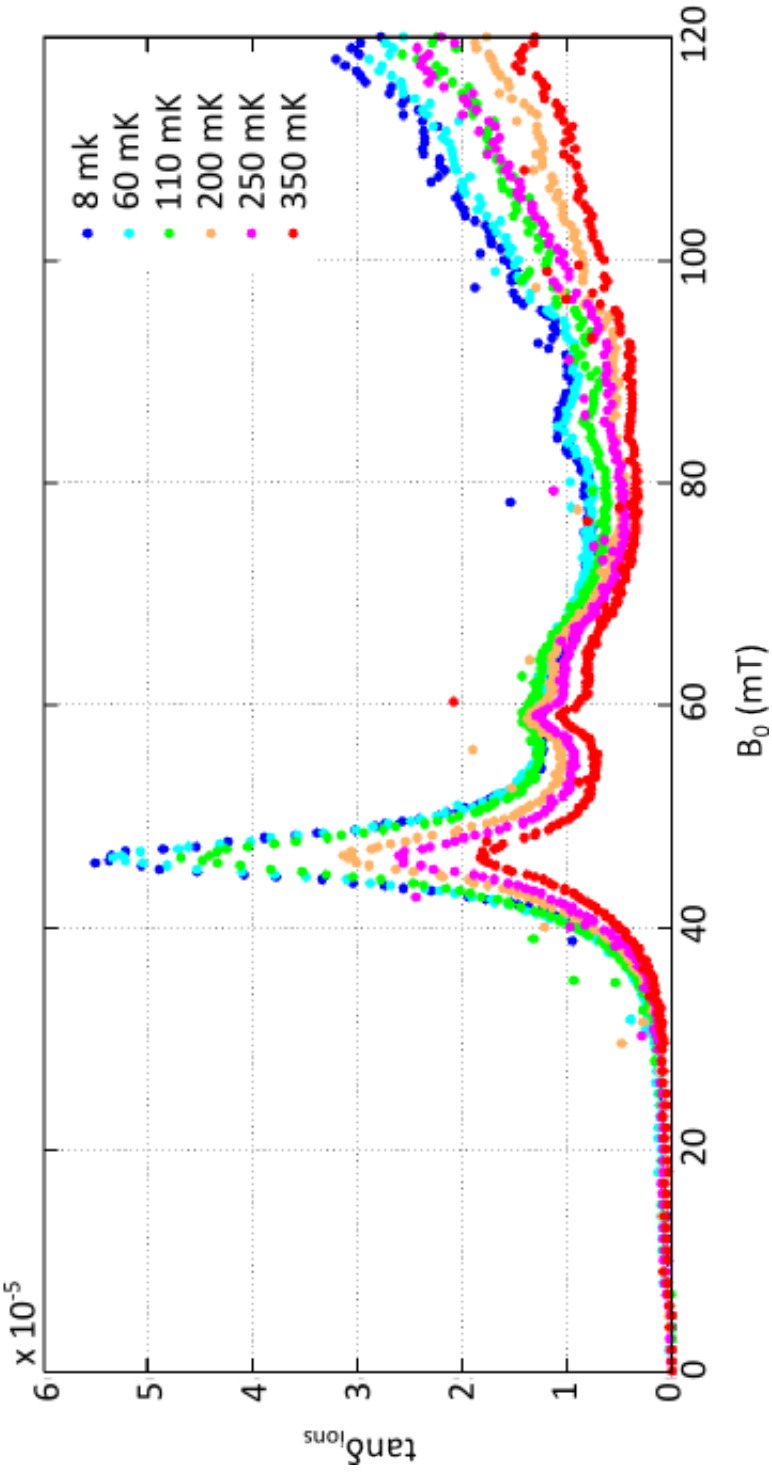

Fig. 8.10 A plot of the temperature dependence of an absorption spectroscopy trace, obtained by applying B_0 at an angle of 13°.

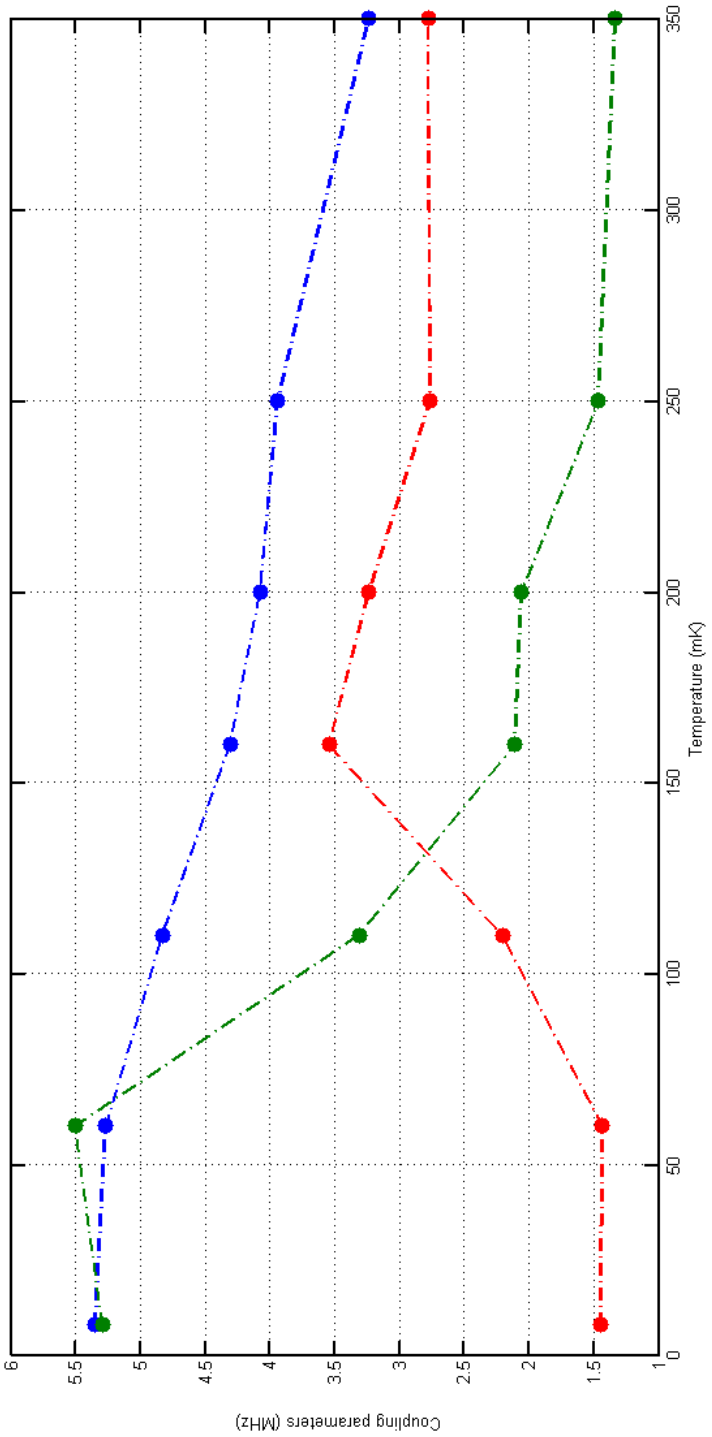

Fig. 8.11 A plot of the temperature dependence of the extracted coupling rates of ESR transitions in Fig. 8.10. Blue corresponds to the transition observed at ≈ 45 mT, red ≈ 58 mT and green ≈ 85 mT. The dotted lines guide the eye to the independent trends.

Chapter 9

A project summary and review

This Chapter provides a summary of the work within this thesis, highlighting areas of success, areas which were less successful, and areas which need further exploration. These will be given in relation to the initial project aims. Finally, a perspective of future directions of the field will be given.

9.1 Successes

We have been able to demonstrate the successful development of a hybrid device, fabricated using a technique for controlled ion implantation of rare earth ions in well-defined micron-sized areas, alongside lithographically defined micro-resonators. The technique allows for precise control of the spin ensemble in terms of the spin ensemble size, density and location without degradation of Q_i. The procedure is demonstrated as a scalable integration with lithographically defined circuitry and frequency multiplexing technology. We observe electron-spin-resonances in good agreement with numerical modelling, corresponding to a collective coupling of the order of 1 MHz and linewidths of $\approx$ 50 - 65 MHz.

From these measurements, it can be concluded that a maximal implantation dose of 10^{14} is required for successful fabrication of devices. This in agreement with the hypothesis of Ref. [62], who believed that at 'low concentrations' of 100 ppm, there would be no detrimental effect to the lattice (as discussed in Chapter 3.4). Within this limit, it can be concluded that the

ion-implantation and micro-processing required for the local ion implantation does not affect the intrinsic quality factors of the devices, which are comparable with Q_i's obtained with non-implanted microresonator devices previously studied in this group [64].

We were then able to demonstrate the characterisation of a locally implanted Gd^{3+} in Al_2O_3 system utilising angular dependent microwave ESR spectroscopy at millikelvin temperatures. We find that, despite the high energy and near surface implantation, the resulting angular-ESR spectra is in excellent agreement with the modelled Hamiltonian parametrised by symmetries obtained from a grown Gd^{3+} in Al_2O_3 system. These results support the notion that there is the successful integration of the dopant ions into their expected lattice sites. We were additionally able to observe clear contributions from individual microwave field components of our microresonator, further emphasising the need for controllable local implantation when coupling spins to superconducting quantum architectures.

We further demonstrate that angular-micro-ESR spectroscopy can provide an excellent means of studying even small numbers of spins, giving valuable feedback towards developing appropriate materials for future rare-earth based quantum information technologies.

9.2 Failures

9.2.1 The coupling regime and excess spin linewidths

Measurements of the fabricated hybrid devices show that the strong coupling regime was not achieved. We have been primarily limited by large spin linewidths γ within the ensemble, which are an order of magnitude larger than required.

This may be due to inhomogeneous broadening caused by excess spin-spin interactions as well as defects. Since previous experiments in Al_2O_3 with 100 ppm doped Gd^{3+} have reported line-widths down to 22 MHz [61], comparable to that of other potential hybrid systems [31], it appears that this linewidth increase is either attributable to the ion implantation process, or the proximity of the spin ensemble to the superconducting resonator device. With this in mind,

one possible explanation for this broadening could be due to local field distortions or crystal strain induced by the close proximity of the superconductor. It is interesting to note that here, there are no observations of any angular dependence in the extracted line-widths.
This is an area in which further exploration is required, however, from the measurements performed within this work, no final conclusions may be settled upon. What is implied from the angular dependent ESR measurements is that the implanted ions appear to be in their appropriate lattice sites, therefore adding weight to the crystal strain theory.

9.2.2 Pulsed ESR

Time was spent within the course of the project in setting up and attempting to perform pulsed-ESR measurements on the system. This was not successful, with no response observed within these measurements. It seems likely that the excess spin ensemble linewidth, and thus lower coupling rate, may be the cause behind this. Whilst this was disappointing, the system and experimental programmes required are set-up within the laboratory for such experiments in the future if the situation were to allow.

9.2.3 Alignment

During the first fabrication run, the alignment between the locally implanted spin ensemble and the micro-resonator device was not optimal. This was due to a mistake when converting the design files into the format required for the e-beam machine. This was resolved during the second fabrication run, where highly accurate alignment was achieved.

9.3 Final conclusions and outlook

In conclusion, we demonstrate the coupling of rare-earth Gd^{3+} ions locally implanted in an Al_2O_3 substrate to a superconducting NbN lumped element micro-resonator. The hybrid device is fabricated using a technique for controlled ion implantation of rare earths in well-defined

micron-sized areas, alongside lithographically defined micro-resonators. Using microwave absorption spectroscopy at millikelvin temperatures, we show the collective enhancement of a spin ensemble created via this ion-implantation process as a proof-of-principle of a promising hybrid device. The technique allows for precise control of the spin ensemble in terms size and location without degradation of Q_i, as well as scalable integration with lithography defined circuitry and frequency multiplexing technology.

We were further able to characterise the locally implanted system utilising angular dependent microwave ESR spectroscopy. We find that, despite the high energy and near surface implantation, the resulting angular-ESR spectra is in excellent agreement with the modelled Hamiltonian parametrized by symmetries obtained from a grown Gd^3+ in Al_2O_3 system. These results support the successful integration of the dopant ions into their relevant lattice sites. We also observe clear contributions from individual microwave field components of our microresonator, emphasising the need for controllable local implantation when coupling spins to superconducting quantum architectures. We further demonstrate that angular-micro-ESR spectroscopy can provide an excellent means of studying even small numbers of spins, giving valuable feedback towards developing appropriate materials for future rare-earth based quantum information technologies.

Whilst the measured collective coupling strengths exceed the decay rate of the cavity, the strong coupling regime is not yet reached due to large spin linewidths. Provided a reduction in linewidth, we believe the presented work shows the promising potential of locally implanted rare-earth doped crystals for application in hybrid quantum technologies.

9.3.1 Outlook

Whilst there are many avenues available to continue taking the subject area of spin doped substrates for the purpose of quantum memory forward, it is interesting to consider how this project could be extended in the future, from the position at which this project has been left. The most obvious constraint to the project lies in the excessive spin ensemble linewidth. This would require further exploration to determine the underlying cause behind this. Whilst, based

on these measurements, unlikely, the excess spin ensemble linewidths could be ion and substrate dependent. This started to be explored in collaboration with M. Hughes (Surrey/Salford University), who provided implanted erbium in silicon samples for study (paper in progress). These results also appeared to yield excessive linewidths during low-temperature micro-ESR experiments, despite appearing to have excellent room temperature standard ESR responses with sharp ESR transitions. This is clearly an area worth further exploration to determine if these effects are attributable to crystalline strain, superconductor proximity, specific ion and substrate combinations, or are simply attributable to crystalline defects formed by the ion implantation process.

Another interesting area for study available to us includes the integration of a qubit device, which may couple either directly to the chip transmission line or to the lumped element resonator, with a locally implanted spin ensemble beneath. This approach was initiated within the course of the project, with simulations validating the potential in terms of appropriate coupling rates. During the second fabrication run, designs were adapted to includes spaces on a number of samples to account for the future integration of qubit devices in collaboration with O. Astafiev (Royal Holloway University). The first steps in undertaking this project lie in the proof of operation of the qubit within the magnitude of magnetic fields required to tune the spin ensemble in and out of resonance. These first steps were initiated within the final year of this project and could easily be continued.

Bibliography

[1] J. I. Cirac, P. Zoller, H. J. Kimble, and H. Mabuchi, Phys. Rev. Lett. **78**, 3221 (1997).

[2] H. J. Kimble, Nature **453**, 1023 (2008).

[3] J. I. Cirac, P. Zoller, H. J. Kimble, and H. Mabuchi, Nat. Photonics **1**, 165 (2007).

[4] C. Simon, M. Afzelius, J. Appel, A. Boyer de la Giroday, S. J. Dewhurst, N. Gisin, C. Y. Hu, F. Jelezko, S. Kröll, J. H. Müller, et al., Euro. Phys. J. D **58**, 1 (2010).

[5] A. Wallraff, D. I. Schuster, A. Blais, L. Frunzio, R. S. Huang, J. Majer, S. Kumar, S. M. Girvin, and R. J. Schoelkopf, Nature **431**, 162 (2004).

[6] M. Hofheinz, H. Wang, M. Ansmann, R. C. Bialczak, E. Lucero, M. Neeley, A. D. O'Connell, D. Sank, J. Wenner, J. M. Martinis, et al., Nature **459**, 546 (2009).

[7] E. Lucero, R. Barends, Y. Chen, J. Kelly, M. Mariantoni, A. Megrant, P. O/'Malley, D. Sank, A. Vainsencher, J. Wenner, et al., Nat. Phys. **8**, 719 (2012).

[8] J. M. Martinis, K. Cooper, R. McDermott, M. Steffen, M. Ansmann, K. Osborn, K. Cicak, S. Oh, D. P. Pappas, R. Simmonds, et al., Phys. Rev. Lett. **95**, 210503 (2005).

[9] Z.-L. Xiang, S. Ashhab, J. Q. You, and F. Nori, Rev. Mod. Phys. **85**, 623 (2013).

[10] J. Clarke and F. K. Wilhelm, Nature **453**, 697 (2008).

[11] A. Andre, D. DeMille, J. M. Doyle, M. D. Lukin, S. E. Maxwell, P. Rabl, R. J. Schoelkopf, and P. Zoller, Nat. Phys. **2**, 636 (2006).

[12] P. Rabl, D. DeMille, J. Doyle, M. Lukin, R. Schoelkopf, and P. Zoller, Phys. Rev. Lett. **97**, 033003 (2006).

[13] B. Blinov, D. Moehring, L.-M. Duan, and C. Monroe, Nature **428**, 153 (2004).

[14] W. Rosenfeld, S. Berner, J. Volz, M. Weber, and H. Weinfurter, Phys. Rev. Lett. **98**, 050504 (2007).

[15] J. Verdú, H. Zoubi, C. Koller, J. Majer, H. Ritsch, and J. Schmiedmayer, Phys. Rev. Lett. **103**, 043603 (2009).

[16] M. Neeley, M. Ansmann, R. C. Bialczak, M. Hheinz, N. Katz, E. Lucero, A. O'Connell, H. Wang, a. N. Cleland, and J. M. Martinis, Nat. Phys. **4**, 523 (2008).

[17] A. Imamoglu, Phys. Rev. Lett. **102**, 083602 (2009).

[18] J. Wesenberg, A. Ardavan, G. A. D. Briggs, J. J. L. Morton, R. Schoelkopf, D. Schuster, and K. Mølmer, Phys. Rev. Lett. **103**, 070502 (2009).

[19] R. Amsüss, C. Koller, T. Nöbauer, S. Putz, S. Rotter, K. Sandner, S. Schneider, M. Schramböck, G. Steinhauser, H. Ritsch, et al., Phys. Rev. Lett. **107**, 060502 (2011).

[20] Y. Kubo, I. Diniz, C. Grezes, T. Umeda, J. Isoya, H. Sumiya, T. Yamamoto, H. Abe, S. Onoda, T. Ohshima, et al., Phys. Rev. B **86**, 064514 (2012).

[21] K. Sandner, H. Ritsch, R. Amsüss, C. Koller, T. Nöbauer, S. Putz, J. Schmiedmayer, and J. Majer, Phys. Rev. A **85**, 053806 (2012).

[22] C. Grezes, B. Julsgaard, Y. Kubo, M. Stern, T. Umeda, J. Isoya, H. Sumiya, H. Abe, S. Onoda, T. Ohshima, et al., Phys. Rev. X **4**, 021049 (2014).

[23] Y. Kubo, F. R. Ong, P. Bertet, D. Vion, V. Jacques, D. Zheng, A. Dréau, J.-F. Roch, A. Auffèves, F. Jelezko, et al., Phys. Rev. Lett. **105**, 140502 (2010).

[24] Y. Kubo, C. Grezes, A. Dewes, T. Umeda, J. Isoya, H. Sumiya, N. Morishita, H. Abe, S. Onoda, T. Ohshima, et al., Phys. Rev. Lett. **107**, 220501 (2011).

[25] D. I. Schuster, A. P. Sears, E. Ginossar, L. DiCarlo, L. Frunzio, J. J. L. Morton, H. Wu, G. A. D. Briggs, B. B. Buckley, D. D. Awschalom, et al., Phys. Rev. Lett. **105**, 140501 (2010).

[26] A. M. Tyryshkin, S. Tojo, J. J. L. Morton, H. Riemann, N. V. Abrosimov, P. Becker, H.-J. Pohl, T. Schenkel, M. L. W. Thewalt, K. M. Itoh, et al., Nat. Materials **11**, 143 (2012).

[27] R. E. George, W. Witzel, H. Riemann, N. V. Abrosimov, N. Nötzel, M. L. W. Thewalt, and J. J. L. Morton, Phys. Rev. Lett. **105**, 067601 (2010).

[28] C. O'Brien, N. Lauk, S. Blum, G. Morigi, and M. Fleischhauer, Phys. Rev. Lett. **113**, 063603 (2014).

[29] T. Böttger, Y. Sun, C. W. Thiel, and R. L. Cone, Phys. Rev. B **74**, 075107 (2006).

[30] S. Probst, H. Rotzinger, S. Wünsch, P. Jung, M. Jerger, M. Siegel, A. V. Ustinov, and P. A. Bushev, Phys. Rev. Lett. **110**, 157001 (2013).

[31] A. Tkalcec, S. Probst, D. Rieger, H. Rotzinger, S. Wünsch, N. Kukharchyk, A. Wieck, M. Siegel, A. Ustinov, and P. Bushev, Phys. Rev. B **90**, 075112 (2014).

[32] S. Probst, A. Tkalčec, H. Rotzinger, D. Rieger, J.-M. Le Floch, M. Goryachev, M. E. Tobar, A. V. Ustinov, and P. A. Bushev, Phys. Rev. B **90**, 100404 (2014).

[33] I. Usmani, M. Afzelius, H. de Riedmatten, and N. Gisin, Nat. Comms. **1**, 12 (2010).

[34] X. Zhang, C.-L. Zou, L. Jiang, and H. X. Tang, Phys. Rev. Lett. **113**, 156401 (2014).

[35] Y. Tabuchi, S. Ishino, T. Ishikawa, R. Yamazaki, K. Usami, and Y. Nakamura, Phys. Rev. Lett. **113**, 083603 (2014).

[36] C. Grezes, B. Julsgaard, Y. Kubo, M. Stern, T. Umeda, J. Isoya, H. Sumiya, H. Abe, S. Onoda, T. Ohshima, et al., Phys. Rev. X **4**, 021049 (2014).

[37] M. Goryachev, W. G. Farr, N. D. Carmo Carvalho, D. L. Creedon, J.-M. Le Floch, S. Probst, P. Bushev, and M. E. Tobar, App. Phys. Lett. **106** (2015).

[38] I. Chiorescu, N. Groll, S. Bertaina, T. Mori, and S. Miyashita, Phys. Rev. B **82**, 024413 (2010).

[39] E. Abe, H. Wu, A. Ardavan, and J. J. L. Morton, App. Phys. Lett. **98** (2011).

[40] J. Burnett, T. Lindström, M. Oxborrow, Y. Harada, Y. Sekine, P. Meeson, and A. Y. Tzalenchuk, Phys. Rev. B **87**, 140501 (2013).

[41] H. K. Onnes, Commun. Phys. Lab. Univ. Leiden **12**, 120+ (1911).

[42] M. Tinkham, *Introduction to Superconductivity: Volume 1* (Dover Publications Inc, 2004).

[43] D. C. Mattis and J. Bardeen, Phys. Rev. **111**, 412 (1958).

[44] S. Doyle, Ph.D. thesis, Cardiff University (2008).

[45] S. D. Graaf, Ph.D. thesis, Department Microtechnology and Nanoscience Chalmers University Technology, Sweden (2014).

[46] D. M. Pozar, *Microwave Engineering* (Wiley and Sons, 2012).

[47] M. Calvo, Ph.D. thesis, Sapienza University Rome (2008).

[48] B. A. Mazin, Ph.D. thesis, California Insitute Technology (2004).

[49] M. Meschke, W. Guichard, and J. P. Pekola, Nature **444**, 187 (2006).

[50] J. Burnett, L. Faoro, I. Wisby, V. L. Gurtovoi, A. V. Chernykh, G. M. Mikhailov, V. A. Tulin, R. Shaikhaidarov, V. Antonov, P. J. Meeson, et al., Nat. Comms. **5**, 4119 (2014).

[51] J. Burnett, Ph.D. thesis, Royal Holloway, University of London (2013).

[52] J. Wenner, R. Barends, R. C. Bialczak, Y. Chen, J. Kelly, E. Lucero, M. Mariantoni, A. Megrant, P. J. J. O'Malley, D. Sank, et al., App. Phys. Lett. **99** (2011).

[53] C. Neill, A. Megrant, R. Barends, Y. Chen, B. Chiaro, J. Kelly, J. Y. Mutus, P. J. J. O'Malley, D. Sank, J. Wenner, et al., App. Phys. Lett. **103** (2013).

[54] P. Masha, S. H. W. van der Ploeg, G. Oelsner, E. Ilichev, S. Wunsch, H.-G. Meyer, and M. Siegel, App. Phys. Lett. **96** (2010).

[55] T. K. K. Yoshida, K. Watanabe and K. Enpuku, IEEE Trans. App. Super. **5** (1995).

[56] E. H. Brandt and M. Indenbom, Phys. Rev. B **48**, 12893 (1993).

[57] A. A. Abrikosov, Rev. Mod. Phys. **76**, 975 (2004).

[58] J. E. Healey, T. Lindstrom, M. S. Colclough, C. M. Muirhead, and A. Y. Tzalenchuk, App. Phys. Lett. **93**, 043513 (2008).

[59] D. Bothner, C. Clauss, E. Koroknay, M. Kemmler, T. Gaber, M. Jetter, M. Scheffler, P. Michler, M. Dressel, D. Koelle, et al., App. Phys. Lett. **100** (2012).

[60] K. Saeedi, S. Simmons, J. Z. Salvail, P. Dluhy, H. Riemann, N. V. Abrosimov, P. Becker, H.-J. Pohl, J. J. L. Morton, and M. L. W. Thewalt, Science **342**, 830 (2013).

[61] A.-N. Mushait, Ph.D. thesis, Durham University, Durham (1988).

[62] S. Geschwind and J. P. Remeika, Phys. Rev. **122**, 757 (1961).

[63] C. Kittel, *Introduction to Solid State Phys.* (John Wiley and sons, 1991).

[64] T. Lindstrom, J. E. Healey, M. S. Colclough, C. M. Muirhead, and A. Y. Tzalenchuk, Phys. Rev. B **80**, 132501 (2009).

[65] W. G. Farr, D. L. Creedon, M. Goryachev, K. Benmessai, and M. E. Tobar, Phys. Rev. B. **88**, 224426 (2013).

[66] P. H. E. Meijer and J. Lewiner, J. Res. Nat. Bureau Stand. **75A**, 493 (1971).

[67] A. Abragam and B. Bleaney, *Electron Paramagnetic Resonance Transition Ions* (Oxford University Press, 1970).

[68] B. B. A. Abragam, *Electron Paramagnetic Resonance Transition Ions* (Dover Publications Inc, 1986).

[69] S. Haroche and J.-M. Raimond, *Exploring the Quantum* (Oxford University Press, 2013).

[70] M. Tavis and F. W. Cummings, Phys. Rev. **170**, 379 (1968).

[71] T. Holstein and H. Primaakoff, Phys. Rev. **58**, 1098 (1940).

[72] D. Braun, J. Hoffman, and E. Tiesinga, Phys. Rev. A **83**, 062305 (2011).

[73] A. Lund, M. Shiotani, and S. Shimada, *Principles of ESR* (Springer Netherlands, Dordrecht, 2011).

[74] Z. Kurucz, J. H. Wesenberg, and K. Mølmer, Phys. Rev. A **83**, 053852 (2011).

[75] P. Bushev, A. K. Feanov, H. Rotzinger, I. Protopopov, J. H. Cole, C. M. Wilson, G. Fischer, A. Lukashenko, and A. V. Ustinov, Phys. Rev. B **84**, 060501 (2011).

[76] S. Probst, Ph.D. thesis, Karlsruher Instituts fur Technologie (KIT) (2015).

[77] S. Stoll and A. Schweiger, Biol. Magn. Reson **27**, 299 (2007).

[78] S. Stoll, Methods in Enzymology **563**, 121 (2015).

[79] S. Stefan, Ph.D. thesis, Eidgenossische Technische Hochschule, Zurich (2003).

[80] A. A. B. Brojeny, Y. Mawatari, M. Benkraouda, and J. R. Clem, Superconductor Science and Technology **15**, 1454 (2002).

[81] S. E. D. Graaf, A. V. Danilov, A. Adamyan, T. Bauch, and S. E. Kubatkin, J. App. Phys. **112**, 123905 (2012).

[82] S. Franssila, *Introduction to Microfabrication* (John Wiley and sons, Ltd, 2010), 2nd ed.

[83] Y. Dong, Ph.D. thesis, University of California, Santa Barbara (2004).

[84] C. White, J. McCallum, and L. Boatner, J. App. Phys. **54**, 683 (1983).

[85] G. N. van den Hoven, E. Snoeks, A. Polman, J. W. M. van Uffelen, Y. S. Oei, and M. K. Smit, App. Phys. Lett. **62**, 3065 (1993).

[86] I. Wisby, S. E. de Graaf, R. Gwilliam, A. Adamyan, S. E. Kubatkin, P. J. Meeson, A. Y. Tzalenchuk, and T. Lindström, App. Phys. Lett. **105**, 102601 (2014).

[87] I. S. Wisby, S. E. de Graaf, R. Gwilliam, A. Adamyan, S. E. Kubatkin, P. J. Meeson, A. Y. Tzalenchuk, and T. Lindström, Phys. Rev. App. **6**, 024021 (2016).

[88] S. Probst, N. Kukharchyk, H. Rotzinger, A. Tkalčec, A. D. Wieck, M. Siegel, A. V. Ustinov, P. A. Bushev, A. Tkalčec, and S. Wünsch, App. Phys. Lett. **105**, 162404 (2014).

[89] A. Tkalčec, S. Probst, D. Rieger, H. Rotzinger, S. Wünsch, N. Kukharchyk, A. D. Wieck, M. Siegel, A. V. Ustinov, and P. Bushev, Phys. Rev. B **90**, 075112 (2014).

[90] S. Probst, A. Tkalčec, H. Rotzinger, D. Rieger, J.-M. Le Floch, M. Goryachev, M. E. Tobar, A. V. Ustinov, and P. A. Bushev, Phys. Rev. B **90**, 100404 (2014).

[91] A. Bienfait, J. J. Pla, Y. Kubo, M. Stern, X. Zhou, C. C. Lo, C. D. Weis, T. Schenkel, M. L. W. Thewalt, D. Vion, et al., Nat. Nano. **11**, 253 (2016).

Appendix A

Fabrication Details

- Nickel alignment markers
  - Tri-layer resist
    - mmA8.5mAAEL10: 570 nm
    - Sx Ar-P: 70 nm
    - espacer (monolayer)
  - E-beam exposure
  - Develop:
    - E-spacer removal: water rinse
    - O-Xylene: 1 minute
    - H_2O and IPA rinse
  - Oxygen plasma ashing
  - Ni Evaporation: 80 nm
  - Acetone lift Off
  - Oxygen plasma ashing
- Silicon nitride mask

- SiN deposition: 600 nm

  MFSIN(PCVD) @ 1 and 13.56 MHz

- Al evaporation: 70 nm
- PMMA(A4) resist, 3000 rpm, 5 min bake @ 170° C
- E-beam exposure in DUV for 250s
- Develop: H_2O and IPA mixture $(7:93)$ for 3 min
- Reactive ion etch:
  - Al etched in chloride plasma: 2 min 40 s
  - SiN etched in CF_4 plasma: $Cl2\ Al2\ SiC4$
- $MF319$ wet etch (7 min)

- Mask Removal
  - 10 min HF bath
  - 5°C/min ramp
  - Hold @ 980°C for 1 hr
  - 4 hr cool to RT

- NbN sputtering
  - 200 nm deposited
    - 6.5 sccm N2
    - 60 sccm Ar
    - 12 μbar
    - 430 s

- Resist spinning
  - UV5-0.8 (+ve photoresist)

        * 3000 rpm
        * Accel. 1000 ms-1
        * Bake @ 130°C for 2 min

- E-beam writing
    - Align: Calibrate position
        * Rotation and centre
    - Calibrate: aperture, current, focus and astigmatism
    - Expose at 35 nA, 23 μC/cm^2

- Developing
    - Bake at 130°C for 90 s
    - MF-24-A for 40 s
    - Water rinse

- Etch
    - NbN in plasma (404) in NF_3 gas
    - Over etch for 10 s, total etch time: 90 s for 200 nm of NbN
    - Resist clean (1165 for 12 hours)
    - Water rinse
    - Ash if residue.

Appendix B

Validating the EasySpin model

Before performing simulations relevant to the experimental set-up of this work, it is sensible to check the correct operation of this simulation by simulating spectral results which have previously been obtained. We therefore turn to the experimental results shown in Fig. B.1(a)(Ref. [62]). These results were obtained using a grown Gd^{3+}:Al_2O_3 crystal with a doping concentration comparable to that of our work. The measurements were performed at room temperature and at 4.2 K. The r-plane $(10\bar{1}0)$ was mounted parallel to the B_z axis of standard cavity and the magnetic field rotated in the r-plane.

This experimental result may be replicated using the EasySpin simulation technique described in Chapter. 5 by coding the experimental parameters relevant to this experiment (shown in Listing. B.1). the Gd^{3+} isotope is not specified in Ref. [62], so the Gd isotope of most natural abundance (Gd^{157}) is assumed.

The resulting simulations are shown in Fig. B.1(b) and successfully replicates the spectra obtained experimentally. This is verified by an overlay of the two in Fig. B.1(c). Additional transitions are observed in the modelling since the results in Ref. [62] present only the $-\frac{1}{2} \rightarrow +\frac{1}{2}$ and $+\frac{1}{2} \rightarrow +\frac{3}{2}$ transitions.

These results help to provide some confidence in the veracity of the simulation under the experimental conditions of our own work.

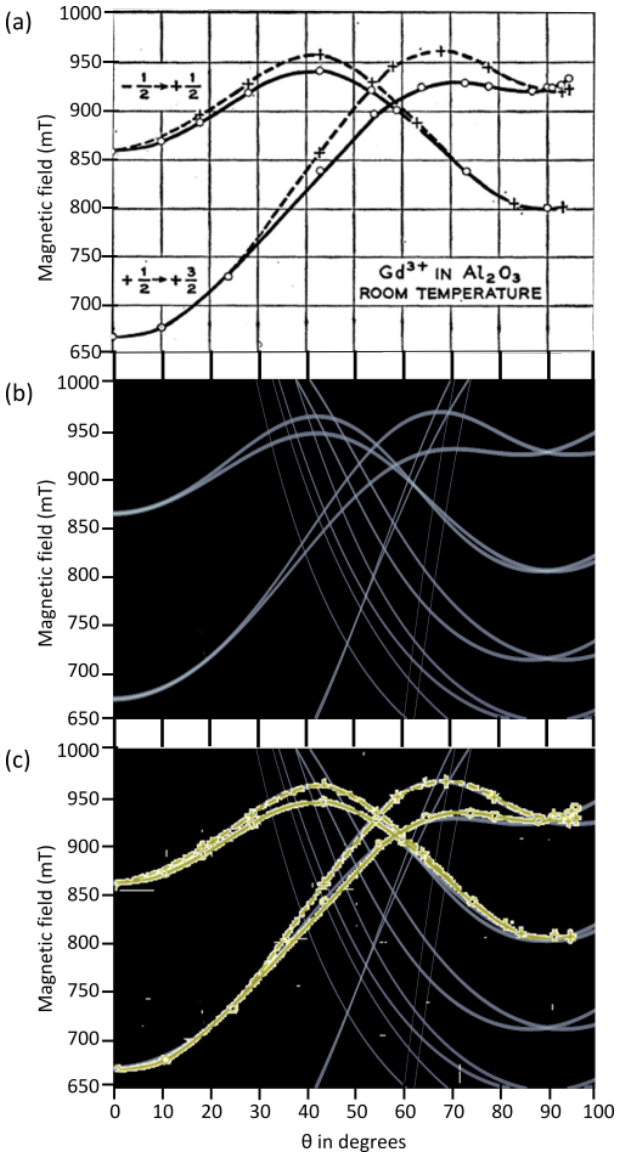

Fig. B.1 (a) Figure from Ref. [62]: Cavity ESR (24 MHz) of the Gd^{3+} in Al_2O_3 system $-1/2 \rightarrow +1/2$ and $+1/2 \rightarrow -1/2$ lines observed as the magnetic field is rotated in the $(10\bar{1}0)$ plane at room temperature. (b) Simulated spectra using EasySpin for the experimental parameters in Ref. [62]. (c) Overlay of the above two figures with colour enhancement of (a) for clarity. The simulation and experiment are in good agreement, verifying the validity of the simulation. Additional ESR lines of higher order transitions are also observed in the simulation which are not reported in the experiment.

```
field_start = 0;
field_stop = 1000;
angle_start = -100*(pi/180);
angle_stop = +100*(pi/180);
Fieldrange=[field_start field_stop]; %in mT
Exp=struct('mwFreq',MWFreq,'Range',Fieldrange);
Exp.Temperature=300;
alpha = 60;
beta = 0;
gamma = 0;
Exp.CrystalOrientations = [alpha beta gamma]*pi/180;
MWFreq=24; %in GHz
Sys=struct('S',7/2,'g',1.9912,'Nucs','157Gd');
```

Listing B.1 Experimental `'Exp.'` and system `'Sys.'` parameters used to simulate the experimental results of Ref. [62].

Appendix C

The collective coupling calculation

The following code details the simulation of the collective coupling parameters:

Listing C.1 Simulation of collective coupling parameters

```
1
2  %(*Constants*)
3  g=1.998; %gfactor
4  mub=9.274*10^(-24); %bohr mag
5  mu0=4*pi*10^(-7); %vacuum permeability
6  hbar=6.63e-34/(2*pi);
7  kb=1.38*10^(-23);
8
9  %(*Cavity Parameters*)
10 b=4*10^(-6); %strip spacing/2
11 a=4*10^(-6);%strip Width
12 W=a+b;
13 fo=3.352*10^(9); %cavity frequency Hz
14 w0=2*pi*fo;
15 Z=20; %(*for NbN 140nm fractal)
16 L=Z/w0;
17 M = 11; %Number of Meanders
18 %(* Spin ensemble parameters *)
19 Len = 100*10^(-6); %(* Length of the segment covered with spins *) ...
       in m
20 Sx0 = 0.0*10^(-6); %(* Center position, x *) in m
21 Sx = 200.0*10^(-6); %(* Width, something very wide for gd lines *) ...
       in m
22 Sy0 = 160*10^(-9); %(* Bottom position, peak implantation depth *) ...
       in m
23 SyFHWM = 33*10^(-9);% (* Height, FWHM of implantation profile *) in m
24 SyDepth = 300*10^(-9); %(Depth of interest over all implant ...
       profile) in m
25 SyDepth = 180*10^(-9);
26 SiteDensity = 1.4832e28; % site density per m^3
27 SiteDensity =1.4e28; % total number of sites per m^3
28 check: total coupling is independent of SiteDensity. Ok!
29 Implantation Parameters 1e14 in m
30 Dose=1e13*1e4; % spins/cm2->spins/m2
31 PeakConcentration=Dose/(sqrt(2*pi)*SyFHWM); %Peak Concentration, ...
       spins/m3
32 IntVal=2e-9;%cl (m)
33 FinalVal=SyDepth; %Depth of interest (m)
34 step=1e-9;
35 y=IntVal:step:FinalVal;
36 ConcentrationProfile = ...
       PeakConcentration.*(exp((-(y-Sy0).^(2))./(2*(SyFHWM.^(2)))));
37 figure(100)
38 semilogy(y,ConcentrationProfile)
```

Listing C.2 Simulation of collective coupling parameters, continued 2

```
figure(101)
ppmFun= (ConcentrationProfile./SiteDensity).*1e5; %Spin Density ...
    function in ppm
semilogy(y,ppmFun)
SpinDensityFun = (ppmFun.*2)./((5.3*10^(-10)).^3)/2; %(* Spin ...
    Density function in spins/m3 *)
ConcentrationProfile = ...
    @(y)PeakConcentration.*(exp((-(y-Sy0).^(2))./(2*(SyFHWM.^(2))))); ...
    % spins/m3
ppmFun= @(y)(ConcentrationProfile(y)./SiteDensity) ;%Spin Density, ...
    dimensionless
pN_Vspin = @(y)((ppmFun(y))*SiteDensity); %(* Spin Density function ...
    in spins/m3 *)
yvec = linspace(0,500e-9,100);
(*Magnetic field distribution*)
m=sqrt(1-(b^(2))/(W^(2)));
ell= ellipke(m);
I0 = (sqrt((hbar*w0)/(2*L)));
H0=abs(I0/(W*ell)); %Eqn 7.9
g0=((mub*mu0)/(2*pi*hbar))*H0; %Eqn 7.11
H = @(x,y) -H0.*((W.^2)./(sqrt((x+1i.*y).^(2)-b.^(2))...
...*sqrt(((x+1i.*y).^(2)-W.^(2))))); %Eqn 7.7
MagH = @(x,y) (H(x,y)); %Numerator 7.10 integral Bfield part
h1=0;
Bnorm = MagH(0,h1); %Denomentator 7.10 integral Bfield part
BFieldFun = @(x,y) abs((MagH(x,y)./Bnorm)).^2; %Total Bfield part ...
    of integral dimensionless
xvec = linspace(-50e-7,50e-7,100);
plot(xvec,log10(BFieldFun(xvec,-100e-9)))
Test1=integral(pN_Vspin,IntVal,SyDepth)
Test2=integral2(BFieldFun,-Sx/2+Sx0,Sx/2+Sx0,IntVal,SyDepth);

%(*Find Geff function: Previously when integrated sep. = 0.1159.)
GeffFunction = @(x,y) pN_Vspin(y).*BFieldFun(x,y) ; % Unit: spins/m3
OverallInt=quad2d(GeffFunction,-Sx/2+Sx0,Sx/2+Sx0,..
...IntVal,SyDepth,'MaxFunEvals',1e5,'RelTol',1e-2);
Geffective=abs((OverallInt)*Len);
Geff=sqrt(Geffective); %
```

Listing C.3 Simulation of collective coupling parameters, continued 3

```
%(*Find collective coupling g0*rootN*Geff*ThermalFactor #Hz*)
%(Find Number of spins)
SpinArea = Len*Sx; %(m)
NSpinsDepth = quad(pN_Vspin,IntVal,FinalVal); %Integrate over ...
    function between area of interest
NSpinsEnsemble=NSpinsDepth.*(Len.*Sx);
%Multiply Z(depth component number of spins by area to get volume - ...
    x len * width

%(*Boltzman Thermal and B field Distribution:)
T=0.02; %Kelvin
H=0.041; %Use this value as a test for now - Can explore more ...
    anothe time.
H=0.078
NThPolarised=(NSpinsEnsemble*(sqrt(tanh((g*mub*H)/(2*kb*T)))));
ThermalFactor=NThPolarised/NSpinsEnsemble; %number available in ...
    ground state
ContributingSpins=ThermalFactor*NSpinsEnsemble*(M-1);
LEFactor = sqrt(M-1);

Find Total coupling
TotalCouplingT=(g0*sqrt(NSpinsEnsemble)*Geff*ThermalFactor)/10^(6);
TotalCouplingT=(LEFactor*g0*Geff*ThermalFactor)/10^(6) % g0 is in ...
    units of Hz. Other variables are dimensionless.
go=109, sqrt(Nspins) thermal fact approx 0.6
MaxCoupledT=(10^6*TotalCouplingT/g0)^2;
Measured LW %FWHM in mT
gausslw=mt2mhz(4.5); %
lorenzlw=55;
RequiredLw=mhz2mt(TotalCouplingT)
AvCoupPerSpin = (TotalCouplingT * ...
    10^6)/(ContributingSpins*ThermalFactor)
```

Appendix D

Other experimental techniques

The following summarises other experimental techniques performed independently or with collaborators throughout the course of the project, with the motivation for performing these tasks, and the outcome achieved.

D.1 Performed by myself

D.1.1 MPMS

The magnetic property measurement system (MPMS) was operated at NPL to perform a number of magnetic measurements on the implanted sapphire crystals. The motivation of these measurements was to investigate the magnetic moments, where previous experiments in other groups had hinted at the property of giant-magnetic moments when the concentration of implanted ions in sapphire was too high. We speculated that these measurements may also provide further information about impurities, or other unexpected magnetic moments which may be present within the substrate and device. Measurements were performed, but the MPMS was not sufficiently sensitive to the number of ions present in samples within this work.

D.1.2 Fridge fixing

During the course of the project, a custom re-condensing dewar and cryo-magnet was installed and was integrated with a pre-existing cryostat system. This was not a trivial procedure and a large proportion of time was spent trouble shooting and fixing these systems such that they would work in conjunction with each other.

D.1.3 Pulsed ESR

Time was also spent attempting to perform pulsed-ESR experiments on the spin ensembles. Much time was spent setting up the system and programmes to perform these pulsed measurements. Measurements performed included changing pulse lengths, pulse distances, tuning patterns and attempting more simple ring-down time measurements. Unfortunately, we were not able to gain a response from the spin ensemble in this manner. We were likely restricted by the excessive line-width associated with the spin ensemble, and the low coupling rate operation in the weak-coupling regime.

D.2 Performed in collaboration

D.2.1 THz spectroscopy

THz spectroscopy measurements were performed at NPL in collaboration with John Molloy. Investigations were performed on a number of crystals at different ion implantation concentrations. It was believed that a level of damage assessment may be obtained from the crystalline phonon-modes within the implanted substrates. This yielded some interesting results with full analysis yet to be performed. Whilst this was an interesting side project, there results were ultimately more interesting to the field of THz spectroscopy than relevant to this thesis.

D.2.2 SIMS

Collaborations were mediated by myself to perform secondary ion mass spectroscopy (SIMS) within NPL and Surrey university. Measurements of the implanted ion substrate. Again, this did not yield successful results due to the low concentration of the impurity ion.

D.2.3 Photo-luminescence

Collaborations were managed and photo-luminescence measurements of the implanted ion substrate were performed at NPL. Again, this did not yield successful results possibly due to the low concentration of the impurity ion.

D.2.4 Cavity electron-spin-resonance measurements

Collaborations with UCL enabled room temperature and cold standard cavity ESR experiments to be performed on the implanted substrate. Again, this did not yield successful results possibly due to the low concentration of the impurity ion.